ELASTICALLY DECOUPLING RELICS, MULTI-MESSENGER SEARCHES FOR DARK MATTER, AND ν PROBES OF NEW PHYSICS

A Dissertation

Presented to the Faculty of the Graduate School

of Cornell University

in Partial Fulfillment of the Requirements for the Degree of

Doctor of Philosophy

by

Yu-Dai Tsai

August 2018

ELASTICALLY DECOUPLING RELICS, MULTI-MESSENGER SEARCHES FOR DARK MATTER, AND ν PROBES OF NEW PHYSICS

Yu-Dai Tsai, Ph.D.

Cornell University 2018

We discuss a new dark matter framework, Elastically Decoupling Relics (ELDER), and its phenomenology. We then discuss multi-messenger astrophysical probes of various dark matter scenarios, utilizing electromagnetic emission and gravitational signatures from neutron star mergers (and black hole mergers with the gravitational wave signature) to probe super-heavy ($\mathrm{PeV} - \mathrm{EeV}$) asymmetric dark matter. Finally, we discuss how to use intensity frontier experiments to investigate weakly coupled states, including dark scalars, dark photons, heavy neutral leptons, and millicharged particles.

BIOGRAPHICAL SKETCH

When you look up my CV, you see a title "Ph.D. in Physics".

What you don't see, is a story that a kid that was physically abused in public in the middle school, by several of his teachers, for failing to hand in homework on time and failing the dress code. What you don't see, is a story that a teenager had to transfer between schools multiple times, due to a fatal earthquake, and due to the rapid advances of his parents' careers and the associated job changes. What you don't see, is that someone is fundamentally different from others, but was never given proper care or consultant when he was young, and all the obstacles that come with it.

I have come a long way, and I will keep going.

Getting a doctoral degree was difficult, but it is nothing compared to all these previous struggles I had to overcome in life.

The things I had to overcome in life, are also nothing compared to more severe problems some people have to face, every single day.

My school days have not always been easy, but in general, I have been given so much more opportunities, in comparison to those who haven't.

This thesis is dedicated to those who are not offered a fair chance, but never give up on what they believe to be important.

This thesis is dedicated to those who never give up.

ACKNOWLEDGEMENTS

I would like to thank Maxim Perelstein (my advisor), Csaba Csaki, and Jim Alexander for being on my Ph.D. committee, and educating me throughout my Ph.D. study. I also thank my family, my friends, and everyone that I have learned from during my years in Ithaca and Waterloo. I especially thank Maxim for reading through the Introduction of this thesis in detail and for helping me revise the thesis. I also thank Junxue Zhao for proofreading this thesis.

I would like to thank Asimina Arvanitaki, Yuval Grossman, Tom Hartman, Dan Hooper, Liam McAllister, Hitoshi Murayama, Maxim Pospelov, Tracy Slatyer, and Tung-Mow Yan for giving me advice and helping me getting established as a researcher.

I would also like to thank Joseph Bramante, Eric Kuflik, Tim Linden, Gabriel Magil, and Ryan Plestid for our wonderful collaborations.

I have had great times and memorable moments with my friends including Masha Baryakhtar, Asher Berlin, Jeff Dror, Junwu Huang, Gordan Krnjaic, Gowri Kurup, Hongwan Liu, Salvator Lombardo, Jing Qian, Nick Rodd, Oren Slone, Ofri Telem, Zhengkang Zhang and many other friends I met at TASI, TRISEP, GGI, and Pheno.

Among my family members, I would especially like to thank my parents, Ju-Bo Chang and Ping-Kun Tsai, and my sister, Chih-Chi Tsai.

CONTENTS

CHAPTER 1

INTRODUCTION

A new era of fundamental physics research has arrived. To begin with, we are entering the age of multi-messenger astrophysics. For the first time ever, gravitational-wave (GW) signatures from black hole (BH) mergers, as well as GW and other signatures from a neutron star (NS) merger, were observed. Furthermore, we have begun to study dark matter (DM) beyond the traditional cold dark matter (CDM) and the weakly interacting massive particles (WIMP) paradigms. New tools are currently being developed, including the use of novel condensed-matter materials as DM detectors or the application of atomic interferometry to probe new physics. The Large Hadron Collider (LHC) is running at peak energy, and many small-scale and high-luminosity experiments will soon begin operation. The research presented in this thesis utilizes these ideas, tools, and observations to investigate the deepest secrets of the Universe.

In particular, most of the research presented here is focused on DM and hidden particles. DM remains one of the basic constituents of our universe that we are not able to understand, yet there are overwhelming evidences of its existence. In this thesis, I propose new models of DM and hidden particles, and develop search methods using astrophysical and terrestrial probes.

In this Introduction, first I will briefly summarize my various projects on DM and hidden particles. I will then review the evidence for DM, introduce the WIMP paradigm, and give the framework to go beyond the WIMP paradigm that was proposed in my work on Elastically Decoupling Relics. I will end with an extended discussion of probing DM using astrophysical measurements and ground-based

experiments.

1.1 Summary of Ph.D. Research

Model: Elastically Decoupling Relics

My collaborators and I proposed a new DM candidate, which has its current-day abundance mostly determined via the elastic scattering/decoupling between Standard Model (SM) particles and DM, called Elastically Decoupling Relics (ELDER) [1, 2]. ELDER has a distinctive thermal history and new phenomenological implications in comparison to the usual CDM scenario. ELDER provides solid predictions for both next-generation DM direct-detection experiments and dark photon searches. The concept of elastic decoupling before freezing out of the thermal relics can be applied to many existing models as well as future model building.

Astrophysical Signatures of DM-induced Neutron Star Implosions

If DM is asymmetric, a neutron star (NS) could potentially collect enough DM in its center to form a black hole (BH). The BH could then implode the host NS. The radial distribution of NS mergers in a galaxy could thus be significantly modified by such DM-induced implosions. In [3], my collaborators and I studied the optical, radio, and GW (merger) signatures, directly or indirectly caused by the DM-induced NS implosions. We focused on heavy asymmetric DM (ADM) as an example, because the capture and collapse processes are better understood in this mass regime. The NS merger distribution observed via LIGO/Virgo GW detections and the associated merger kilonovae observed via optical telescopes can be applied to test such DM models given 5–10 localized detections. Bounds were set on the ADM model parameter space using the present Dark Energy Survey (DES)

Kilonova Search results and the Milky Way's r-process element abundance. It is worth noting that the recent detection of an NS merger event (GW170817+EM signatures) is the first ever robust data point for our statistical test. We are currently actively analyzing the data to determine whether we can improve the current constraint based on this single measurement alone, as well as preparing for future events to come.

Intensity-Frontier Experiments as Probes of Hidden Sector Particles

Weakly interacting particles, including dark scalars, dark photons, sterile neutrinos, and axion-like particles, could explain several experimental anomalies and are of great theoretical interest. For one, they could be mediators for Standard Model (SM) particles to interact with the dark sector that may include DM particles. In [4], Professor Maxim Pospelov and I proposed to recast the Borexino-SOX experiment to probe light scalars and sub-MeV dark photons. The light scalar is introduced to explain the anomaly in the charge-proton radius measurement. This hypothesis can be definitely tested with the BoreXino-SOX experiment.

In [5], my collaborators and I studied the sensitivities of probing heavy neutral leptons with neutrino dipole portals using the neutrino experiments (the short baseline neutrino (SBN) program) at Fermilab and the proposed Search for Hidden Particle (SHiP) experiment at CERN. Furthermore, we proposed that numerous neutrino experiments, including LSBD, the Fermilab SBN program (MicroBooNE and Short Baseline Near Detector (SBND)), Deep Underground Neutrino Experiment (DUNE) and SHiP can be applied to study the millicharged particles (mCPs) [6]. These experiments can already set leading constraints on low-mass ($\sim$ MeV - 100 MeV) mCP and could greatly advance the sensitivity reach for mCPs

up to 5 GeV.

Other than the aforementioned topics, I also studied the possible electroweak-scale explanations of matter-antimatter asymmetry, the origin of the neutrino masses, and the small-scale structure of the Universe. In particular, I studied electroweak phase transition (EWPT) and Higgs-hierarchy-motivated models. EWPT is important for the electroweak baryogenesis mechanism, which could explain the matter – anti-matter asymmetry in our present Universe. In [7], Professor Perelstein and I studied the addition of extra states that can successfully generate a first-order electroweak phase transition, and in turn, modify the Higgs properties that could be measured by the LHC and future colliders. I also worked on a number of other different subjects as a graduate student, including condensed matter, hadronic/nuclear, and theoretical black hole physics [8–10].

1.2 Evidence for Dark Matter

In this section, I will briefly summarize the observational evidence for DM, and discuss the properties of DM that can be inferred from these observations. Multiple observations, at a variety of length scales, provide overwhelming evidences for dark matter. I will go through some of them briefly in this section.

The first evidence we talk about is the galaxy rotation curves. The visible mass density of a spiral galaxy is mostly distributed near its center. As the stars of spiral galaxies rotate around the galactic center, their velocities are determined by the mass enclosed within their orbits. Based on the prediction, the velocities of galactic satellites should drop rapidly as the visible mass density decreases away from the center of the galaxy. However, observed satellite velocities do not follow

this pattern, and instead remain roughly constant as the distance from the galactic center grows. The non-visible matter (dark matter, DM) was thus postulated to explain the curves (see, e.g. [11]). Based on the virial theorem and measured velocity distribution, one can also determine the mass distribution in stellar systems such as elliptical galaxies [12]. It was found that the mass distributions in elliptical galaxies generally do not match the expectation from the visible mass distribution, and DM can be again applied to explain the discrepancies.

The next evidence we discuss is gravitational lensing. There are two kinds of gravitational lensing effects researchers consider, strong lensing [13] and weak lensing [14]. Both rely upon the general relativity prediction that light can be bent by a heavy object, and one can use the distortion or multiplicity of images to determine the mass of the gravitational source responsible for the "lensing" (light bending) effect.

Strong lensing, as its name suggests, is based on the actual distortion of galaxy images into arc shapes observed. The distortion geometry can directly infer the mass of the object, usually a galaxy clusters that the light is passing though [13]. Furthermore, the strong lensing can create multiple images from the same light source. Strong lensing can be used to infer the mass distribution of the gravitating matter and has been used to determine the distribution of DM. Weak gravitational lensing, on the other hand, describes the situation in which the images of galaxies are only slightly distorted. In this case, it is not possible to get useful information out of a single image, but mean mass distribution can be extracted from a statistical analysis of combined surveys [14].

The cosmic microwave background (CMB) also provides strong but indirect evidence of dark matter. CMB, as its name suggests, is a background radiation in

the microwave wavelength coming from the early universe. Such radiation comes from the era of recombination/photon decoupling, roughly 378,000 years after the postulated beginning of the Universe. After this time, photons were able to travel through space without interacting with matter. The CMB spectrum thus contains information from the early universe.

CMB follows a flat blackbody distribution to the zeroth order. The small anisotropies of the CMB radiation can be decomposed into angular power spectrum. A cosmological model with DM parameters, called ΛCDM, provides an excellent fit to the observed CMB power spectrum. Parameters such as baryonic and DM densities can be extracted from this fit. State-of-the-art measurement of the CMB power spectrum reveal that roughly 63% of the matter in the Universe is in the form of DM.

Two remarks are in order here:

First, the Λ in ΛCDM symbolizes the "dark energy", which contributes approximately 68% of the total energy/mass density of the current Universe. The density of dark energy is indeed best derived based on CMB fitting. CDM means Cold Dark Matter, which is a basic assumption of this model. We will discuss the meaning of "cold DM" and possible deviations from this assumption below.

Secondly, as briefly mentioned, the "missing mass phenomena" from astrophysical observations such as galaxy rotation curves and velocity dispersion was thought of as a possible indication of Newtonian Gravity needing modification at the galactic scale. A series theories of modified gravity have been proposed to explain the effect, collectively called Modified Newtonian dynamics (MOND). MOND has not been able to explain the cosmological observations, such as CMB power spectrum,

as well as gravitational lensing so far, but is still an active research topic.

DM can also have significant effects on the structure of the universe. There are different scales of sizes in Cosmology. Galaxies are formed of around 10^8 (dwarfs) to 10^{14} (giants) stars, 1 kpc to 100 kpc in diameters. Galaxy clusters are formed of hundreds to thousands of galaxies in a 2 - 10 Mpc size. Above these, there is superclusters that have sizes of above 100 Mpc. The evolution of these structures, from the small seeds of perturbation predicted in the very early universe to the coalescence in the later stage, is called "structure formation" in Cosmology.

DM provides gravitational potentials for the structures to form. If the universe consisted of only the normal visible matter, it would remain dominated by the relativistic or semi-relativistic species for too long, given the temperature evolution. The relativistic species would wash out the density contrast and prevent structures from forming. The proper DM abundance, consistent with the ΛCDM best fit value, would allow the Universe to enter the non-relativistic matter domination era (known as "matter domination") early enough for the structure to form. This requires the DM to be non-relativistic, or "cold", at the time when structure is forming, thus gives the name cold dark matter (CDM).

Hot (relativistic) or warm (semi-relativistic) DM models are disfavored by structure formation in a quantitative fashion, but there are models with DM temperatures higher than traditional CDM that are still consistent with the structure formation history, if the temperature drops fast enough in the later stage. ELDER DM is a good example, as introduced in section 1.4 and further detailed in Chapter 2.

Finally, the Bullet Cluster (1E 0657-56) provides a relatively recent yet incred-

ibly strong evidence of DM, which cannot be explained by alternative theories like modified gravity. The Bullet Cluster is considered a merger of two galaxy clusters. Based on the x-ray image and gravitational lensing, one can see a clear mismatch in the spatial distortion of the gravitating matter (from lensing) and the visible matter (from x-ray).

Furthermore, the observation of the Bullet Cluster also gives constraints on both DM-SM interaction and DM-DM self-interaction. In particular, since the dark matter particle collisions leads to significant mass loss in the cluster, the consistency of the subcluster mass-to-light ratio with respect to the value from the main cluster constrains the DM self interaction to $\sigma/m \lesssim 1\ \mathrm{cm}^2/\mathrm{g}$ [15], which actually puts a strong constraint on strongly self-interacting DM like ELDERs [1,2].

Note that I only discussed several of the most important pieces of evidence for the existence of DM here. There are various other observations that indicate the existence of DM that can be found in [16].

Now, let me summarize the valuable information concerning the properties of DM that these observations revealed:

- Gravitational interaction:

  The gravitational interaction, or simply the mass/energy of DM, are crucial to explaining physics at galactic and cosmological scales. Observations are consistent with DM gravitational interactions described by standard General Relativity.

- Constraints on non-gravitational interactions:

  There is currently no evidence of any interaction of DM outside of the gravitational interaction. Furthermore, the DM-SM interactions and DM-DM

self-interactions are both highly constrained by the aforementioned astrophysical/cosmological measurements.

- Coldness of dark matter:

  DM cannot be too hot (relativistic) that it destroy the formation of the structure of the Universe. Cold (non-relativistic) DM models (especially the Λ CDM model) are in great agreement with the observations on large-scale structure.

1.3 WIMP Dark Matter and Other Thermal Relics

Our knowledge about DM, as discussed above, is limited to its gravitational interaction. However, it is interesting to postulate DM candidates with other feeble but non-zero interactions with SM, that is consistent with the observations briefly discussed in section 1.2. One hypothetical category that many of such DM candidates fall into is "thermal relics", meaning that the DM particle was once thermalized and in equilibrium with the SM particle bath, in the early universe, when the interaction rate exceeds the Hubble expansion rate due to high densities of the DM/SM species and high temperature. The DM particles abundance than "freezes out", as the DM interaction rate with the SM particles becomes lower than the Hubble expansion rate. The DM current-day abundance is thus calculable since the DM comoving density remains almost constant after the freeze-out.

From here on, we denote DM particle as χ for simplicity, assuming only one species of DM. The simplest models of this form usually have one important interaction in which the DM particle number changes:

- Annihilation: $\chi+\chi \leftrightarrow$ SM+SM, where SM stands for known Standard Model particles.

When the annihilation rate of $\chi + \chi \leftrightarrow$ SM+SM drops below the Hubble rate, the freeze-out happens. The DM-SM interaction strength is determined by three important factors: the SM particle number density n_γ, the DM number density n_χ, and the thermally averaged interaction cross section $\langle \sigma v \rangle$. The freeze-out usually happens when the DM particles become non-relativistic, since n_χ becomes exponentially suppressed by the Boltzmann factor, $e^{-m_\chi/T}$. Thus, assuming the standard cosmological history of temperature evolution, the mass of the DM m_χ and the interaction cross-section $\langle \sigma v \rangle$ determine the final relic abundance.

The weakly-interacting massive particle (WIMP) paradigm comes as a direct consequence of studying the thermal relics that rely on the freeze-out of the DM annihilation to set the current DM abundance. One finds that based on the simple assumption of freeze-out, the correct abundance of dark matter can be set by the DM annihilation cross section around $\langle \sigma v \rangle \simeq 3 \times 10^{-26} \mathrm{cm}^3\ \mathrm{s}^{-1}$. For a DM particle around TeV mass range, this would point to a DM-SM interaction of the strength close to the SM weak-interaction strength. This is why WIMP is "wealy-interacting". It is called a "massive" particle, again, because it freezes out non-relativistically.

In the past, the WIMP paradigm became widely popular given its natural connections to solutions of Higgs hierarchy problem, e.g. Supersymmetry [17], and to the collider experiments, e.g. LHC, probing new physics around the TeV scale. As the hope of finding TeV Supersymmetry dwindles and the LHC is reaching its designed capacity, theorists are starting to think about other scenarios that are equally intriguing but less experimentally constrained.

Now that we introduced WIMP, let's mention another DM-SM interaction that exists for most of the thermal relics:

- Elastic Scattering: χ+SM $\leftrightarrow$ χ+SM, where "SM" stands for any of the known Standard Model particles.

This interaction does not change number density and usually decouples after the freeze-out, so it can be neglected when determining the DM relic abundance. However, this interaction is crucial in keeping the DM and SM particles thermalized. The decoupling of this interaction could in principle allow DM to have a different temperature from the SM particles. In the next section, we will introduce a new DM paradigm, in which the early decoupling of elastic scattering is actually crucial in setting the DM relic abundance.

Finally, let us mention another kind of thermal relic that was considered [18], that is not freezing out through DM annihilation. Instead, the number changing process that the DM freeze-out with is an n DM particles to 2 DM particles ($n > 2$) self-annihilation:

- Self-Annihilation: $\overbrace{\chi \dots \chi}^{n} \leftrightarrow \chi\chi$, with $n \geq 3$.

This class of models was originally referred to as "self-interacting dark matter" or SIDM [18]. The term SIDM was later referred to as a different class of models relying on DM self-interaction to explain astrophysical anomalies [19], as discussed in more details in the next section. The modern incarnation of the original self-annihilating SIDM is called Strongly-Interaction Massive Particle (SIMP) [20]. The word "strong" describes the DM self-interaction, which needs to be strong

enough to change its number density. Incidentally, the name SIMP may also not an optimal choice of naming since it was also originally used to describe DM strongly interacting with visible SM matter (without considering the DM self-interaction) [21]. The next section contains a very brief review of these dark matter candidates.

1.3.1 Family of Self-Interacting or Strongly Interacting Dark Matter

There are generally two different types of dark matter called self-interacting dark matter (SIDM). The first SIDM model (to the knowledge of the author) was proposed by Carlson, Machacek, and Hall [18] (we can thus call it CMH SIDM). The DM assumes no interaction with SM particles before freezing out. The self-interaction is strong, and the dark matter freezes out through the three-to-two (or n-to-2, with $n > 3$) self-interaction, as described in the previous section. This has implications for the dark matter mass (light dark matter is preferred) and could have significant effects on large-scale structure [22]. Later on, simulations/observation revealed that there could be potential tension between the cold DM and small-scale structure measurement (see, e.g. [23]). Spergel and Steinhardt [19] proposed to use DM self-interaction (which could also be quite strong in strength in comparison to weak interactions) to resolve this tension. This kind of dark matter is often referred to as SIDM as well.

The two SIDM both have strong self-interactions, but they are aiming for different goals. One is devising a new way to set the DM relic abundance, and the other is to resolve the CDM small-scale structure problems. The Spergel-Steinhardt

SIDM also has strong $2 \to 2$ self-interaction as mentioned, but it does not require a number-changing process.

Now let's move on and discuss "SIMP" (Strongly Interacting Massive Particles), which could have completely different meanings in different sources[1]. Originally, the term Strongly Interacting Massive Particles (SIMPs) [25], was used to describe DM with strong interactions with normal/visible/Standard Model matter. Given its strong interaction, it is often shielded from the underground DM detectors by its interaction with dirt and other earth materials, avoiding constraints from direct-detection experiments. Fast forward to 2014, a new kind of "SIMP" paradigm was developed [20], closely related to the idea of the original CMH SIDM. The DM freezes out through the 3 to 2 or 4 to 2 interaction, but is always thermalized with SM particles during the freeze-out process. This paradigm points to a sub-GeV DM candidate with strong self-interaction roughly of the nuclear-interaction strength. This modern SIMP has generated strong interest in model building, based on the ideas of dark sector (connected to the SM particles by some dark mediators to thermalize with SM matter) and dark QCD (to describe the required strong self-interaction).

1.4 Beyond the WIMP/Freeze-out Paradigm: Elastically Decoupling Relics

As mentioned in the previous section, for most known DM models, the DM relic abundance is set by processes that change the χ particle number. In this section,

[1] It is worth noting that in some occasions, the Spergel-Steinhardt type SIDM is also referred to as SIMP [24], which only adds to the confusion.

we present a novel scenario in which the dark matter relic density is determined almost entirely by the decoupling of the *elastic scattering*, and we call this scenario "ELastically DEcoupling Relic", or ELDER.

The ELDER scenario considers the two interactions mentioned above, elastic scattering between DM and SM and $n \to 2$ number-changing DM self-annihilation. When DM is relativistic, it stays in thermal and chemical equilibrium with the SM particle bath. When it becomes non-relativistic, the elastic scattering first decouples, meaning that DM-SM interaction becomes too weak to keep DM and SM sectors at the same temperature. The DM then enters the self-heating era, which was first discussed in the original SIDM paper [18]. During this era, the energy released by self-annihilation keeps the DM particles at an approximately constant temperature as the universe continues to expand, and the comoving entropy of the DM sector is conserved. This drastically slows down the decrease of comoving number density as well. Finally, the self-annihilation process also freezes-out, at which point the comoving number density of χ actually freezes. But as will be shown in Chapter 2, the final relic abundance depends much more on the early elastic decoupling (exponentially) compared to the freeze-out of the number-changing self-annihilation (logarithmically), and thus we call the DM *ELastically DEcoupling Relics*. We will demonstrate this point by conducting analytic calculations as well as solving coupled Boltzmann equations numerically.

We found that the current dark matter abundance can be successfully produced in this scenario, with all theoretical and observational constraints satisfied, for χ masses between a few and a few hundred MeV. The cross-section of elastic scattering between DM and SM particles (electrons, photons, and/or neutrinos) is of the order of $10^{-3} - 1$ fb in the non-relativistic limit, which can be easily achieved,

by considering DM-SM interactions mediated by dark photons [2]. The strong self-interaction required for the ELDER scenario could be achieved by considering QCD-like theory in the dark sector [26].

One of the most exciting features of the ELDER scenario is that, based on a specific DM mass, it points to a very precise elastic scattering strength. This means that ELDER provides a robust target for DM direct detection, which relies on the elastic scattering of the DM with SM particles. The ELDER predictions define a well-defined target region in the parameter space for direct-detection and dark photon experiments (assuming the DM-SM interaction is mediated by a dark photon). These features are reported in detail in Section 2.3. In particular, Figs. 2.3 and 2.4 show the main results of the ELDER phenomenology.

1.5 New Searches for Dark Matter with Neutron Stars, Black Holes, and Their Mergers

As discussed in section 1.2, astrophysical observations present some of the major evidences for DM. It is thus very interesting to consider other astrophysical observations in hopes of unveiling the non-gravitational interactions for DM particles. Given the high density of neutron star, DM with very feeble interactions with nucleons can trigger dramatic phenomena for this stellar system. Several astrophysical searches may be used to unveil DM that implodes neutron stars [27–31], thereby creating r-process elements [32], and plausibly fast radio bursts [33]. Fortuitously, the unprecedented sensitivity of laser interferometer gravitational wave detectors at LIGO/VIRGO [34], the broad optical purview of DES [35,36], BlackGEM [37], and the Zwicky Transient Factory (ZTF) [38], as well as kilo-channel

radio reception at the CHIME [39] and HIRAX [40] arrays, are all opening new windows onto the dynamics of neutron stars and black holes.

Thus, in Chapter 3, we consider distinct signatures of DM-induced NS implosions, which may be found by upcoming gravitational, optical, and radio surveys. In particular, we will discuss how to utilize the distribution of NS mergers in the galaxies, to probe DM-nucleon interaction cross-sections 4 to 10 orders of magnitude smaller than the direct detection experiment sensitivity on a few-years timescale.

We also consider other direct and indirect signatures of implosions, including "Quiet Kilonovae" and "Black Mergers" (NS-mass black hole mergers). LIGO and Virgo detectors currently have the sensitivity to probe the light black hole mergers, which would be an exciting search both in its own right and as a complimentary piece to the NS merger search to probe the NS implosion scenarios.

1.6 ν Hopes for New Physics: Experimental Probes of Hidden Particles

Light (sub-GeV) and weakly interacting particles could explain both experimental anomalies (e.g., using dark photons to explain g-2 anomaly [41]) and account for theoretical issues (e.g. axion as a solution for the strong CP problem). In addition, weakly interacting particles may arise as a part of the "dark sector", that are not necessarily the main components of the DM relic abundance, but could, for example, facilitate interaction between DM and SM particles. For instance, as discussed in section 1.4, a dark photon could be included in an ELDER scenario to

mediate the DM-SM interaction. The experimental program of searches for weakly coupled states has undergone a strong revival in recent years [42].

Examples of well-motivated weakly interacting particles, including sterile neutrinos, QCD axion, axion-like particles, dark photons, and dark scalars, can be searched for in a variety of particle physics experiments (see, *e.g.* [43–51]). Since these particles interact very weakly with SM particles, one way to detect them is to utilize experiments with high statistics. Even when the particles are produced very weakly and/or deposit small amounts of energy in the detector, such experiments have a chance to detect them. There are roughly two kinds of setups considered high-statistics experiments in particle physics. One would be fixed target/beam dump-type experiments, usually downstream of a beam-line, that can collect a large number of protons/electrons on target [52]. A different direction would be having a detector with high volume, low background, and long exposure time, in order to catch rare events. Neutrino experiments are perfect for the purposes of detecting hidden particles, which is not surprising since neutrinos are themselves very weakly interacting particles in the Standard Model.

Going along this direction, one of the most promising avenues for exploring very light and very weakly coupled states is by performing experiments in either deep underground laboratories, where the external backgrounds are very low, or large detectors built for the purpose of studying solar neutrinos. With the solar neutrino program currently measuring the last components of the neutrino flux, the usage of these large detectors shifts onto new applications. Thus, the KAMLAND and SNO+ detectors are (or will be) used to study double beta decays of Xe and Te isotopes [53, 54]. The Borexino detector will see the expansion of its program to include the sterile neutrino searches when new powerful external beta-decay

sources are placed nearby [55].

There are also interesting proposals based on a possible usage of accelerators underground. Currently, relatively modest accelerators in terms of the energy and current intensity are used in the underground laboratories for measuring the nuclear-astrophysics-relevant reactions [56] or for calibration purposes [57]. These efforts can be significantly expanded. Powerful accelerators next to large neutrino detectors could open a new way of exploring the nature of light weakly coupled sectors [58–62].

In Chapter 4, we concentrate on the Borexino-SOX project that uses a radioactive ^{144}Ce$-^{144}$Pr source in close proximity to the detector. It has been pointed out that the same configuration will be sensitive to the emission of light scalar (or vector) particles in the transitions between the nuclear levels in the final point of the β-decay chain [60]. We revisit the question of sensitivity of Borexino-SOX to light particles, and update several aspects of [60]. We greatly improve the sensitivity reaches by taking into account the decays of light particles inside the Borexino detector. Only scalar scattering on electrons was taken into account in the previous studies.

In Chapter 5, we present a comprehensive study of experimental constraints and future sensitivity reaches on heavy neutral leptons (HNL), with neutrino-HNL-photon dipole interactions. Such HNL has been proposed to explain the LSND and MiniBooNE anomalies [63–65], and is a five-dimensional operator/portal for the SM particles to interact with the hidden sectors. We take into account data from LEP, LHC, MiniBooNE, and LSND, and consider the constraints from Supernova 1987A and Big Bang Nucleosynthesis (BBN). We also derive projected sensitivities from the proposed Search for Hidden Particles (SHiP) experiment and the ongoing

Short-Baseline Neutrino (SBN) experiments at Fermilab. Dipole mediated Primakoff neutrino upscattering and Dalitz-like meson decays are the primary production channels in our study. The detection signature is from the decay of HNLs into a photon and a neutrino. Thus understanding the single photon background in each experiment is crucial for this analysis.

1.6.1 Charge Quantization and Millicharged Particles

Fundamentally, charges under U(1) gauge group, unlike charges under compact non-abelian groups, do not have to be quantized (i.e., they do not need to be a multiple of a fundamental unit). However, it has long seen thought that electron (or positron) charge represents the minimal charge under $U(1)_{\rm em}$. This inspired the famous Dirac string/monopole argument to explain the empirically observed charge quantization, in terms of the electron charge e.

The hypothesis of charge being quantized in units of electron charge was shattered by the evidence for the existence of quarks, which carry a minimal charge of $e/3$. However, a broader sense of charge being quantized in a fundamental unit (currently believed to be at most $e/3$), still motivates models, such as Grand Unification Theories, that provide an explanation.

A long-standing program of experimental searches for millicharged particles [66] has aimed to test this hypothesis. The goal could be viewed as twofold: 1) testing the narrow sense of charge quantization, in terms of the minimal quark charge $e/3$. 2) if smaller charges are possible, finding the particle that possess the minimal charge. Philosophically, one can never completely disprove the concept of "charge quantization" in general, because whatever small electric charges we might find

can be viewed as the new quanta for electric charge. But one can certainly make the concept unattractive by finding smaller and smaller charges, or a charge with a random real number in unit (e.g., 0.17 e, if the experimental sensitivity permits). Outside of the charge quantization, millicharged particles have also attracted some attention in other contexts in modern particle physics, e.g., as a candidate for dark matter (see, e.g., [45, 47, 67]).

In [6], my collaborators and I pointed out a new direction for probing millicharged particles, in the neutrino experiments. The millicharged particle can be produced in meson decays, and leave a detection signatures in neutrino detectors through its elastic scattering with the electrons. This will be discussed in Chapter 6.

CHAPTER 2

ELASTICALLY DECOUPLING RELICS

2.1 Introduction

In this chapter, we study the Elastically Decoupling Relic (ELDER) dark matter. ELDER is a thermal relic whose present density is determined primarily by the cross-section of its elastic scattering off Standard Model (SM) particles. Assuming that this scattering is mediated by a kinetically mixed dark photon, we argue that the ELDER scenario makes robust predictions for electron-recoil direct-detection experiments, as well as for dark photon searches. These predictions are independent of the details of interactions within the dark sector. Together with the closely related Strongly-Interacting Massive Particle (SIMP) scenario, the ELDER predictions provide a physically motivated, well-defined target region, which will be almost entirely accessible to the next generation of searches for sub-GeV dark matter and dark photons. We provide useful analytic approximations for various quantities of interest in the ELDER scenario, and discuss two simple renormalizable toy models which incorporate the required strong number-changing interactions among the ELDERs, as well as explicitly implement the coupling to electrons via the dark photon portal.

Cosmological observations at a variety of length scales, from individual galaxies to the Hubble scale, indicate that most of the matter in the universe is in the form of dark matter (DM). DM cannot consist of any of the known elementary particles, and its existence provides solid experimental evidence for physics beyond the Standard Model (SM). The microscopic nature of dark matter is one of the major mysteries in fundamental physics. For many years, both theoretical work

and experimental searches for dark matter focused on a short list of possible candidates independently motivated by particle physics—primarily QCD axions and weakly-interacting massive particles (WIMPs) realized within supersymmetry or other extensions of the SM at the weak scale. Despite decades of experimental effort, no evidence for these candidates has been found. While neither WIMP nor axion dark matter is ruled out and the experimental searches are ongoing, there has been renewed interest in exploring alternative particle dark matter candidates.

A promising new direction is to consider models in which dark matter particles have strong number-changing self-interactions [1, 18, 20, 68–82]. If the DM is a thermal relic, its current density in such models can be determined either by the cross section of the number-changing self-interaction processes ("Strongly-Interacting Massive Particle", or SIMP, scenario [83]) or by the cross section of elastic scattering between the DM and SM ("Elastically Decoupling Relic", or ELDER, scenario [1]). In both cases, the observed DM density is naturally obtained if the mass of the DM particles is parametrically close to the QCD confinement scale, $m_{\rm DM} \sim 10 - 100$ MeV. This leads to an attractive particle physics framework: a "dark sector" of fields not charged under the SM gauge groups, containing a non-Abelian "dark QCD" gauge group that confines at a scale similar to $\Lambda_{\rm QCD}$. The proximity of the SM and "dark" confinement scales may be due to a discrete symmetry relating the dark QCD gauge coupling to the SM g_3 at a high energy scale [84–88]. The dark matter may then consist of mesons that emerge from dark QCD upon confinement [20]. If the dark sector also contains an Abelian gauge field, kinetic mixing between this field and the SM electromagnetic field naturally provides the requisite interaction between the dark matter particle and the SM, via the dark photon portal [69, 72].

The goal of this chapter is to study the above possibilities in more detail, in particular, the ELDER scenario proposed in Ref. [1]. In Ref. [1], we demonstrated the viability of this scenario in a general framework, without reference to a specific model of either the dark sector or the portal connecting it to the SM. Instead, we used a simple parametrization of the DM number-changing self-scattering and DM-SM elastic scattering cross sections. Moreover, the analysis of Ref. [1] was primarily based on numerical solution of Boltzmann equations. Here, we expand that analysis in several directions:

2.2 ELDER Dark Matter

Consider a particle χ with mass m_χ[1]. The χ particles can undergo the following processes:

I Elastic scattering: χ+SM $\leftrightarrow$ χ+SM, where "SM" stands for any of the Standard Model particles. (In practice, the important SM states are those with mass below m_χ; for ELDERs, this will typically include electrons, photons, and neutrinos.)

II Annihilations to SM: $\chi + \chi \leftrightarrow$ SM + SM.

III "$3 \to 2$" Self-Annihilations: $\chi\chi\chi \leftrightarrow \chi\chi$.

IV "$2 \to 2$" Elastic Self-Scattering: $\chi\chi \leftrightarrow \chi\chi$.

[1]This may be a single state, or a set of mass-degenerate states χ_i. In the latter case, appropriate averaging over the particle "flavor" is implicit in the discussion of this section, and the "flavor indices" are suppressed for clarity.

We assume that in the early universe at temperatures above m_χ, all four reactions are "active", *i.e.* occur in the plasma at rates $\Gamma > H$. This means that the ELDERs have a thermal energy distribution (thanks to reaction 4), zero chemical potential (reaction 3), and temperature equal to that of the SM plasma (reactions 1 and 2), which we denote by T. The ELDER number density follows the equilibrium trajectory, $n^{\rm eq}(T)$. As the temperature drops below m_χ, the ELDERs become non-relativistic, and the equilibrium density drops exponentially, $n^{\rm eq}(T) \propto e^{-m_\chi/T}$. The rates of the reactions 2, 3, and 4, drop off exponentially, while the reaction 1 slows more gradually.

All the reactions eventually decouple, $\Gamma \lesssim H$, but the order of decoupling is crucially important in determining the relic abundance. It is natural for $3 \to 2$ self-annihilation to decouple before $2 \to 2$ self-scattering: the interaction strengths entering the two rates are generically of the same order (both involve interactions internal to the dark sector), but $\Gamma_{3\to2} \propto n_\chi^2$ while $\Gamma_{2\to2} \propto n_\chi$. On the other hand, the rate of annihilations to SM, $\Gamma_{\rm an}$, is controlled by the coupling between the SM and the dark sector, which can naturally be small. (For example, in the dark photon portal model considered below, this will be controlled by kinetic mixing between the SM and dark-sector $U(1)$ gauge groups.) In this chapter, we will consider the regime where annihilations to SM decouple *first*, while the $3 \to 2$ process is still active. This is the case in both the SIMP and ELDER scenarios.

The rate of elastic scattering $\Gamma_{\rm el}$ is proportional to the SM density, which is not exponentially suppressed at $T < m_\chi$. However, the scattering cross section is suppressed by the small coupling between the SM and χ. Generically, this cross section is of the same order as that of annihilations to SM, and therefore decoupling of elastic scattering occurs after annihilations to SM are decoupled. Depending on

the relative strength of the SM-χ coupling and χ self-couplings, the decoupling of the elastic scattering may occur either after or before the decoupling of the $3 \to 2$ self-annihilation. The former case corresponds to the SIMP scenario [83], while the latter is the ELDER scenario [1].

2.2.1 The Thermal History of ELDERs

After annihilations and elastic scattering with the SM decouple, but while the $3 \to 2$ and $2 \to 2$ self-interactions are still active, the ELDERs are still in thermal equilibrium at zero chemical potential, but their temperature T' no longer has to be the same as the SM plasma temperature T. As shown in Appendix B, the two temperatures are related by

$$\frac{\partial T'}{\partial T} = 3\frac{T'^2}{m_\chi T} + a\left(\frac{T}{m_\chi}\right)^{1+n}\frac{T'^2}{m_\chi^2}\frac{(T'-T)}{m_\chi}, \tag{2.1}$$

where

$$a \equiv \frac{c_n g_\psi^2 g_\chi N_{3+n}^\psi}{32\pi^3}\,\frac{M_{\rm Pl}}{1.66 g_{*,d}^{1/2} m_\chi}. \tag{2.2}$$

Here ψ is the SM particle that couples to χ, with corresponding number of degrees-of-freedom g_ψ and g_χ, respectively; N_{3+n}^ψ is a numerical constant given in Eq. (A.17). We assume that the effective number of relativistic degrees of freedom $g_{*,d}$ remains constant throughout the decoupling process. (The case of varying g_* can be handled numerically.) The *"elastic scattering strength"* c_n is defined as the dimensionless coefficient of the leading term in the low-energy expansion of the matrix element-squared of the elastic scattering process $\chi\psi \leftrightarrow \chi\psi$:

$$|\mathcal{M}|^2_{\substack{t=0 \\ s=m_\chi^2+2m_\chi E_\psi}} \equiv c_n\left(\frac{E_\psi}{m_\chi}\right)^n + \ldots, \tag{2.3}$$

where $|\mathcal{M}|^2$ is averaged over initial and final-state degrees of freedom, including spin, color, and electric charge. (See Appendix A for details.) If χ couples to more

than one SM particle, a summation over the relevant SM species is implied in the definition of a. The formalism presented here is applicable to SM particles that are relativistic at the time of χ decoupling, $m_{\rm SM} \ll T_d \sim m_\chi/10$. SM particles with $m_{\rm SM} \gg T_d$ are irrelevant to the decoupling process, while the case $m_{\rm SM} \sim T_d$ can be studied numerically.

An approximate analytic solution to the temperature evolution equation can be found (see Appendix B):

$$x' = e^t \left(\left(\frac{a}{n+4} \right)^{\frac{1}{n+4}} \Gamma \left(\frac{n+3}{n+4}, t \right) - \frac{3\mathrm{Ei}(-t)}{n+4} \right) , \tag{2.4}$$

where $x = m_\chi/T$, $x' = m_\chi/T'$, and $t = \frac{a x^{-n-4}}{n+4}$. At small x, $x' \approx x$, corresponding to SM and ELDER sectors in thermal equilibrium. At large x, the asymptotic form of the solution is

$$x' \approx 3\log(x) + \left(\frac{a}{n+4} \right)^{\frac{1}{n+4}} \Gamma \left(\frac{n+3}{n+4} \right) - 3\log \left[e^{\frac{\gamma_E}{n+4}} \left(\frac{a}{n+4} \right)^{\frac{1}{n+4}} \right]. \tag{2.5}$$

Identifying the “decoupling temperature" at which the ELDER and the SM thermally decouple,

$$T_d = m_\chi \frac{\left(\frac{n+4}{a} \right)^{\frac{1}{n+4}}}{\Gamma \left(\frac{n+3}{n+4} \right)}, \tag{2.6}$$

Eq. (2.5) can be rewritten as $x' \simeq x_d + 3\log(x/x_d)$, or

$$T' \simeq \frac{T_d}{1 + 3\frac{T_d}{m_\chi} \log \frac{T_d}{T}}. \tag{2.7}$$

This is precisely the behavior expected in the “cannibalization" regime [18], where ELDER temperature decreases only slowly (logarithmically with the scale factor) as the universe expands. The physical reason is that the kinetic energy released by $3 \to 2$ self-annihilations partially compensates for the energy lost when particle momenta are redshifted due to the expansion. This regime persists until the $3 \to 2$ process decouples, after which the ELDER density is frozen out. Note that the

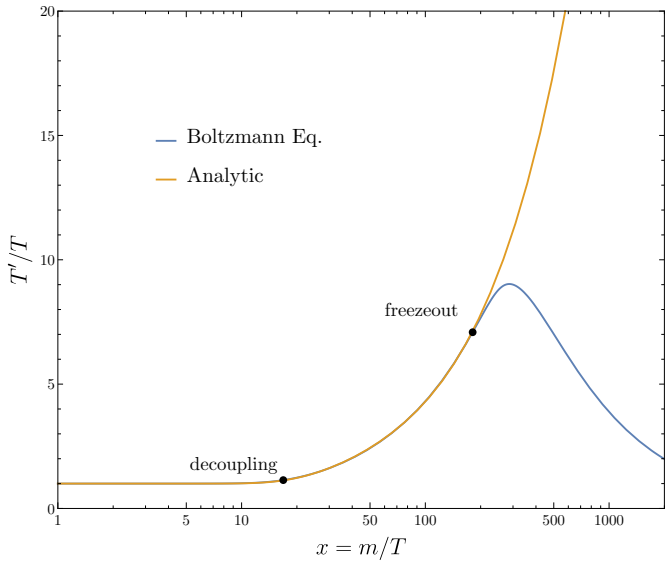

Figure 2.1: Evolution of the ratio of ELDER temperature T' to the SM plasma temperature T. Here $m_\chi = 10$ MeV, $c_2 = 1.3 \times 10^{-14}$, $\alpha = 5$, $g_\chi = 2$, and $g_\psi = 4$.

dark matter particles remain non-relativistic throughout the cannibalization period, so that from the point of view of Cosmic Microwave Background (CMB) and structure formation, ELDER is a Cold Dark Matter (CDM) candidate, consistent with observations.

The evolution of ELDER temperature throughout the kinetic decoupling and freeze-out process is illustrated in Fig. 2.1. The ELDER-to-SM temperature ratio starts growing after kinetic decoupling due to cannibalization, reaching the maximum value of $T'/T \sim 10$ at the time of freeze-out. It drops rapidly after freeze-out since ELDERs are non-relativistic and $T' \propto R^{-2}$, while $T \propto R^{-1}$, where R is the size of the universe. The analytic function (2.4) provides an excellent approximation to the numerical solution of the Boltzmann equations up until $3 \to 2$ freezeout.

We note that Eq. (2.7) can also be derived by assuming instantaneous kinetic decoupling between the dark sector and the SM at temperature T_d, and using the

conservation of comoving entropy in the dark sector after decoupling. This approach was taken, for example, in Ref. [1]. The alternative derivation presented here does not make the assumption of instantaneous decoupling, relying instead on the approximate solution for the evolution of T' accurate throughout the decoupling process. Apart from being better justified physically, the distinct advantage of the new derivation is that it automatically provides the expression for T_d in terms of the underlying model parameters, Eq. (2.6).

In the instantaneous freeze-out approximation, the asymptotic value of the yield $Y_\chi = n_\chi/s_0$, where s_0 is the entropy density today, is given by

$$Y_\infty = Y_{x_f} = \frac{g_\chi (2\pi x'_f)^{-3/2} e^{-x'_f}}{(2\pi^2/45) g_{*s,f} x_f^{-3}}, \tag{2.8}$$

where x_f and x'_f are the temperatures of the SM and the ELDERs, respectively, at the time of freeze-out. The effective multiplicity at freeze-out, $g_{*s,f}$, is strongly dominated by the SM degrees of freedom that are relativistic at that temperature, and the ELDER contribution to entropy is negligible; for typical ELDER parameters, $g_{*s,f} = 10.75$. The ELDER relic density is given by

$$\Omega_\chi h^2 \simeq 3 \times 10^6 \left(\frac{m_\chi}{10 \text{ MeV}}\right) Y_\infty \simeq 4 \times 10^5 \left(\frac{m_\chi}{10 \text{ MeV}}\right) \frac{g_\chi}{g_{*s,f}} \frac{x_d^{3/2} e^{-x_d}}{\left(1 + \frac{3}{x_d} \log \frac{x_f}{x_d}\right)^{3/2}}, \tag{2.9}$$

where x_d is the decoupling temperature defined in Eq. (2.6).

The $3 \to 2$ self-annihilations freeze-out when $n_\chi^2 \langle \sigma_{3\to 2} v^2 \rangle \simeq H$. Let us parametrize

$$\left\langle \sigma_{3\to 2} v^2 \right\rangle \equiv \frac{\alpha^3}{m_\chi^5}. \tag{2.10}$$

The freeze-out and decoupling temperatures can then be estimated by solving the

equations

$$x'_f + \frac{9}{4}\log x'_f \simeq 31.0 - \frac{x_d}{2} - \frac{3}{4}\log\left(\frac{m_\chi}{10\text{ MeV}}\right) + \frac{9}{4}\log\alpha + \frac{3}{2}(\log x_d + \log g_\chi - \frac{1}{4}\log\frac{g_{*,f}}{10}) \tag{2.11}$$

and

$$x_d - 3\log x_d \simeq 12.9 - \frac{3}{2}\log x'_f + \log g_\chi - \log\frac{g_{*s,f}}{10} + \log\left(\frac{m_\chi}{10\text{ MeV}}\right) - \log\left(\frac{\Omega_\chi h^2}{0.1}\right). \tag{2.12}$$

Numerically, $x_d \simeq 17$ and $x'_f \simeq 25$ for a typical ELDER model. The decoupling temperature is directly related to the strength of elastic scattering between ELDERs and SM particles, see Eqs. (2.2), (2.6). Once x_d is found by solving Eq. (2.12), it is straightforward to compute the corresponding elastic scattering strength:

$$\bar{c}_n \simeq (1.4\times 10^{-18})\,\frac{g_{*,d}^{1/2}\xi_n}{g_\chi g_\psi^2}\,\left(\frac{m_\chi}{10\text{ MeV}}\right)\,x_d^{n+4}, \tag{2.13}$$

where $g_{*,d}$ is the effective number of relativistic degrees of freedom at T_d, and $\xi_n = (n+4)[\Gamma(\frac{n+3}{n+4})]^{-n-4}/N^{\psi}_{3+n}$ is a numerical constant. (For future reference, $\xi_0 \simeq 0.08$ and $\xi_2 \simeq 0.004$.) Once a mechanism that mediates ELDER-SM scattering is specified, this formula can be used to make detailed, robust phenomenological predictions, as discussed in the next Section. Remarkably, such predictions are almost completely independent of the details of self-interactions of ELDERs, or their interactions with other dark sector states.

2.2.2 ELDER Mass Estimates

A model-independent upper bound on the ELDER dark matter particle mass can be obtained as follows. Self-consistency of the ELDER scenario requires $x_f > x_d$,

or[2]

$$\alpha \gtrsim 0.5 \frac{m_\chi}{10 \text{ MeV}}. \tag{2.14}$$

Here we see that ELDER dark matter is pushed to the strongly interacting regime ($\alpha \gtrsim 1$). The thermally averaged $3 \to 2$ rate can be bounded above by unitarity, in similar spirit to the bound derived on the thermally averaged WIMP annihilation rate [89]. The optical theorem states that

$$2 \text{ Im} \, \mathcal{M}_{\text{forward}} = \sum_X \int d\Pi_X (2\pi)^4 \delta^4(p_i - p_X) |\mathcal{M}_{\chi\chi \to X}|^2, \tag{2.15}$$

where $\mathcal{M}_{\text{forward}}$ is the matrix element for forward scattering $\chi\chi \to \chi\chi$, and $d\Pi_X$ is the Lorentz invariant phase space. Picking the term with $X = \chi\chi\chi$ from the sum yields the inequality

$$\int d\Pi_X (2\pi)^4 \delta^4(p_i - p_f) |\mathcal{M}_{3\to 2}|^2 < 2 \text{ Im} \, \mathcal{M}_{\text{forward}}. \tag{2.16}$$

Using this in the definition of the thermally averaged rate in Eq. (A.7), in the non-relativistic limit, the rate is bounded above by

$$\left\langle \sigma_{3\to 2} v^2 \right\rangle \lesssim \frac{\sqrt{15}\pi}{6 T^3 m^4} e^{3m/T} \int_{9m^2}^{\infty} ds \, e^{-\frac{\sqrt{s}}{T}} \text{Im} \left(\mathcal{M}_{\text{forward}}(s) \right). \tag{2.17}$$

In the absence of light degrees of freedom, non-relativistic elastic scattering of scalar χ particles is typically dominated by the s wave. Partial-wave unitarity requires[3] $|\mathcal{M}_{\text{forward}}| \leq 8\pi\sqrt{s}/p \simeq 48\pi/\sqrt{5}$, which in turn implies (taking into

[2] Close to this bound, the kinetic decoupling and freeze-out occur close in time, and the formulas derived in this Section, which assumed a clear separation between the two events, are not strictly applicable. The bound on α for "pure ELDER" regime, in which the separation is clear, is stronger by a about a factor of 2. For smaller α, a "mixed SIMP-ELDER" regime occurs, which does not lend itself to simple analytic estimates. Numerical analysis of this regime indicates a smooth connection between "pure SIMPs" and "pure ELDERs", see for example Fig. 2.2.

[3] At $\sqrt{s} = 3m$, the χ particles are moderately relativistic, $\beta^2 \sim 0.5$, and corrections to s-wave scattering amplitude may be non-negligible. This will affect the unitarity bound at the level of order-one factors. Thus, this bound as well as the mass bound in Eq. (2.19) should be viewed as order-of-magnitude estimates.

account the typical freeze-out temperature $x'_f \simeq 20$) an upper bound

$$\alpha \lesssim 73. \tag{2.18}$$

where α is defined in Eq. (2.10). Combining this bound with Eq. (2.14) yields

$$m_\chi \lesssim 1 \text{ GeV}. \tag{2.19}$$

This partial-wave unitarity bound is independent of the details of the dark sector. In specific models of dark sector self-interactions, other considerations, such as perturbativity of couplings, may impose stronger bounds. For example, in simple scalar models discussed in Section 2.4, the upper bound on the ELDER mass from perturbativity is about 200 MeV.

There is also a lower bound on m_χ. As the ELDER becomes non-relativistic, energy and entropy are transferred from the dark sector to the SM, reheating the SM degrees of freedom. This process continues until the decoupling of elastic scattering between ELDERs and the SM at temperature T_d. If the energy and entropy transfer is active during or after Big-Bang Nucleosynthesis (BBN), it will generally result in modification of BBN predictions for light-element abundances, and/or the effective number of neutrinos N_{eff} inferred from the Cosmic Microwave Background (CMB) measurements; see *e.g.* Ref. [90]. This is certainly the case if the interactions between the ELDER and the SM are mediated via the dark photon portal, which, as argued in Section 2.3, is the most plausible renormalizable portal compatible with this scenario. The dark photon portal couples the ELDERs very weakly to neutrinos. If entropy transfer continues below the temperature of neutrino decoupling from the electron/photon plasma, non-standard N_{eff} is produced. It is in principle possible that this bound could be avoided in a model in which electrons, photons and neutrinos are reheated equally. However in this thesis we

will adopt [90]

$$m_\chi \gtrsim 5 \text{ MeV} \tag{2.20}$$

as a rough lower bound on the ELDER mass.

2.2.3 ELDERs, SIMPs and WIMPs, Oh My!

If in a given model $c_n < \bar{c}_n$, defined in (2.3) and (2.13), the particle χ cannot account for the observed dark matter. On the other hand, if $c_n > \bar{c}_n$, the correct relic density can still be achieved through the SIMP mechanism. In this case, dark matter and SM remain in kinetic equilibrium until the $3 \to 2$ interactions decouple and the χ density freezes out: $x_d > x_f$. The relic density is given by

$$\Omega_\chi h^2 \simeq 0.02 \left(\frac{m_\chi}{10 \text{ MeV}}\right)^{3/2} \alpha^{-3/2} \left(\frac{x_f}{20}\right)^2, \tag{2.21}$$

where the freeze-out temperature x_f is found as a solution to

$$x_f + \frac{1}{2}\log x_f = 20.7 - \frac{1}{2}\log\left(\frac{m_\chi}{10 \text{ MeV}}\right) + \frac{3}{2}\log\alpha + \log g_\chi. \tag{2.22}$$

After freeze-out, elastic scattering with SM no longer affects n_χ; thus in the SIMP regime, the relic density is determined by the self-interaction strength α, and is independent of c_n. The SIMP value of α,

$$\alpha_{\text{SIMP}} \simeq 0.34 \left(\frac{m_\chi}{10 \text{ MeV}}\right) \left(\frac{\Omega_\chi h^2}{0.1}\right), \tag{2.23}$$

is close to the lower bound on α required for the ELDER scenario, Eq. (2.14), and scales the same way with m_χ. This gives a clear intuitive picture of the relation between the two regimes: for a given dark matter particle mass, the ELDER value of c_n gives the lower bound on c_n for SIMPs, while α_{SIMP} is the lower bound of α for ELDERs.

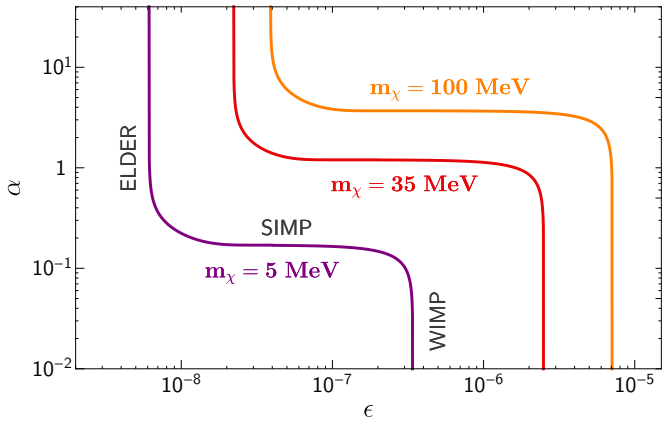

Figure 2.2: Regions of parameters corresponding to the observed relic density. For each mass, the vertical section of the line of the left/top corresponds to the elastically decoupling relic (ELDER) scenario proposed in this thesis; the horizontal line to the SIMP scenario; and the vertical section on the right/bottom to the WIMP scenario. This figure, reproduced from Ref. [1], is based on a numerical solution of the Boltzmann equations for a model with $g_\chi = 2$, $\psi =$ photon, $n = 0$, $c_0 = 8\pi\epsilon^2$. The same behavior is observed in other models, see for example Fig. 2.6 below.

If c_n is increased even further, eventually a point is reached where annihilations to SM decouple after the $3 \to 2$ interactions. At this point, the relic density is determined by the cross section of annihilations to SM, and is once again independent of α. Since this is the mechanism that sets the relic abundance of the conventional WIMPs, we refer to it as the "WIMP regime", even though the dark matter particle mass is still well below the weak scale, and a small coupling to SM is required to obtain the correct relic density. (For theoretically motivated realizations of such a scenario, see [91].) Figure 2.2 illustrates the three regimes. This figure, reproduced from Ref. [1], is based on a numerical solution of the Boltzmann equations for a model with $g_\chi = 2$, $\psi =$ photon, $n = 0$, $c_0 = 8\pi\epsilon^2$, which was performed in that thesis. The same behavior is observed in other models, see for example Fig. 2.6 below.

2.3 Dark Photon Portal and Phenomenology

It is well known that there are only three renormalizable interactions that can couple SM to dark sector states: “dark photon", “Higgs", and “right-handed neutrino" portals [52]. Of these, only the dark photon portal is compatible with the ELDER scenario in its simplest form. In the case of the Higgs portal, the interaction has the form S^2H^2, where S is a dark-sector field and H is the SM Higgs. In the case of ELDER, the decoupling temperature is at the MeV scale, and the relevant SM degrees of freedom are electrons, photons, and neutrinos. The couplings to these particles at MeV temperatures mediated by the Higgs are too weak to produce the elastic scattering of the strength required in the ELDER scenario. In the case of the neutrino portal, the interaction is of the form HLN, where N is a dark-sector fermion. The ELDER dark matter particle must possess $3 \to 2$ interactions, and thus must be a boson. If the dark matter is a fermion, then cannibalization may occur via $4 \to 2$ annihilations. However, this leads to strongly self-interacting sub-MeV DM, which is excluded by BBN and structure formation [83]. Hence, we will focus on the dark photon portal as the most plausible mechanism for ELDER-SM coupling.

2.3.1 Dark Photon Portal

Specifically, we consider a complex scalar field χ, neutral under SM gauge symmetries but charged under an abelian $U(1)_D$ gauge group in the dark sector:

$$\mathcal{L} = |D_\mu \chi|^2 = \partial^\mu \chi \partial_\mu \chi^* + i g_D A'_\mu \left(\chi^* \partial_\mu \chi - \chi \partial_\mu \chi^*\right) + \dots \tag{2.24}$$

where g_D is the $U(1)_D$ coupling constant, and A' is the corresponding gauge field. The A' kinetically mixes with the SM photon:[4]

$$\mathcal{L}_{\rm k-m} = \frac{1}{2}\frac{\epsilon_\gamma}{\cos\theta_W} B^{\mu\nu} F_{D\mu\nu}, \tag{2.25}$$

where B and F_D are the field strength tensors of the $U(1)_Y$ and $U(1)_D$, and θ_W is the Weinberg angle. Diagonalizing the kinetic terms yields the SM photon A, under which χ is uncharged, and the "dark photon" V, which couples to the SM electromagnetic current with strength $\epsilon_\gamma e$, and to the "dark" $U(1)_D$ current with strength g_D. We further assume that $U(1)_D$ is broken, giving the dark photon mass m_V. (For specific models that realize this setup, including ELDER self-interactions, see Section 2.4.) If dark photons have a significant abundance in the early universe at the time of ELDER decoupling and freeze-out, the physics of these processes becomes considerably more complicated: for example, co-annihilation processes may play an important role in transferring energy between the SM and the dark sector. To avoid these complications, we focus our attention on the "pure ELDER" case, when the dark photon is significantly heavier than the dark matter particle. For concreteness, we assume $m_V > 2m_\chi$.

Elastic scattering of ELDER on electrons is mediated by the t-channel dark photon exchange. In the language of Section 2.2, the dark photon portal model corresponds to $\psi = e^\pm$, $g_\psi = 4$, $n = 2$, and the elastic scattering strength is given

[4] In the fundamental theory, the mixing involves the SM hypercharge gauge field. Since the physics considered here takes place well below the weak scale, we ignore the mixing with the Z boson.

by[5]

$$c_2 = \frac{2e^2\epsilon_\gamma^2 g_D^2 m_\chi^4}{m_V^4} \simeq 2.3y. \tag{2.26}$$

Here we defined the dimensionless combination

$$y = \epsilon_\gamma^2 \alpha_D \left(\frac{m_\chi}{m_V}\right)^4, \tag{2.27}$$

where $\alpha_D = g_D^2/(4\pi)$. This is the same combination of parameters that controls dark matter annihilations to the SM, as has been previously noticed in studies of the conventional scenario where such annihilations determine the relic density [92]. In the ELDER scenario, the value of y that corresponds to the observed relic density can be inferred from Eq. (2.13):

$$y_{\rm ELDER} \simeq 5.8 \times 10^{-15} \left(\frac{g_{*,d}}{10}\right)^{1/2} \left(\frac{m_\chi}{10\ {\rm MeV}}\right) \left(\frac{x_d}{17}\right)^6, \tag{2.28}$$

where x_d is the solution to Eq. (2.12). This is a robust prediction of the ELDER scenario with the dark photon portal, independent of the details of ELDER self-interaction dynamics.

As discussed above, if the dark matter coupling to the SM is increased above the ELDER value, correct relic density can still be achieved by SIMP or WIMP mechanisms. In the dark photon portal model, the WIMP regime corresponds to the well-known "thermal target" value for y [92]:

$$\frac{y_{\rm WIMP}}{\xi^2} \simeq 1.4 \times 10^{-11} \left(\frac{\Omega_\chi h^2}{0.1}\right)^{-1} \left(\frac{m_\chi}{10\ {\rm MeV}}\right)^2 \left(\frac{x_{f,a}}{20}\right)^2, \tag{2.29}$$

where $\xi = 1 - 4m_\chi^2/m_V^2$, and $x_{f,a}$ is the temperature at which annihilations to SM freeze out. Any value of y between $y_{\rm ELDER}$ and the thermal target is compatible with the SIMP mechanism, which can yield the correct relic density for appropriately chosen $3 \to 2$ self-scattering cross sections.

[5]Near the upper boundary of the ELDER mass region, $m_\chi \sim 1$ GeV, scattering off charged pions and muons is relevant during decoupling, and the formulas in this Section are modified by $\mathcal{O}(1)$ factors to include their contributions.

Before proceeding, let us briefly comment on the astrophysical constraints on this model. Dark matter pair annihilation into electrons is constrained by the CMB measurements [93–95], as well as indirect-detection searches. However, in the case of scalar dark matter in the relevant mass range, the s-wave annihilation cross section is suppressed by a factor of $(m_e/m_\chi)^2 \lesssim 10^{-2}$, while the p-wave contribution is velocity-suppressed. As a result, ELDER dark matter is easily consistent with these constraints. Also, the reaction $e^+e^- \to \chi\chi$ (with or without an on-shell dark photon) can provide an additional mechanism of cooling in supernovae, which is constrained by the observation of neutrinos from SN1987A (see *e.g.* [96, 97]). We checked that in the ELDER region, the elastic scattering of χ on electrons is always sufficiently strong to prevent the dark matter particles from leaving the supernova core. The produced χ's become trapped in the core, and do not contribute to the cooling rate.

2.3.2 Direct Detection

Direct detection of sub-GeV dark matter has been an area of active recent investigations. Heavy nuclear recoils do not carry sufficient energy to be detected in this mass range, and direct detection is easier for dark matter scattering on electrons. Remarkably, in the ELDER scenario with a dark photon portal, it is *precisely the same process* that determines the DM relic density. The observed dark matter density completely determines the direct detection cross section, with essentially no free parameters other than the ELDER mass m_χ. The direct detection cross section is given by

$$\sigma_e^{\rm DD} = \frac{16\pi\alpha m_e^2}{m_\chi^4}\, y. \tag{2.30}$$

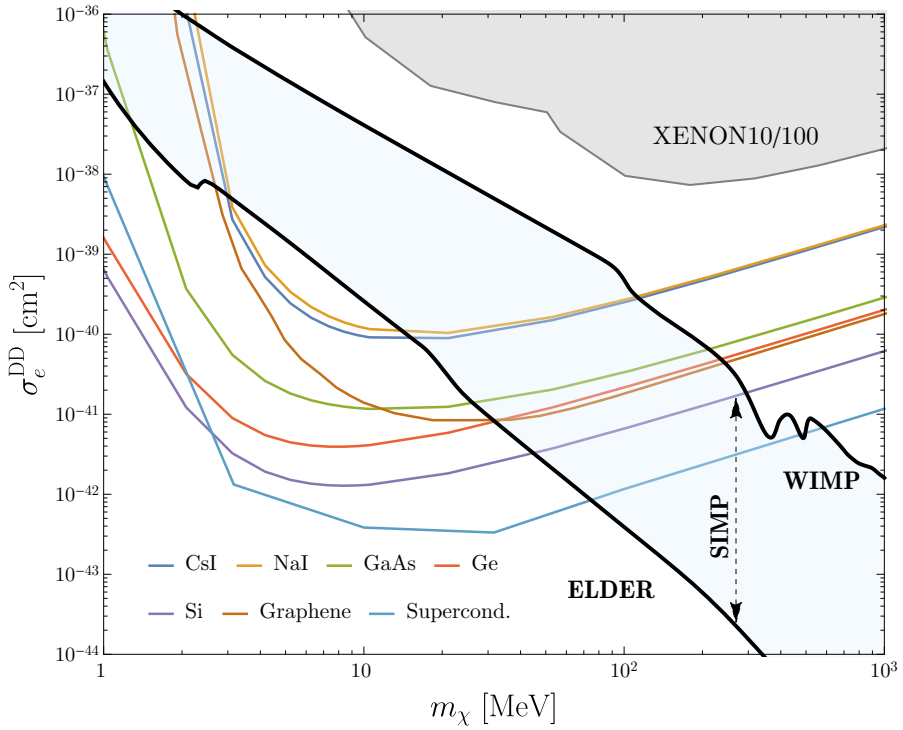

Figure 2.3: Direct detection cross section, $\sigma_e^{\rm DD}$, predicted in the ELDER, WIMP and SIMP scenarios with a dark photon portal. For comparison, also shown are the current bounds from XENON experiment [98, 99] and projected sensitivities for 3 events in 1 kg-year exposure of proposed experiments: semiconductors [100–103], superconductors (10 meV threshold) [26, 104], superfluids [105, 106], scintillators [100, 107] and graphene [108].

Setting $y = y_{\rm ELDER}$ in this formula defines a very sharp "ELDER target" for the direct detection experiments. This complements the "thermal target" [52, 92], which in our language corresponds to $y = y_{\rm WIMP}$, while the region $y_{\rm ELDER} < y < y_{\rm WIMP}$ corresponds to SIMP dark matter. Moreover, as discussed above, observational constraints and unitarity considerations restrict m_χ to a range between roughly 5 MeV and 1 GeV. These considerations define the *direct detection target region*, shown in Fig. 2.3.

The predicted cross sections are well below the current XENON bounds [98,99]. However, novel experimental approaches that are currently being investigated have

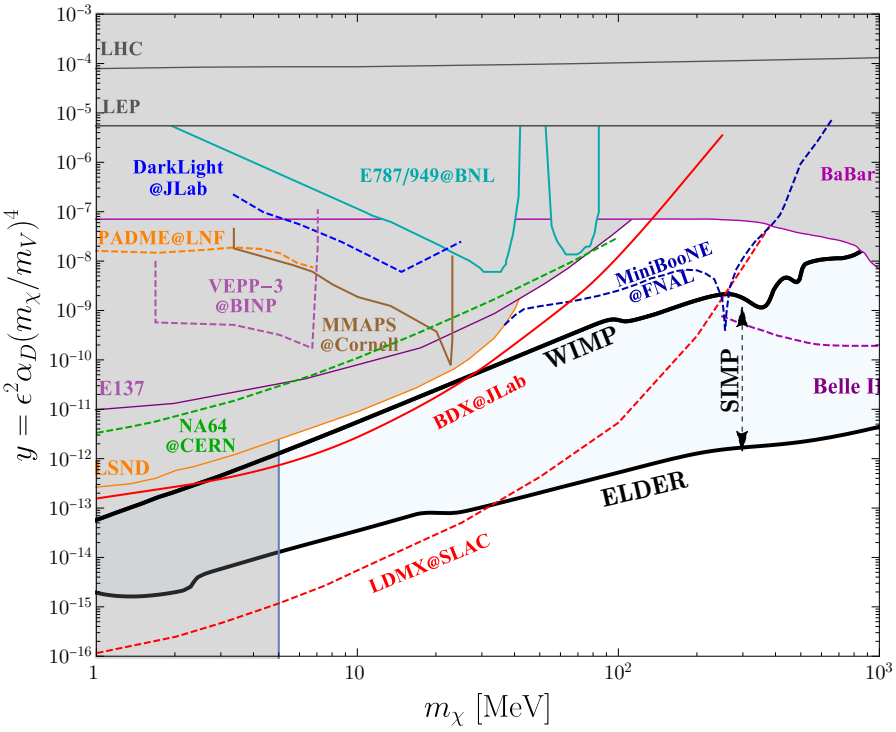

Figure 2.4: The dark photon target region predicted in the ELDER, WIMP and SIMP scenarios. For comparison, the current bounds and projected sensitivities of searches for dark photon decaying to dark matter particles [52] are also shown.

the potential to dramatically increase the sensitivity to DM-electron scattering in this mass range. Target materials under study include semiconductors [100–103], noble liquids [98, 100], superconductors [26, 104], superfluids [105, 106], scintillators [100, 107] and graphene [108]. Projected sensitivities of these experiments will allow them to test a significant part of the SIMP and ELDER target region, see Fig. 2.3.

2.3.3 Dark Photon Searches

Searches for a dark photon in the MeV-GeV range have also been an area of much activity recently. Existing experimental data has been used to place bounds on the

dark photon, and several dedicated experiments are now running or in preparation. The ELDER, SIMP and WIMP scenarios with dark photon portal provide a well-defined *dark photon target region* for such experiments, shown in Fig. 2.4.

In the ELDER scenario, the dark photon mass m_V must be large enough so that the process $\chi\chi^* \leftrightarrow VV$ is not relevant throughout the χ kinetic decoupling and freeze-out process. For the discussion of this section, we assume $m_V > 2m_\chi$. In this case, the decay $V \to \chi\chi^*$ is likely to be the dominant dark photon decay channel, since its amplitude is proportional to the dark sector gauge coupling g_D, which is naturally of order one, while the amplitudes of competing decays such as $V \to e^+e^-$ are controlled by the small kinetic mixing parameter ϵ_γ. As a result, the experiments relevant for constraining our scenario are those searching for *invisible* dark photon decays. There are two basic experimental approaches. First, one can search for missing mass or energy in collider events due to an invisible particle V. The strongest current constraints from this approach come from re-analysis of BaBar data [109], as well as, at low masses, the dedicated NA-64 experiment at CERN [110]. These searches do not yet constrain the ELDER scenario. In the future, the missing-energy LDMX experiment proposed at SLAC [92,111] will have sufficient sensitivity to test a significant part of the ELDER parameter space. Second, one can search for a dark matter particle that is produced in dark photon decay and propagates through shielding material to a downstream detector. (This would in effect amount to "direct detection" of a dark matter particle produced in an accelerator.) This approach was recently pioneered by the MiniBooNE experiment [112], and dedicated experiments such as BDX [113] and SHiP [114] have been proposed. Such future experiments may be sensitive to ELDER and SIMP dark matter. A snapshot of the current and expected sensitivities of a variety of dark photon searches, collected in Ref. [52], and overlaid with the ELDER and

SIMP regimes, is shown in Fig. 2.4.

We remind the reader that while the theoretical predictions of the dark photon target region are naturally defined in terms of the y variable, and are largely insensitive to variations of model parameters that leave y unchanged, the same is *not* true of experimental sensitivities, which depend on model parameters in different ways. For example, sensitivity of a missing-mass experiment such as BaBar is completely independent of g_D, as long as it's large enough so that the invisible branching ratio of V is close to 100%. Thus, additional assumptions have to be made in displaying experimental sensitivities in terms of y, as in Fig. 2.4; see Ref. [52] for further discussion.

2.4 Models of ELDERs

We argued above that strong self-interactions in the dark sector are required in the ELDER scenario, with $3 \to 2$ cross-section of order one in its natural units. At some level, this is welcome: Such strong self-interactions are indeed expected if the ELDER is a bound state of confining dynamics in the dark sector, a paradigm that can potentially provide a natural explanation of proximity of the ELDER mass to the QCD confinement scale. On the other hand, it does create obvious challenges for model-building. Moreover, strong number-changing self-interactions tend to be accompanied by a large ELDER elastic scattering cross section, which can run afoul of observational constraints on dark matter self-scattering in galactic clusters such as the Bullet cluster. Fortunately, many phenomenological predictions of the ELDER scenario are independent of the details of dark sector self-interactions. This allowed us to completely sidestep these questions in the discussion of Sec-

tion 2.3. We will now discuss two simple, renormalizable dark-sector models that explicitly realize the ELDER scenario. While not deeply rooted in strong gauge dynamics, they can be thought of as toy models representing interactions among the lightest mesons produced by such dynamics. They provide a useful illustration of the issues involved in dark-sector model building, and an "existence proof" demonstration that consistent models can be found.

2.4.1 χ^3 Model

Here we consider a simple model in which the dark matter is a complex scalar charged under an unbroken Z_3 symmetry [68, 83, 115]. Consider a dark sector consisting of a $U(1)_D$ gauge field with gauge coupling g_D, and two scalar fields charged under it, Φ and χ, with $Q(\Phi) = +3$ and $Q(\chi) = +1$. The χ particle will play the role of dark matter. The scalar potential is

$$V = V(\Phi) + V(\chi) + \frac{g}{3!}\left(\Phi^* \chi^3 + \Phi \chi^{*3}\right) + \lambda_{\Phi\chi} |\Phi|^2 |\chi|^2, \tag{2.31}$$

where $V(\psi) = m_\psi^2 |\psi|^2 + \lambda_\psi |\psi|^4$. We will assume $m_\Phi^2 < 0$, so that this field gets a vacuum expectation value (vev) $\langle \Phi \rangle = w/\sqrt{2}$. We further assume that m_χ^2 is positive. For simplicity, we consider the situation $m_\chi < |m_\Phi|$, with sufficient separation to ensure that the radial degree of freedom of Φ is sufficiently heavy to not play a role in the calculation of χ relic abundance. The effective Lagrangian for such calculation is then given by

$$V_{\text{eff}} = V(\chi) + \frac{R}{3!} m_\chi \left(\chi^3 + \chi^{*3}\right), \tag{2.32}$$

where we defined a dimensionless 3-point coupling

$$R = \frac{gw}{\sqrt{2} m_\chi}. \tag{2.33}$$

The only effect of the last term in the potential (2.31) is to renormalize the χ mass. The vev of Φ leaves a global Z_3 subgroup of the $U(1)_D$ unbroken, and the charge of χ under this discrete symmetry guarantees its stability, as required for a dark matter candidate. The $U(1)_D$ gauge boson gets a mass $m_V = \sqrt{3} g_D w$. The symmetry of the theory allows for kinetic mixing between the $U(1)_D$ gauge boson and the SM hypercharge gauge boson, as in Eq. (2.25). As long as there are states, at any mass scale, that are charged under both gauge groups, such kinetic mixing will be generated, with values of $\epsilon_\gamma \sim 10^{-4} - 10^{-2}$ being generic if no cancellations occur at the one-loop level [44]. Thus, this construction provides a stable scalar dark matter candidate with natural coupling to the electron via a dark photon portal.

The matrix elements for non-relativistic $3\chi \to 2\chi$ annihilations are given by

$$\mathcal{M}(\chi\chi\chi^* \to \chi^*\chi^*) = -i\frac{13}{24}\frac{R^3}{m_\chi}\,, \quad \mathcal{M}(\chi\chi\chi \to \chi\chi^*) = +i\frac{1}{2}\frac{R^3}{m_\chi}\,. \tag{2.34}$$

Here we set $\lambda_\chi = 0$ for simplicity. This point is unexceptional (there is no enhanced symmetry associated with vanishing of λ_χ) and is sufficient to illustrate the important physical features of the model. This yields the thermally averaged cross section

$$\langle \sigma v^2 \rangle = \frac{\sqrt{5}}{2304\pi}\frac{265}{768}\frac{R^6}{m_\chi^5} \simeq 10^{-4}\frac{R^6}{m_\chi^5}. \tag{2.35}$$

In the SIMP scenario, the coupling R can be inferred from the relic density as follows:

$$R_{\rm SIMP} \simeq 2.6 \left(\frac{m_\chi}{10\ {\rm MeV}}\right)^{1/2} \left(\frac{\Omega_\chi h^2}{0.1}\right)^{1/2}. \tag{2.36}$$

The required coupling is quite large, consistent with the idea that SIMP/ELDER dark matter particle can be a bound state of dark-sector confining gauge group: in this scenario, the potential (2.31) can be thought of as a toy model representing the interactions among the two lightest mesons. The range of validity of the

perturbative χ^3 model can be estimated as $R \lesssim 4\pi$. In the SIMP scenario, this gives an upper bound on the dark matter particle mass:

$$m_\chi \lesssim 230 \text{ MeV}. \tag{2.37}$$

As discussed in Section 2.2, the "pure ELDER" scenario requires larger $3 \to 2$ cross section than SIMP for the same m_χ, and therefore the upper bound on m_χ is somewhat lower for ELDERs.

The dark matter elastic self-scattering cross section is constrained by observations of galactic clusters, such as the Bullet cluster [15, 116, 117], and halo shapes [118–120]:

$$\frac{\bar{\sigma}_{2\to2}}{m_\chi} \leq 0.47 \text{ cm}^2/\text{g}, \tag{2.38}$$

where $\bar{\sigma}_{2\to2} \equiv (\sigma(\chi\chi \to \chi\chi) + \sigma(\chi\chi^* \to \chi\chi^*))/2$. The χ^3 model in the SIMP scenario predicts

$$\frac{\bar{\sigma}_{\text{SIMP}}}{m_\chi} \simeq \left(\frac{m_\chi}{10 \text{ MeV}}\right)^{-1} \cdot \left(30 \frac{\text{cm}^2}{\text{g}}\right), \tag{2.39}$$

while in the ELDER scenario the cross-section is even larger (bounded from below by Eq. (2.39)). Thus, the simplest single-field χ^3 model cannot provide sufficiently strong self-interactions required in these scenarios, while being consistent with observational constraints. We will now show that adding another dark-sector scalar field can resolve this problem.

2.4.2 Choi-Lee Model

This model was originally introduced by Choi and Lee (CL) [73] in the context of the SIMP scenario. The dark sector contains a $U(1)_D$ gauge symmetry, with gauge coupling g_D, and three complex scalar fields charged under this symmetry:

ϕ, S, and χ, with charges $q_\phi = +5$, $q_S = +3$, and $q_\chi = +1$. The most general renormalizable scalar potential consistent with these charge assignments is

$$\begin{aligned} V_{\rm d} &= m_\phi^2|\Phi|^2 + \lambda_\phi|\Phi|^4 + m_S^2|S|^2 + \lambda_S|S|^4 + m_\chi^2|\chi|^2 + \lambda_\chi|\chi|^4 \\ &\quad +\lambda_{\phi S}|\Phi|^2|S|^2 + \lambda_{\phi\chi}|\Phi|^2|\chi|^2 + \lambda_{S\chi}|S|^2|\chi|^2 + \\ &\quad +\frac{1}{\sqrt{2}}\lambda_1\Phi^\dagger S^2\chi^\dagger + \frac{1}{\sqrt{2}}\lambda_2\Phi^\dagger S\chi^2 + \frac{1}{6}\lambda_3 S^\dagger\chi^3 + \text{h.c.} \end{aligned} \tag{2.40}$$

We assume that $m_\phi^2 < 0$, while the other two scalar fields have positive mass-squared. The vev $\langle\Phi\rangle = w/\sqrt{2}$ breaks the gauge symmetry, giving the $U(1)_D$ gauge boson a mass $m_V = \sqrt{5}g_D w$. The Φ vev preserves a discrete Z_5 subgroup of the $U(1)_D$, under which S and χ are both charged. The lighter of these particles, which we will assume to be the χ, is therefore stable, and can play the role of dark matter. The scalar interactions after spontaneous symmetry breaking are described by

$$\begin{aligned} V_{\rm d} &= \frac{m_\chi}{\sqrt{2}}R_1 S^2\chi^\dagger + \frac{m_\chi}{\sqrt{2}}R_2 S\chi^2 + \frac{1}{6}\lambda_3 S^\dagger\chi^3 + \text{h.c.} \\ &\quad +\lambda_S|S|^4 + \lambda_\chi|\chi|^4 + \lambda_{S\chi}|S|^2|\chi|^2, \end{aligned} \tag{2.41}$$

where we have omitted interactions with the Higgs component of Φ which play no role in the phenomenology considered here, and defined dimensionless couplings

$$R_i = \frac{v_D\lambda_i}{\sqrt{2}m_\chi}, \quad i = 1, 2. \tag{2.42}$$

As in the χ^3 model, the dark gauge boson V kinetically mixes with the SM photon, providing a dark photon coupling between the dark sector and the SM.

The $2\chi \leftrightarrow 3\chi$ scattering process is induced by the couplings in the first line of Eq. (2.41). For simplicity, we set $\lambda_3 = 0$; this point is unexceptional (there is no enhanced symmetry associated with vanishing of λ_3) and is sufficient to illustrate the features of interest to us. The key observation is that for $m_S \approx 3m_\chi$,

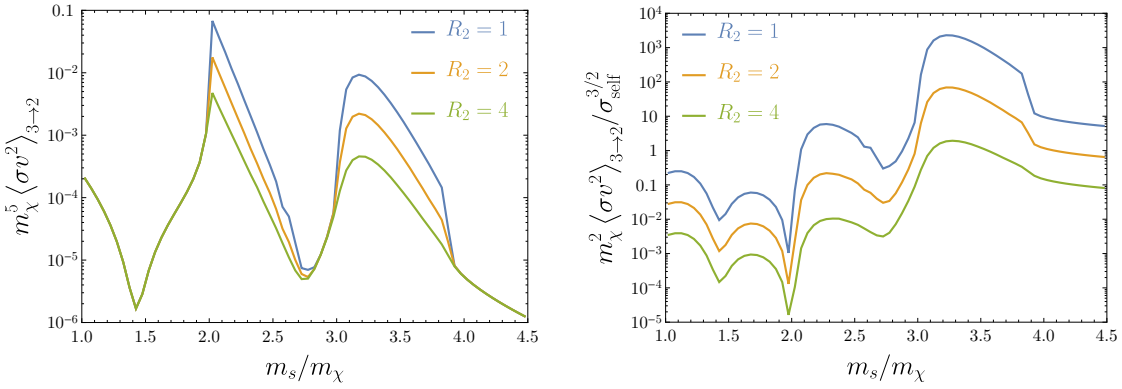

Figure 2.5: The cross section $\langle \sigma_{3\to 2} v^2 \rangle$ (left) and the dimensionless ratio of number-changing and elastic self-scattering rates (right), as a function of m_S/m_χ.

the $2\chi \leftrightarrow 3\chi$ scattering is resonantly enhanced, while the $2\chi \leftrightarrow 2\chi$ process is not. This effect is illustrated by the left panel of Fig. 2.5, where we plot the thermally-averaged $\langle \sigma_{3\to 2} v^2 \rangle$ at temperature close to ELDER kinetic decoupling. A dimensionless ratio of the number-changing and number-preserving cross sections, $m_\chi^2 \langle \sigma_{3\to 2} v^2 \rangle / \sigma_{2\to 2}^{3/2}$, can reach $\mathcal{O}(10^3)$. For comparison, in the χ^3 model studied in the previous section, this ratio is close to 1. Note that the values of couplings R_i required in the SIMP/ELDER scenarios are fairly large, so that the S resonance is rather broad and no significant fine-tuning of m_S/m_χ is required to achieve significant enhancement of the $3 \to 2$ rate. This enhancement makes it possible to successfully implement SIMP and ELDER dark matter in the CL model without conflict with observational constraints from galaxy clusters and halo shapes.

Because of the resonance at $\sqrt{s} \approx 3m_\chi$, the quantity $\langle \sigma_{3\to 2} v^2 \rangle$ has a non-trivial temperature dependence in the non-relativistic regime, making the parametrization of Eq. (2.10) inapplicable. To compute the relic density, we integrate the Boltzmann equations numerically. The relic density is controlled by the seven model parameters that enter the Boltzmann equations: particle masses m_χ, m_S, and m_V; and dimensionless coupling constants R_1, R_2, g_D, and ϵ_γ. To perform

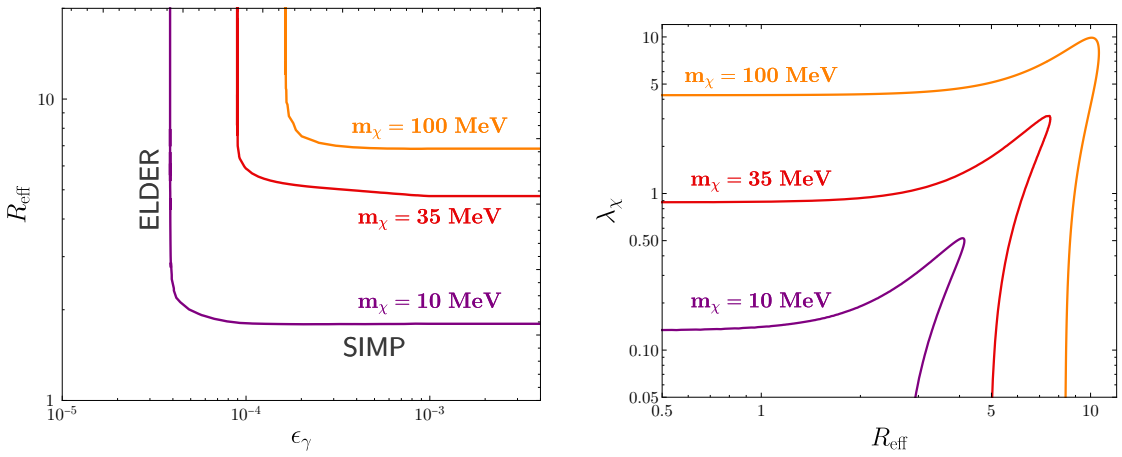

Figure 2.6: Left: Regions of CL model parameter space with χ relic density consistent with the current best-fit ΛCDM value. Right: Constraints from galaxy cluster observations (the regions below the curves are allowed). In both plots, $m_S/m_\chi = 3.1$, $m_V/m_\chi = 10$, and $g_D = 1$. In the right panel, we fix $R_1 = 10$ for illustration.

numerical analysis in this large parameter space, we made the following choices:

- The ratio of S and χ masses was fixed close to the $3 \to 2$ resonance, $m_S/m_\chi = 3.1$.
- As discussed in Section 2.3, the relic density depends on the three parameters of the dark photon portal only through a single dimensionless combination y, defined in Eq. (2.27). Therefore it is sufficient to fix two of these parameters, and vary the third one. We fix $m_V/m_\chi = 10$ and $g_D = 1$, and vary ϵ_γ.
- The $3 \to 2$ matrix element is proportional to a product $R_1 R_2^2$, so that the DM relic density primarily depends on these couplings through the "effective" $3 \to 2$ coupling,

$$R_{\rm eff} \equiv \left(R_1 R_2^2\right)^{1/3}. \tag{2.43}$$

The relic density also depends on the width Γ_S, which is proportional to R_2^2. In practice, in the numerical analysis we fix R_2 (specifically, $R_2 = 2$ for

$m_\chi = 10$ MeV and $R_2 = 4$ for $m_\chi = 35, 100$ MeV) and vary R_1. However, we checked that in the parameter range of interest, the relic density is insensitive to variations of R_2 within broad ranges around these values, allowing us to present the results solely in terms of the effective coupling $R_{\rm eff}$.

The three remaining parameters $(m_\chi, R_{\rm eff}, \epsilon_\gamma)$, are scanned over. The results are illustrated in the left panel of Fig. 2.6, which shows regions of parameter space consistent with the current best-fit ΛCDM dark matter density, $\Omega_\chi h^2 = 0.1188 \pm 0.0010$ [121], in the $\epsilon_\gamma - R_{\rm eff}$ plane for three values of DM mass, 10, 35 and 100 MeV. The (roughly) horizontal bands of viable parameter space correspond to the SIMP scenario, while the (roughly) vertical bands realize the ELDER scenario. The values of ϵ_γ for the ELDER regime are in excellent agreement with the results of the analytic approach, Eq. (2.28). In the intermediate regime, the DM-SM elastic scattering and the DM number-changing self-scattering decouple at roughly the same time, and both processes play a role in determining the relic density.

As expected, realizing ELDER (or SIMP) dark matter in the CL model requires $\mathcal{O}(1)$ couplings among the scalars of the dark sector. The range of validity of perturbative CL model can be estimated as $R_1 \lesssim 4\pi$, $R_2 \lesssim 4\pi$. Combined with the relic density calculation, these constraints place an upper bound on the ELDER dark matter mass, $m_\chi \lesssim 200$ MeV. Furthermore, the χ self-scattering cross section is constrained by observations of galactic clusters and halo shapes, Eq. (2.38). The self-scattering cross section receives contributions from a quartic coupling λ_χ as well as the S-exchange diagram controlled by R_2, and partial cancellation of the two diagrams is possible. Combined with the perturbativity bound on R_1, cluster observations place an upper bound on $R_{\rm eff}$, shown in Fig. 2.6. For $m_\chi > 5$ MeV, the values of $R_{\rm eff}$ required in the ELDER scenario are compatible with observations.

2.5 Conclusions

In this chapter, we studied the Elastically Decoupling Relic (ELDER) scenario for thermal dark matter. We presented an approximate analytic solution for the evolution of ELDER temperature throughout the kinetic decoupling epoch. This solution was used to provide explicit formulas relating various relevant quantities, such as, for example, the relic density of ELDERs and the cross section of their elastic scattering off SM particles. We also applied partial-wave unitarity constraint to obtain a bound on the allowed mass range for the ELDER dark matter candidate, 5 MeV $\lesssim m_\chi \lesssim$ 1 GeV. These results are valid in a broadly model-independent framework.

Further, we showed that a dark photon portal can naturally provide the coupling between the dark matter particles and SM of the strength required in the ELDER scenario. Within the dark photon model, the ELDER scenario provides unambiguous predictions for dark matter direct detection experiments and dark photon searches, shown in Figs. 2.3 and 2.4. These predictions have no free parameters other than the dark matter mass. They are also independent of the details of dark sector, as long as it provides sufficiently strong number-changing self-interactions to realize the ELDER scenario. Together with the well-known "thermal target" and predictions of the Strongly-Interacting Massive Particle (SIMP) scenario, the ELDER predictions delineate a well-defined target region in the parameter spaces relevant for direct-detection and dark photon searches, which will be explored by the next generation of experiments.

Both the ELDER and SIMP scenarios require $\mathcal{O}(1)$ strength (in natural units) of self-interactions among dark matter particles. Here, we studied two simple scalar-field models that incorporate such interactions while remaining within per-

turbative regime, for $m_\chi \lesssim 200$ MeV. The models also naturally contain coupling to the SM via the dark photon portal. The simplest model, with just two scalar fields, exhibits tension with bounds on dark matter self-scattering cross section from observations of galaxy clusters. However, a slightly more complex model, with three scalar fields and a resonance structure, easily evades such bounds. These results indicate that there is no fundamental obstruction to finding dark sectors compatible with ELDER and/or SIMP scenarios.

An important motivation for SIMP and ELDER scenarios is the proximity of the predicted dark matter particle mass to $\Lambda_{\rm QCD}$, a well-established important scale in the SM. In the toy models studied in this thesis, $m_\chi \sim \Lambda_{\rm QCD}$ is put in by hand. The natural next step in the model-building direction would be to construct models in which this relation, as well as the strong self interactions, emerge naturally from UV physics.

CHAPTER 3

NEW ASTROPHYSICAL SEARCHES FOR DARK MATTER

3.1 Introduction

Dark matter (DM) that implodes neutron stars (NSs) may explain the paucity of pulsars in the Milky Way galactic center, the source of r-process elements, and the origin of fast-radio bursts. In this chapter, we identify new astrophysical signatures of NS-imploding DM, which could decisively test these hypotheses in the next few years. First, NS-imploding DM forms $\ll 10^{-10}$ solar mass black holes inside NSs, thereby converting NSs into $\sim$1.5 solar mass BHs. This decreases the number of NS mergers seen by LIGO/VIRGO (LV) and associated merger kilonovae seen by telescopes like DES, BlackGEM, and ZTF, instead producing a population of "black mergers" containing $\sim$1.5 solar mass black holes. Second, DM-induced NS implosions create a new kind of kilonovae that lacks a detectable, accompanying gravitational signal. Using DES data and the Milky Way's r-process abundance, we set bounds on these DM-initiated "quiet-kilonovae." Third, the spatial distribution of merger kilonovae, quiet kilonovae, and fast radio bursts in galaxies can be used to detect dark matter. NS-imploding DM destroys most NSs at the centers of mature disc galaxies, so that NS merger kilonovae would appear mostly in a donut at large radii. We find that as few as ten NS merger kilonova events, located to $\sim$1 kpc precision could validate or exclude DM-induced NS implosions at 2σ confidence, exploring DM-nucleon cross-sections over an order of magnitude below current limits. Similarly, NS-imploding dark matter as the source of fast radio bursts can be tested at 2σ confidence once 20 bursts are located in host galaxies by radio arrays like CHIME and HIRAX.

3.2 Dark matter-induced neutron star implosions

Once enough dark matter has accumulated in a neutron star's interior, dark matter may collapse into a small ($\lesssim 10^{-10}$ $M_\odot$) black hole that subsequently consumes the neutron star [27, 29, 32]. We begin by defining a useful variable combination, the "normalized implosion time," which relates dark matter-induced NS implosions occurring at different radii from a galactic center, where the local dark matter density ρ_x and velocity dispersion v_x will be different, see Figure 3.1. The maximum mass accumulation rate of dark matter into a NS is [122]

$$\begin{aligned}\dot{m}_x &= \pi \rho_x \frac{2GMR}{v_x}\left(1-\frac{2GM}{R}\right)^{-1} \\ &\simeq \frac{10^{26}\ \mathrm{GeV}}{\mathrm{s}}\left(\frac{\rho_x}{\mathrm{GeV/cm^3}}\right)\left(\frac{200\ \mathrm{km/s}}{v_x}\right),\end{aligned} \tag{3.1}$$

where M and R are the mass and radius of the neutron star and G is Newton's constant. The time until NS implosion scales inversely with the mass accumulation rate, $t_c \propto \dot{m}_x^{-1}$; therefore t_c is proportional to the dark matter velocity dispersion divided by density, $t_c \propto v_x/\rho_x$. Furthermore, v_x and ρ_x are the only quantities in $\dot{m}_x$ that depend on the galactocentric radius r. It follows that for dark matter which implodes NSs in time t_c, the quantity

$$t_c \frac{\rho_x}{v_x} = \text{ Constant} \times \left[\mathrm{Gyr}\ \frac{\mathrm{GeV/cm^3}}{200\ \mathrm{km/s}}\right], \tag{3.2}$$

which we call the normalized implosion time,[1] is independent of r. Throughout we will normalize $t_c\rho_x/v_x$ to a typical dark matter density (GeV/cm^3) and velocity dispersion (200 km/s) for a disc galaxy.

The value of $t_c\rho_x/v_x$ for a specific dark matter model can be determined by

[1] The units given in square brackets in Eq.(3.2) might be read as "A neutron star will implode in one gigayear for local dark matter density GeV/cm^3 and dark matter velocity dispersion 200 km/s."

calculating the time for dark matter with local density $\rho_{\rm x}$ and relative velocity $v_{\rm x}$ to implode a neutron star. While many asymmetric dark matter models implode neutron stars [27,28,28–32,123–128], we will focus on heavy $m_{\rm x} \gtrsim$ PeV asymmetric dark matter as a simple example. In the case of heavy asymmetric dark matter, the critical mass of dark matter required to form a small black hole is $M^{\rm f}_{\rm crit} \sim \frac{m^3_{\rm pl}}{m^2_{\rm x}}$ for dark fermions with mass $m_{\rm x}$ [128], and $M^{\rm b}_{\rm crit} \sim 0.12\sqrt{\lambda}\frac{m^3_{\rm pl}}{m^2_{\rm x}}$ for dark scalars with self-interaction potential $V(\phi) = \lambda|\phi|^4$ [129]. In these models, the neutron star will implode shortly after it collects a critical mass of dark matter at time $t_{\rm c} \simeq M_{\rm crit}/\dot{m}_{\rm x}$, where this expression assumes all dark matter passing through the neutron star is captured – see Appendix B.2 for details and for the scaling of dark matter-nucleon cross-section with $t_{\rm c}\rho_{\rm x}/v_{\rm x}$. Then the value of the galactic radial invariant $t_{\rm c}\rho_{\rm x}/v_{\rm x}$ is

$$
\begin{aligned}
t_{\rm c}\frac{\rho_{\rm x}}{v_{\rm x}}\Big|_{\rm f} &= \left(\frac{10\ {\rm PeV}}{m_{\rm x}}\right)^2\ 15\ {\rm Gyr}\ \frac{{\rm GeV/cm^3}}{200\ {\rm km/s}} \\
t_{\rm c}\frac{\rho_{\rm x}}{v_{\rm x}}\Big|_{\rm b} &= \left(\frac{\lambda}{1}\right)^{1/2}\left(\frac{3\ {\rm PeV}}{m_{\rm x}}\right)^2\ 20\ {\rm Gyr}\ \frac{{\rm GeV/cm^3}}{200\ {\rm km/s}},
\end{aligned}
\tag{3.3}
$$

for heavy asymmetric fermions and bosons, respectively.

3.3 Black mergers, quiet kilonovae, and r-process donuts

NS-imploding dark matter creates an unexpected population of low mass $\sim 1.5\ {\rm M}_\odot$ black holes (BHs), depleting the expected population of NSs. This in turn would alter the number of merging neutron stars that would be seen by LIGO/Virgo, along with their accompanying merger kilonovae, which are the days-long luminous outbursts from beta decaying neutrons ejected when NSs fall into a BH or another NS.

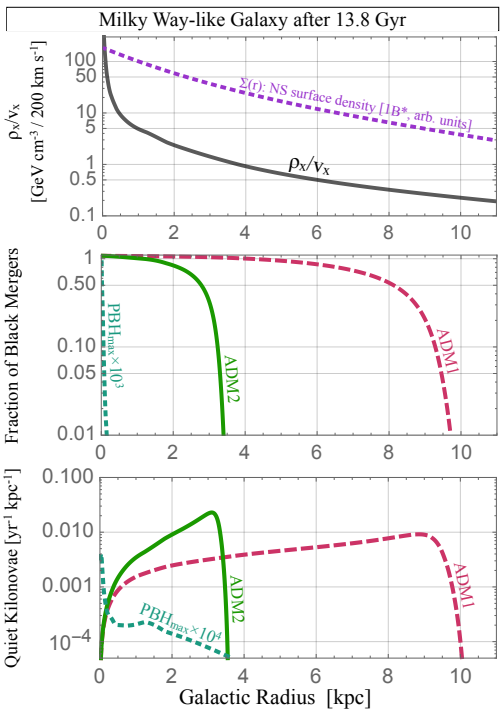

Figure 3.1: The dark matter density over velocity $\rho_{\rm x}/v_{\rm x}$ and NS surface density Σ in an MWEG (top), the total fraction of imploded neutron stars (middle), and the rate for quiet kilonovae, aka dark matter-induced NS implosions, per yr per kpc (bottom), are given as a function of distance from the center of a Milky Way-like galaxy for two asymmetric dark matter models ADM1 and ADM2, defined by $t_{\rm c}\rho_{\rm x}/v_{\rm x} = 3$ and 15 Gyr GeV/cm^3 (200 km/s)$^{-1}$. PBH$_{\rm max}$ is a maximally NS-imploding model described in Appendix B.2. For visibility, the PBH curve has been augmented by 3 and 4 orders of magnitude.

We now determine the number and position of neutron stars converted to BHs by dark matter in a Milky Way-like galaxy. With some subtleties that we will address, our findings for a typical 13 Gyr old $\sim 10^{12}$ M$_\odot$ disc galaxy can be applied to events in different galaxies, using a Milky Way equivalent galaxy (MWEG) volumetric conversion for merger and kilonova rates, *i.e.* one MWEG per (4.4 Mpc)^3 [130].

The number of neutron stars converted into BHs by dark matter in an MWEG will depend on the historic neutron star formation rate in the galaxy, the dynamics and final positions of neutron stars after formation, the dark matter halo density

profile, and the relative velocity of dark matter with respect to neutron stars. We model the historic star formation rate $\dot{M}^*(t)$ using a global fit to astronomical data ([131], Table 1, Column 2). While we use $\dot{M}^*(t)$ to determine the relative historic rate of neutron star formation, we normalize the total rate to 10^9 neutron star births over the MWEG lifetime.

To model dark matter in an MWEG, we use an NFW dark matter halo density profile [132], $\rho_{\rm x}(r) = \rho_0 (r/R_{\rm s})^{-1}(1 + r/R_{\rm s})^{-2}$, with dark matter density normalization $\rho_0 = 0.3$ GeV/cm^3 and scale factor $R_{\rm s} = 20$ kpc. To approximate the dark matter velocity dispersion in an MWEG, we match the phenomenological fit of Sofue to stellar velocities in the Milky Way ([133], Figure 11). With the star formation rate, neutron star distribution and dark matter properties specified, the fraction of neutron stars at radius r converted to solar mass BHs is given by $F_{\rm BH}(r) = \frac{\int_0^{{\rm Max}[t_{\rm u} - t_{\rm c}(r), 0]} \dot{M}^*(t)\ dt}{\int_0^{t_{\rm u}} \dot{M}^*(t)\ dt}$, where $t_{\rm u} \sim 13.8$ Gyr is the lifetime of the universe and $t_{\rm c}(r)$ is the collapse time at radius r, obtainable from Eq. (3.3). Similarly, the rate of neutron star implosions (and also quiet kilonovae) per unit galactocentric radius is given by $R_{\rm qk} = 2\pi r \Sigma(r) \dot{M}^*(t_{\rm u} - t_{\rm c}(r))$. In Figure 3.1, we plot the fraction of neutron stars converted to BHs along with the rate of neutron star implosions per year per kpc, both as a function of galactocentric radius, for a 13 Gyr old MWEG. In Table 3.1, we show how standard rates for compact object mergers would be altered, and display dark matter-induced neutron star implosion rates, for a few values of $t_{\rm c}\rho_{\rm x}/v_{\rm x}$. Table 3.1 also gives the maximum rate for PBH implosion of NSs, which we address in the next section.

Model	NS-NS	NS-BH	BH-BH	LM-BH	NS Im.	Im./$t_{\rm u}$
Non-Imp.	1e-4	3e-6	4e-7	0	0	0
ADM1	3e-5	9e-7	4e-7	7e-5	4e-2	7e8
ADM2	7e-5	2e-6	4e-7	3e-5	3e-2	3e8
$\rm PBH_{max}$	1e-4	3e-6	4e-7	4e-11	1e-7	400

Table 3.1: The first five columns give the rate for compact object mergers and dark matter-induced neutron star implosions per MWEG per year ($AeB \equiv A \times 10^B$), for both "Non-Implosive" and NS-imploding dark matter. ADM1 and ADM2 are defined by $t_{\rm c}\rho_{\rm x}/v_{\rm x} = 3$ and 15 Gyr GeV/cm^3 (200 km/s)$^{-1}$ respectively, and $\rm PBH_{max}$ is a maximally NS-imploding primordial BH model defined in Section 3.4. NS-NS, NS-BH, and BH-BH indicate standard NS and BH mergers, while LM-BH indicates a BH-BH merger with at least one $\sim 1.5\ M_\odot$ BH (Black Merger). We use the average BH and NS merger rates predicted in [130]; actual merger rates may be 100-fold larger or smaller. The final column shows the number of NS implosions expected in a $t_{\rm u} \sim 13$ Gyr old MWEG hosting 10^9 1B*-distributed NSs.

3.4 Rare neutron star implosions from primordial black holes

Black holes formed from primordial perturbations during the radiation-dominated expansion of the early universe [134,135], with masses between $\sim 10^{41} - 10^{50}$ GeV, can be captured inside and subsequently consume neutron stars [136, 137]. As this work was being completed [138] appeared, which addresses PBH-induced NS implosions, and following [32], considers r-process elements and kilonovae produced by NS implosions. The maximum PBH-induced NS implosion rate for an MWEG found here differs markedly from [138], because we use the realistic, standard values for the NS population density, PBH density, and PBH velocity dispersion. We will find that NS implosions from primordial BHs (PBHs) in a typical Milky Way-like galaxy are rare.

PBHs with halo density $\rho_{\rm pbh}$ are captured by neutron stars at a rate [136]

$$C_{\rm pbh} = \sqrt{6\pi}\frac{\rho_{\rm pbh}}{m_{\rm pbh}}\left(\frac{2GMR}{v_{\rm x}}\right)\frac{1-{\rm Exp}\left[-\frac{3E_{\rm loss}}{m_{\rm pbh}v_{\rm x}^2}\right]}{1-\frac{2GM}{R}}, \tag{3.4}$$

where the energy loss of a PBH transiting the NS is $E_{\rm loss} \simeq \frac{4G^2 m_{\rm pbh}^2 M}{R^2}\left\langle\frac{\ln\Lambda}{2GM/R}\right\rangle$, and for a typical neutron star density profile $\left\langle\frac{\ln\Lambda}{2GM/R}\right\rangle \sim 14.7$. With Eq. (3.4) it can be verified that PBH capture in NSs is maximized for PBH masses $m_{\rm pbh} \sim 10^{44} - 10^{47}$ GeV. Assuming $m_{\rm pbh} \sim 10^{45}$ GeV PBHs make up the entire dark matter density, $\rho_{\rm pbh} \simeq \rho_{\rm x}$, we find that the PBH NS implosion rate appears too low to be detectable by next generation astronomical surveys, as shown in Figure 13.1 and Table 3.1.

3.5 Milky Way r-process enrichment and DES bounds on quiet kilonovae

NSs imploded by dark matter may eject a substantial amount of neutrons into the interstellar medium. Ejected neutron fluid will decompress, beta decay, and form a portion of the r-process elements observed in the Milky Way.

R-process elements are heavy elements with atomic masses around $80, 130, 195$, formed from neutron rich fluid at an as-yet undetermined astrophysical site. While core collapse supernovae have been historically favored as candidate sites for r-process production, recent observations of a high r-process abundance in Reticulum II, and low r-process abundance in other ultra faint dwarf galaxies, favors r-process production from rare events like a NS merger or NS implosion [32]. In the case of a NS implosion, the amount of NS fluid ejected will likely depend on tidal forces during the implosion [32], which require a complete hydrodynamical simulation to be properly modelled. However, it is known that in total, $\sim 10^4\ M_\odot$ of r-

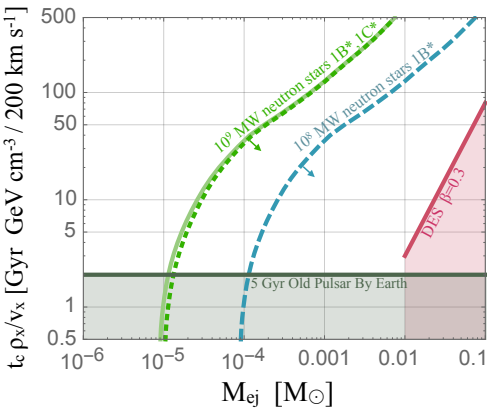

Figure 3.2: Bounds on dark matter-induced quiet kilonovae as a function of the neutron fluid mass ejected $M_{\rm ej}$ during a NS implosion. The DES bounds assume kilonovae with an ejection velocity $\beta = 0.3$c [35], and assume 10^9 NSs in an MWEG. Milky Way r-process elements produced from $M_{\rm ej}$ per NS implosion imply the indicated bounds [32], for either 10^8 or 10^9 total NSs, assumed to have spatial distribution 1B* or 1C* (arrows indicate the direction of excluded regions). Old pulsars in the Milky Way [27, 28] also set constraints. The x-axis indicates dark matter that implodes NSs in time $t_{\rm c}$ for background dark matter density $\rho_{\rm x}$ with velocity dispersion $v_{\rm x}$, expressed in units of $t_{\rm c}\rho_{\rm x}/v_{\rm x}$, see Eq. (3.2).

process elements must be formed to match the abundance seen in the Milky Way. Therefore, the amount of neutron fluid ejected per NS implosion can be bounded, by limiting the total NS mass ejected to $\sim 10^4\ M_\odot$ in the Milky Way. In Figure 3.2, we present such bounds, as a function of $t_{\rm c}\rho_{\rm x}/v_{\rm x}$. This can be compared to the final column of Table 3.1, which shows the expected number of NS implosions after ~ 13 Gyr.

Quiet kilonovae produced by NS-imploding dark matter can be searched for using state-of-the-art optical surveys. DES has recently published a null wide field optical search for kilonovae [35], which are the days-long luminous outbursts of beta-decaying neutron fluid ejected from NSs falling into BHs or other neutron stars. Because this search does not rely on a gravitational signature and instead seeks out beta decay emission from NS fluid flung into outer space, its findings can be used to constrain quiet kilonovae, *i.e.* NS fluid ejected from a NS implosion.

Because kilonovae light curves depend mainly on the mass and velocity of NS fluid ejected [139], bounds obtained for NS merger kilonovae can be applied to quiet kilonovae from NS implosions. We set this bound in Figure 3.2, computing the quiet kilonova rate for each $t_c\rho_x/v_x$ model point, assuming an MWEG containing 10^9 NSs.

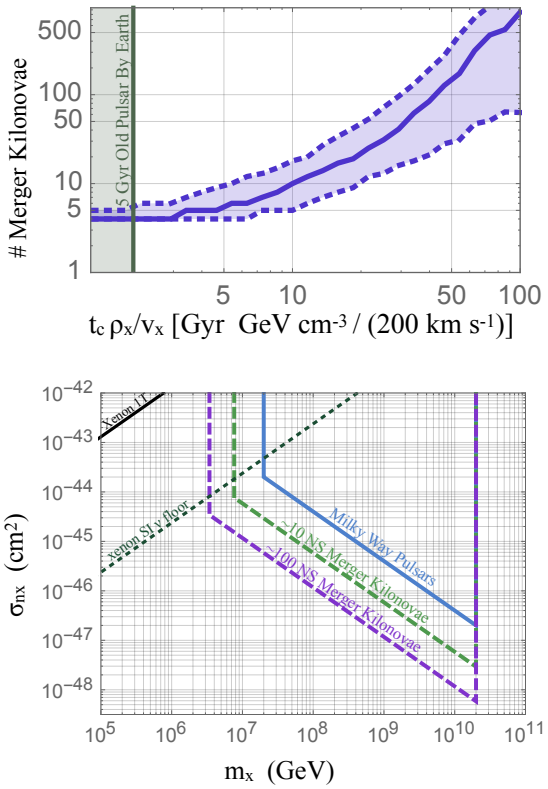

Figure 3.3: (Top) The number of NS mergers found by LIGO/Virgo, located to within $\sim$ 1 kpc in a host galaxy by optical imaging of a kilonova, required to exclude dark matter that implodes NSs in time t_c for background dark matter density ρ_x with velocity dispersion v_x, expressed in units of $t_c\rho_x/v_x$, see Eq. 1 in the main text. A Kolmogorov-Smirnov test was performed at each model point against the standard hypothesis that NS mergers track a standard distribution of NSs model 1B*) in a disc galaxy, for four hundred randomly generated merger data sets, allowing for up to 10^3 NS merger events per data set. Dotted bands indicate number of events needed for 2σ significance, for the upper and lower quartile of randomly generated merger data sets; the solid line indicates the median. (Bottom) The fermionic asymmetric dark matter-nucleon cross-section sensitivity obtainable with future observation of $\sim$ 10 and $\sim$ 100 NS merger kilonovae is shown, along with the MW pulsar bound [28], Xenon 1T bound [140], and the xenon neutrino floor [141], below which atmospheric neutrinos provide an irreducible background to dark matter scattering. Note that for fermionic dark matter masses $\gtrsim 10^{10}$ GeV, the black holes formed in NSs are too small and evaporate via Hawking radiation [124].

3.6 Searching for dark matter with NS mergers

Here we show how the galactocentric radial positions of $\sim$ 10 merger kilonovae would be sufficient to explore asymmetric dark matter-nucleon cross-sections orders of magnitude smaller than those presently probed using old pulsars in the Milky Way. The current generation of LV instrumentation is sensitive to gravitational strains on the order of 10^{-23} at an optimal frequency of 400 Hz, allowing for the observation of double neutron star (NS) binaries out to distances of $\sim$70 Mpc [34]. Anticipated upgrades will significantly expand this reach, as the amplitude of gravitational wave events is inversely proportional to the source distance, while the expected merger rate increases as the distance cubed. In the coming decade, up to hundreds of NS merger events are anticipated. Once a NS merger event is located to within $\sim$ 10 square degrees by LIGO/Virgo, wide field telescopes like BlackGEM [37] and the Zwicky Transient Factory are poised to image any subsequent kilonovae. The number of kilonovae found using this method will depend on their peak brightness, predictions for which range from -10 to -16 AB magnitude [35], while *e.g.* BlackGEM will perhaps probe a 100 degree field of view down to -14 AB magnitude for 200 Mpc distant mergers. As shown in Figure 3.1, galaxies with NS-imploding dark matter will have fewer NS merger kilonovae in their centers, where most NSs will have been converted to BHs. Therefore, the spatial distribution of merger kilonovae that can be used to test for dark matter. In the top panel of Figure 3.3, we show the results of a cumulative distribution test, where the standard (model "1B*") NS distribution defined Section 2, is tested against the distribution expected if dark matter is imploding neutron stars.

The altered NS merger distribution is calculated by taking the fraction of NSs converted into black holes shown in Figure 3.1, and applying this conversion frac-

tion to the 1B* expected distribution of NS mergers. The expected and dark matter-modified cumulative distribution functions of NS mergers in an MWEG are plotted in Appendix B.1. Statistical results were obtained by running 400 random Kolomogorov-Smirnov cumulative distribution trials, for each neutron star normalized implosion time ($t_c \rho_x / v_x$), to determine how many merger kilonovae located in galaxies would be necessary to detect NS-imploding dark matter at 2σ significance. Using the same methodology, in Section 3.7 we find that ~ 20 FRBs localized in galaxies would determine whether FRBs are a byproduct of NS implosions.

In practice, merger kilonovae occur in galaxies that are somewhat different from the Milky Way. To convert a measured galactocentric radius in a NS-merger-containing (non-Milky Way) galaxy, $r_{\rm nMW}$, to a Milky Way equivalent radius $r_{\rm MW}$, one can solve the formula

$$\frac{\rho_x^{\rm MW}(r_{\rm MW})}{v_x^{\rm MW}(r_{\rm MW})} = \frac{\rho_x^{\rm nMW}(r_{\rm nMW})}{v_x^{\rm nMW}(r_{\rm nMW})} \tag{3.5}$$

for $r_{\rm MW}$, where ρ_x and v_x are the dark matter density and velocity dispersion of the MWEG and non-Milky Way galaxies, as indicated. For example, the recently detected NS merger in NGC 4993 occurred in a $\sim 10^{10.9}\ M_\odot$ galaxy which would have an NFW profile defined by $\rho_0 = 0.34\ {\rm GeV/cm^3}$ and scale factor $R_s = 7.5$ kpc. The NS merger in NGC 4993 occurred at$\sim 2-3$ kpc from its center [142]. Solving Eq. (3.5), this corresponds to an Milky Way equivalent radius of 5-8 kpc. Note that this analysis also assumes that most identified NS mergers will have an age of ~ 10 Gyr – indeed, the NS merger progenitor found in NGC 4993 is projected to be this old [143].

In Figure 3.3, the per-nucleon cross-section sensitivity obtainable for heavy, asymmetric, fermionic dark matter is shown, as calculated using the capture rate

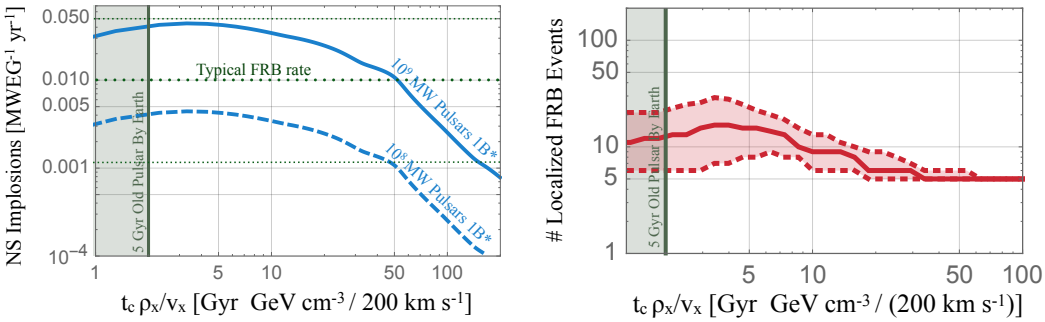

Figure 3.4: *Left*: The NS implosion rate in a Milky Way equivalent galaxy for dark matter that implodes NSs in time t_c for background dark matter density ρ_x with velocity dispersion v_x expressed in units of $\rho_x t_c/v_x$. The dotted lines indicate high, median, and low fast radio burst rate estimates from surveys [149, 150]. Implosion rates are shown for 10^8 and 10^9 NSs with a 1B* spatial distribution. *Right*: Number of fast radio bursts, localized to ~ 1 kpc in a host galaxy, required to test whether fast radio bursts originate from NS-imploding dark matter, against the hypothesis that FRBs come from a non-imploding population of NSs, at 2σ significance.

and collapse conditions presented in [128, 144] and Appendix B.2 in this document. Lighter asymmetric dark matter can also be found using these methods, as in Refs. [27–31, 123–125, 145–148].

3.7 Fast radio bursts from dark matter

Fast radio bursts (FRBs) are a newly-discovered class of millisecond-length ∼Ghz radio pulses found to distances of 2 Gpc with an all sky rate $\sim 10^4$/day, whose source is unknown [151, 152]. In [33] it was proposed that dark matter-induced NS implosions may be the source of FRBs. The electromagnetic energy released by a NS implosion matches what is required for an FRB [153–155]. Ref. [33] calculated the per MWEG NS implosion rate assuming a constant star formation history and a NS population that tracked the baryonic density in an MWEG. We improve on these rate calculations by using a realistic star formation history [131] and NS distribution, see Figure 3.4.

3.8 Gravitational waves from a neutron star implosion in the Milky Way

We have identified new signatures of neutron star-imploding dark matter, and fashioned qualitatively new methods for uncovering this dark sector using imminent astronomical observations. Specifically, our proposed analysis of NS merger kilonova locations has the potential to explore dark matter-nucleon scattering cross-sections up to ten orders of magnitude beyond present direct detection experiments. Finally, we note that the collapse of a neutron star into a BH could be detected directly at advanced LV, if the NS resides in the Milky Way. As we have calculated in Section 2, NS implosion event rates may be as large as 0.05 per year. Reference [156] finds the following strain for a NS collapsing to a BH, $h_c \sim 5 \times 10^{-22} \left(\frac{M}{M_\odot}\right) \left(\frac{10 \text{ kpc}}{D}\right)$ @ 531 Hz, so that advanced LV [157] may find an implosion out to $\sim$ 1 Mpc. We leave additional gravitational signatures of NS-imploding dark matter to future work, along with the application of the spatial kilonova analysis introduced here, to electromagnetic transients from exotic compact object mergers [144, 158].

CHAPTER 4

PROBING LIGHT SCALARS AND DARK PHOTONS AT BOREXINO AND LSND

4.1 Introduction

Search for light weakly coupled states undergoes a revival in recent years [42]. There has been increased interest in models that operate with light sterile neutrinos, axion-like particles, dark photons, and dark scalars that can be searched for in a variety of particle physics experiments. For a representative but incomplete set of theoretical ideas see, *e.g.* [43–51]. With more emphasis placed on the intensity frontier in recent years, experimental searches of exotic light particles are poised to continue [52].

Some of this interest is cosmology-driven, exploiting possible connection of light particles to dark matter, or perhaps to a force that mediates interactions between Standard Model and dark matter particles [45, 47, 50]. In many cases, the interest in light new states is motivated by "anomalous" results from previous experiments. The representative anomalies in that respect are the discrepancy in muon $g-2$ measurements [41], puzzling outcomes of some short baseline neutrino oscillation experiments [159–161], and most recently the discrepancy of the charge radius of the proton measured with the muonic and electronic probes [162, 163].

One of the most promising avenues for exploring very light and very weakly coupled states is by performing experiments in either deep underground laboratories, where the external backgrounds are very low, or large detectors usually built for the purpose of studying solar neutrinos. With the solar neutrino program cur-

rently measuring the last components of the neutrino flux, the usage of these large detectors shifts onto new applications. Thus, the KAMLAND and SNO+ detectors are (or will be) used to study double beta decays of Xe and Te isotopes [53, 54]. The Borexino detector will see the expansion of its program to include the sterile neutrino searches when new powerful external beta-decay sources are placed nearby [55].

There are also interesting proposals based on a possible usage of accelerators underground. Currently, relatively modest accelerators in terms of the energy and current intensity are used in the underground laboratories for measuring the nuclear-astrophysics-relevant reactions [56] or for calibration purposes [57]. These efforts can be significantly expanded. Powerful accelerators next to large neutrino detectors could open a new way of exploring the nature of light weakly coupled sectors [58–62].

In this chapter, we concentrate on the Borexino-SOX project that uses a radioactive ^{144}Ce$-^{144}$Pr source in close proximity to the detector. The source produces a large number of electron antineutrinos, and their signals inside the Borexino as a function of the distance from the source can reveal or constrain sterile neutrinos with commensurate oscillation length. In addition, it has already been pointed out that the same configuration will be sensitive to the emission of light scalar (or vector) particles in the transitions between the nuclear levels in the final point of the β-decay chain [60].

This chapter revisits the question of sensitivity of Borexino-SOX to light particles, and updates several aspects of [60]. We significantly expand the sensitivity reach by taking into account the decays of light particles inside the Borexino detector. Only scalar scattering on electrons was taken into account in the previous

consideration.

To have a more specific target in terms of the light particles, in section 4.2, we introduce a light scalar coupled to leptons and protons, which might be responsible for the resolution of the r_p discrepancy [164]. In section 4.3, we calculate the production rate of the scalars by relating it to the corresponding nuclear transition rate of ^{144}Nd. Taking into account the decay and the Compton absorption of the scalars inside the detector we arrive at the expected counting rate, and derive the sensitivity to coupling constants within the mass reach of this setup. Existing constraints on such light scalars are considered in section 4.4. In section 4.5, we study the sensitivity reach of the Borexino-SOX setup in probing light dark photons between a few hundred keV to 1 MeV with a small kinetic mixing (in full awareness of the fact that such light dark photons are disfavored by cosmology). We reach the conclusions in section 4.6.

4.2 Simplified model of a light scalar and the proton size anomaly

Following the rebirth of interest in dark photons, other models of light bosons have been closely investigated. In particular, scalar particles are quite interesting, not least because they are expected to couple differently to particles with different masses. While it is difficult to create a simple and elegant model of dark scalars with MeV range masses, some attempts have been made in refs. [165,166]. We will consider a simplified Lagrangian at low energy in the following form,

$$\mathcal{L}_\phi = \frac{1}{2}(\partial_\mu \phi)^2 - \frac{1}{2} m_\phi^2 \phi^2 + (g_p \bar{p} p + g_n \bar{n} n + g_e \bar{e} e + g_\mu \bar{\mu} \mu + g_\tau \bar{\tau} \tau)\phi. \tag{4.1}$$

In principle, such Lagrangian can be UV-completed in a variety of ways, although it is difficult to maintain both sizable couplings and small scalar mass m_ϕ. In this study, we will not analyze constraints related to UV completion, concentrating instead only on the low-energy physics induced by (4.1). This simplified Lagrangian with MeV/sub-MeV scalars was proposed in Ref. [164] (see also [167–170]) to explain a 7σ disagreement between the measurements of the proton-charge radius using $e-p$ systems and the more precise muonic Hydrogen Lamb shift determination of r_p.

More recent data with the Lamb shift in muonic deuterium [171] show no additional significant deviations associated with the neutron, so that the new physics interpretation of the anomaly prefers $g_n/g_p \ll 1$. Therefore, we will limit our considerations to $g_n = 0$ case, which will also remove all constraints associated with neutron-nucleus scattering [172]. Of course, the real origin of the r_p discrepancy is a hotly debated subject, and new physics is perhaps a solution of "last resort".

Introducing the product of couplings, $\epsilon^2 \equiv g_e g_p / e^2$, one can easily calculate corrections to the energy levels of muonic atoms due to the scalar exchange. When interpreted as an effective correction to the extracted proton radius from the hydrogen and muonic hydrogen, this scalar exchange gives

$$\Delta r_p^2|_{e\mathrm{H}} = -\frac{6\epsilon^2}{m_\phi^2},\ \Delta r_p^2|_{\mu\mathrm{H}} = -\frac{6\epsilon^2 (g_\mu/g_e)}{m_\phi^2} f(a m_\phi) \tag{4.2}$$

$f = x^4(1+x)^{-4}$ and $a \equiv (\alpha m_\mu m_p)^{-1}(m_\mu + m_p)$ is the μH Bohr radius. For the modifications of the deuterium energy levels, one should make $m_p \to m_\mathrm{D}$ substitution.

In particular, it may originate from the $g_\mu \gg g_e$ hierarchy, which would be expected from a scalar model. For simplicity, we will assume the mass-proportional coupling constants to the leptons and proton, thus $g_e = (m_e/m_\mu)g_\mu$, $g_\tau = (m_\tau/m_\mu)g_\mu$, $g_p = (m_p/m_\mu)g_\mu$, and plot the preferred parameter curve in Fig. 4.1 in green color on the $\epsilon^2 - m_\phi$ plane.

The best part of the new physics hypothesis is that it is ultimately testable with other experimental tools, of which there are many. The most direct way of discovering or limiting such particles is their productions in subatomic experiments with subsequent detection of new particle scattering or decay. The MeV-range masses suggested by the r_p anomaly make nuclear physics tools preferable. Such light scalars can be produced in nuclear transitions, and in the next section, we calculate their production in the gamma decay of selected isotopes that are going to be used in the search for sterile neutrinos.

4.3 Borexino-SOX experiment as a probe of scalar sector

Here we consider the Borexino-SOX setup in which a radioactive ^{144}Ce$-^{144}$Pr source will be placed 8.25 meters away from the center of the Borexino detector.

The decay of ^{144}Ce goes through $^{144}\text{Ce} \rightarrow \beta\nu^- + ^{144}\text{Pr}$ and then $^{144}\text{Pr} \rightarrow \beta\nu^- + ^{144}\text{Nd}(^{144}\text{Nd}^*)$. A fraction of the decays results in the excited states of ^{144}Nd* that γ-decay to the ground state. Then a small fraction of such decays will occur via an emission of a light scalar,

$$^{144}\text{Nd}^* \rightarrow {}^{144}\text{Nd} + \phi. \tag{4.3}$$

Small couplings of ϕ make it transparent to shielding and long-lived relative

to the linear scale of the experiment. Nevertheless, very rare events caused by the scalar can still be detected by the Borexino detector. The main processes via which such scalar can deposit its energy are:

$$\begin{aligned} e\phi &\to e\gamma, \text{ Compton absorption} \\ \phi &\to \gamma\gamma \ , \text{ diphoton decay} \\ \phi &\to e^+e^-, \text{ electron} - \text{positron decay} \end{aligned} \tag{4.4}$$

In what follows we put together an expected strength of such signal, starting from the probability of the scalar emission.

4.3.1 Emission of scalars in nuclear transitions

Let us find the probability of scalar particle emission in radioactive decays as a function of its mass and coupling. About one percent of the ^{144}Ce β-decays to the 2.185 MeV metastable state of Nd. This excited state, Nd*, then transitions to lower energy states via 1.485 MeV and 2.185 MeV gammas with approximately 30% and 70% branching ratios [57].

Ab initio calculation of a nuclear decay with an exotic particle in the final state could be a nontrivial task. Here, we benefit from the fact that the transition of interest (^{144}Nd$^* \to^{144}$ Nd) are E1 and the scalar coupling to neutrons is zero, which allows us to link the emission of the scalar to that of the γ-quanta and thus bypass complicated nuclear physics.

In the multipole expansion, the relevant part of the interaction Hamiltonian with photons is almost the same form as the corresponding counterpart of the

scalar interaction,

$$H_{\text{int},\gamma} \simeq e\omega A_0 \sum_p (\vec{\epsilon}\vec{r_p}); \quad H_{\text{int},\phi} \simeq g_p \sqrt{\omega^2 - m_\phi^2}\phi_0 \sum_p (\vec{n}\vec{r_p}), \tag{4.5}$$

where A_0, ϕ_0 are the amplitudes of the outgoing photon and scalar waves, $\vec{\epsilon}$ and $\vec{n}$ are the unit vectors of photon polarization and the direction of the outgoing waves, and the sum is taken over the protons inside the nuclei. After squaring the amplitudes induced by these Hamiltonians, summing over polarizations and averaging over $\vec{n}$, we arrive at both rates being proportional to the the same square of the nuclear matrix element, $\langle \sum_p \vec{r_p} \rangle$. In the ratio of transition rates it cancels, leaving us with the desired relation

$$\frac{\Gamma_\phi}{\Gamma_{\gamma,\ E1}} = \frac{1}{2}\left(\frac{g_p}{e}\right)^2 \left(1 - \frac{m_\phi^2}{\omega^2}\right)^{3/2}. \tag{4.6}$$

All factors in this rate are very intuitive: besides the obvious ratio of couplings, the 1/2 factor reflects the ratio of independent polarizations for a photon and a scalar, while $(1 - m_\phi^2/\omega^2)^{3/2}$ takes into account the finite mass effect.

4.3.2 Scalar decay and absorption

The Compton absorption $e+\phi \to e+\gamma$ process leads to the energy deposition inside the Borexino detector. Since only the sum of the deposited energy is measured, we would need a total cross section for this process. The differential cross section we derive is the same as Eq. (5) of [60] in the $m_\phi \ll E_\phi$ limit. But in this thesis we do not take the limit and use the full cross-section $\sigma(e + \phi \to e + \gamma)$. The absorption length is then given by $L_{\text{abs}} = 1/(n_e \sigma_{e\phi \to e\gamma})$, where n_e is the number density of electrons inside the Borexino detector. It is easy to see that for the fiducial choice of parameters, the absorption length is much larger than the linear size of the

detector. The Compton absorption process dominates in the very low m_ϕ regime, but the diphoton decays dominate in the medium and high mass range between a few hundred keV to 1.022 MeV (below pair production regime) as discussed below.

The diphoton decay rate of the light scalar ϕ can be derived recasting the Higgs result [173],

$$\Gamma(\phi \to \gamma\gamma) = \frac{\alpha^2}{256\pi^3} m_\phi^3 \left(\sum_{l=e,\,\mu,\,\tau} \frac{g_{\phi ll}}{m_l} \frac{2}{x_l^2} \left[x_l + (x_l - 1) \arcsin^2(\sqrt{x_l}) \right] \theta(1 - x_l) \right)^2 \quad (4.7)$$

where $x_l = \frac{m_\phi^2}{4m_l^2}$ and $\theta(x)$ is the Heaviside step function. In principle, all charged particles with couplings to ϕ will contribute to the rate. Here we take into account only the charged leptons, while the inclusion of quarks would require additional information, beyond assuming a g_p value. Therefore, this is an underestimation, with an actual $\Gamma(\phi \to \gamma\gamma)$ being on the same order but larger than (4.7). (One would need a proper UV-complete theory to make a more accurate prediction for the $\phi \to \gamma\gamma$ rate.)

When the mass of the scalar m_ϕ is larger than $2m_e$, the electron-positron decay will dominate the diphoton and Compton absorption processes. We have

$$\Gamma(\phi \to e^+e^-) = \frac{g_e^2 m_\phi}{8\pi} \left(1 - \frac{4m_e^2}{m_\phi^2} \right)^{3/2}. \quad (4.8)$$

The sum of these two rates determines the decay length,

$$L_{\rm dec} = \beta\gamma \left(\Gamma(\phi \to e^+e^-) + \Gamma(\phi \to \gamma\gamma) \right)^{-1}, \quad (4.9)$$

where β is the velocity of the scalar, which depends on its mass and energy, $\beta = \sqrt{1 - m_\phi^2/E^2}$ ($c = 1$ in our notations). The combination of absorption and decay,

$$L_{\rm dec,\,abs} = (L_{\rm dec}^{-1} + L_{\rm abs}^{-1})^{-1}, \quad (4.10)$$

is required for the total event rate.

The decay/absorption length together with the geometric acceptance determines the probability of energy deposition inside the detector per each emitted scalar particle,

$$\begin{aligned} P_{\text{deposit}} &= \int \frac{d(\theta)}{L_{\text{dec, abs}}} \frac{2\pi}{4\pi} d\cos\theta \\ &= \frac{1}{L_{\text{dec, abs}}} \int_{\sqrt{1-(R/L)^2}}^{1} \sqrt{R^2 - L^2(1-\cos^2\theta)}\, d\cos\theta \\ &= \frac{1}{L_{\text{dec, abs}}} \times \frac{2LR + (L^2 - R^2)\log\left(\frac{2L}{L+R} - 1\right)}{4L}, \end{aligned} \tag{4.11}$$

where a spherical geometry of the detector is considered. Here R is the fiducial radius and L is the distance of the radiative source from the center of the detector. For our numerical results we use $R = 3.02$ m and $L = 8.25$ m as proposed in the SOX project [174]. In the $L \gg R$ limit, the probability has a simple scaling with the total volume and the effective flux at the position of the detector,

$$P_{\text{deposit}} \simeq \frac{1}{L_{\text{dec, abs}}} \frac{\frac{4}{3}\pi R^3}{4\pi L^2}, \tag{4.12}$$

but we use the complete expression (4.11) for the calculations below.

4.3.3 Total event rate and sensitivity reach

Using formulae from the previous subsections, we can predict the signal strength as a function of m_ϕ and coupling constants. The excited state of ^{144}Nd has two gamma transitions, $E_0 = 2.185$ MeV and $E_1 = 1.485$ MeV, partitioned with $\text{Br}_0 = 0.7$ and $\text{Br}_1 = 0.3$ branching ratios. Thus, the signal would constitute peaks at 2.185 MeV and 1.485 MeV in the Borexino spectrum. We assume that the normal gamma quanta of these energies are efficiently degraded/absorbed by shielding.

The signal counting rate for a light scalar ϕ of energy E_i (2.185 MeV or 1.485

MeV as $i = 0$ or 1) in the Borexino detector is given by

$$\dot{N}_i = \left(\frac{dN}{dt}\right)_0 \exp\left(-\frac{t}{\tau}\right) \times \mathrm{Br}_{^{144}\mathrm{Nd}^*} \times \mathrm{Br}_i \times \frac{1}{2}\left(\frac{g_p}{e}\right)^2 \left(1 - \left(\frac{m_\phi}{E_i}\right)^2\right)^{3/2} \times P_{\mathrm{deposit},\,i} \quad (4.13)$$

Here, $\left(\frac{dN}{dt}\right)_0$ is the initial source radioactivity in units of decays per time, and the projected strength is $\simeq 5$ PBq, or 5×10^{15} decays per second. τ is the lifetime of ^{144}Cr, $\tau = 285$ days. $\mathrm{Br}_{^{144}\mathrm{Nd}^*}$ is the probability that the β-decay chain leads to the 2.185 MeV excited state of ^{144}Nd, $\mathrm{Br}_{^{144}\mathrm{Nd}^*} \simeq 0.01$. Finally, $P_{\mathrm{deposit},\,i}$ is the probability of decay/absorption defined in the previous subsection that depends on i via the dependence of the decay length and the absorption rate on E_i. Substituting relevant numbers we get the counting rate for the 2.185 MeV energy as

$$\begin{aligned}\dot{N}_{2.185\ \mathrm{MeV}}\left[\frac{\mathrm{counts}}{\mathrm{day}}\right] &= 1.5 \times 10^{18} \times \exp\left(-\frac{t[\mathrm{day}]}{285d}\right) \times \frac{\left(\frac{dN}{dt}\right)_0}{5\mathrm{PBq}} \\ &\quad \times \left(\frac{g_p}{e}\right)^2 \left(1 - \left(\frac{m_\phi}{2.185\mathrm{MeV}}\right)^2\right)^{3/2} \times P_{\mathrm{deposit},\,2.185\ \mathrm{MeV}} \quad (4.14)\end{aligned}$$

The resulting sensitivity reach of the three processes considered is plotted in the left panel of Fig. 4.1 as a blue curve. Here we assume the mass-proportional coupling strengths for ϕ to proton and leptons, and parametrize the coupling as $\epsilon^2 = g_p g_e / e^2$. The curve corresponds to a $3\,\sigma$ sensitivity level with the assumption that the initial source strength is 5 PBq.

For the derivation of the future sensitivity reach, we have followed the simplified procedure: For every point on the parameter space $\{m_\phi,\ \epsilon\}$, we calculate the expected counting rate using Eq. (4.13). We then take an overall exposure of $t_{exp} = 365$ days to arrive at an expected number of signal events as a function of mass and coupling, $N_{sig}(m_\phi, \epsilon)$. The background is the total number of events in energy bins near $E = 2.185$ MeV and $E = 1.485$ MeV. The energy resolution at

Borexino is $5\% \times \sqrt{1\text{MeV}/E}$. We use this as the bin size when we estimate the background rates at $E = 2.185$ MeV and $E = 1.485$ MeV. For the background event rate, we use the energy spectra shown in Fig. 2 in [174]. After all cuts, the background rate is $R_{backgr} \simeq 200$ counts/100t×100keV per 446.2 live-days at energy $E = 2.185$ MeV (For $E = 1.485$ MeV, the background rate is around 2300 counts/100t×100keV). For $E = 2.185$ MeV this gives the total number of background events to be $N_{backgr} \simeq 90$. We then require $N_{sig} < 3\sqrt{N_{backgr}}$ that results in the sensitivity curve in Fig. 1. Based on our estimation, the inclusion of $E = 1.485$ MeV channel does not lead to a significant improvement: it allows one to increase the significance by roughly 0.2σ with respect to just considering the main 2.185 MeV channel. Should a strong signal be observed, however, the presence of two peaks would be an unmistakable signature.

In the above procedure, we have taken into account only the existing source-unrelated backgrounds. However, a question arises whether additional inverse beta decay (IBD) events in Borexino, $p + \bar{\nu} \to n + e^+$, which is the primary goal of the SOX project, may also affect the search for $E = 2.185$ MeV abnormal energy deposition. If the location of IBD event is inside the fiducial volume, then even the threshold IBD event creates 3.2 MeV energy deposition. (The positron at rest produces 1.0 MeV energy, and the neutron capture results in the additional 2.2 MeV). This is well outside the energy windows for the signal from exotic scalars. Moreover, IBD events have a double structure in time, which can be used to discriminate them. An interesting question arises whether the location of IBD events outside the fiducial volume (*i.e.* close to the edge of the detector) may lead to a loss of positron signal followed by the neutron capture inside the fiducial volume. For a neutron with a typical kinetic energy of a keV would have to diffuse for at least 1m inside liquid scintillator to reach the fiducial volume. However, the estimates

of Ref. [175] show that the typical diffusion length is $O(5\,\mathrm{cm})$, which render the probability for such events to be small. Therefore, we conclude that source-induced IBD events would not lead to a significant increase in the background.

To be more inclusive, we also consider a variant of the scalar model when the couplings to electrons and tauons are switched off (muonic scalar). In this case, the remaining energy depositing channel is the diphoton decay, and there is no gain in sensitivity for $m_\phi > 2m_e$. We plot the corresponding sensitivity reach in the right panel of Fig. 4.1 also as a blue curve.

4.4 Comparing to existing constraints

Here we reassess some limits on the couplings of very light scalars. The most significant ones are from the beam dump experiments, meson decays and stellar energy losses. The particle physics constraints that rely on flavor changing processes are difficult to assess, as they would necessarily involve couplings of ϕ to the heavy quarks. We leave them out as model-dependent constraints.

4.4.1 Beam dump constraints

Among the beam dump experiments, the LSND is the leader given the number of particles it has put on target. The LSND measurements of the elastic electron-neutrino cross section [159, 176] can be recast to put constraints on the parameter space of our model. Here we revise previous bounds discussing different production channels, and account for scalar decays and Compton absorptions inside the LSND volume.

The collisions of primary protons with a target at LSND energies produce mostly pions and electromagnetic radiations. Exotic particles, such as scalars ϕ can be produced in the primary proton-nucleus collisions, as well as in the subsequent decays and absorptions of pions. A detailed calculation of such processes would require a dedicated effort. It would also require more knowledge about an actual model, beyond the naive Lagrangian (4.1). In particular, one would need to know how the scalars couple to pions and Δ-resonances, that alongside nucleons are the most important players in the inelastic processes in the LSND experiment energy range. Here we resort to simple order-of-magnitude estimates, assuming that the g_p coupling is the largest, and drives the production of scalars ϕ.

The important process for the pion production at LSND is the excitation of Δ resonance in the collisions of incoming protons with nucleons inside the target. Assuming that the decay of Δ's saturates the pion production inside the target, we can estimate the associated production of scalars in the $\Delta \to p + \pi + \phi$ process. To that effect, we consider the following two interaction terms,

$$\mathcal{L}_{int} \sim g_p \phi \bar{p} p + g_{\pi \Delta p} (\Delta_\mu p) \partial_\mu \pi, \tag{4.15}$$

where Δ_μ is the Rarita-Schwinger spinor of Δ-resonance, $g_{\pi \Delta p}$ is the pion-delta-nucleon coupling constant, and the isospin structure is suppressed. To estimate scalar production, we calculate the rates for $\Delta \to p + \pi$, $\Delta \to p + \pi + \phi$ and take the ratio finding

$$N_\phi \sim N_\pi \times \frac{\Gamma_{\Delta \to p \pi \phi}}{\Gamma_{\Delta \to p \pi}} \simeq N_\pi \times 0.04 g_p^2. \tag{4.16}$$

Notice that the decay rates are relatively large, being enhanced by the $\log(Q/m_\phi)$, where Q is the energy release. The coefficient 0.04 is calculated for $m_\phi = 1$ MeV, and it varies from 0.06 for $m_\phi = 0.2$ MeV to 0.03 $m_\phi = 2$ MeV.

Depending on their charges, pions have very different histories inside the target.

The negatively charged π^- undergoes nuclear capture. In [60] the rate of the scalar production in nuclear capture was overestimated, as it was linked to the production of photons in the capture of π^- by free protons via $e^2 \to g_p^2$ substitution. The radiative capture rate on protons is about 40%. For the LSND target, however, the more relevant process is the radiative capture on nuclei with $A \geq 16$, which is in the range of $\sim 2\%$ [177]. Therefore, one may use $N_\phi(\pi^-) \sim 0.02 \times N_{\pi^-} \times \left(\frac{g_\pi}{e}\right)^2$ as an estimate for the production rate of scalars from the π^- capture. Notice this is the coupling of scalars to pions that mostly determines the capture rate. Moreover, the number of π^- is smaller than the total pion production, and therefore we expect the production of ϕ in the π^- capture to be subdominant to Δ decays (4.16). Unlike the case with negatively charged pions, most of π^+ stop in the target and decay. The scalar particle is then produced in the three-body decay, $\pi^+ \to \mu^+ \nu \phi$, and in the four-body decay of the stopped μ^+, $\mu^+ \to e^+ \nu\nu\phi$. The decays of π^0 are instantaneous, and they could also lead to the production of light scalars in $\pi^0 \to \gamma\gamma\phi$. Direct estimates of the corresponding branching ratios give $\sim 0.05 (g_{\mu(\pi)})^2$, and again we find that this is subdominant to (4.16) estimate because of $g_{\mu(\pi)} < g_p$.

A conservative estimate of the number of pions produced in the experiment is $N_\pi \sim 10^{22}$ (see, *e.g.*, [176]). We take 300 MeV as an estimate for the average energy of scalars. Now we can estimate the expected number of events $N_{\rm LSND}$, *i.e.* the number of light scalars that deposit their energies in the LSND detector:

$$\begin{aligned} N_{\rm LSND} \sim & N_\pi \times 0.04\, g_p^2 \times P_{\text{survive + deposit in LSND}} \\ \simeq & N_\pi \times 0.04\, g_p^2 \times \left[\exp\left(-\frac{L_{\rm LSND} - \frac{d_{\rm LSND}}{2}}{L_{\rm dec}} \right) - \exp\left(-\frac{L_{\rm LSND} + \frac{d_{\rm LSND}}{2}}{L_{\rm dec,\,abs}} \right) \right] \left(\frac{A_{\rm LSND}}{4\pi L_{\rm LSND}^2} \right). \end{aligned} \tag{4.17}$$

Here we conservatively assume spatially isotropic distribution, take $L_{\rm LSND} = 30$ m

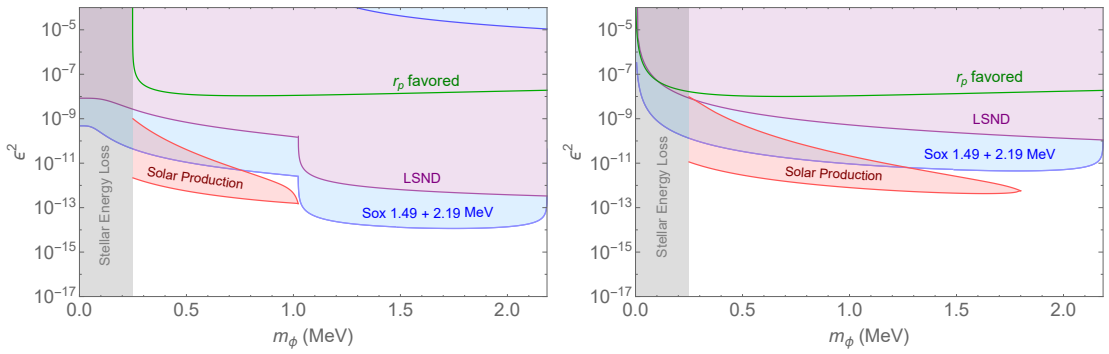

Figure 4.1: Future sensitivity reach of the Borexino-SOX setup and existing constraints placed on the coupling constant-mass parameter space. *Left panel:* The $g_i \propto m_i$ scaling is assumed and ϵ is defined as $\epsilon^2 = g_p g_e/e^2$. *Right panel:* $g_e = g_\tau = 0$, a $g_i \propto m_i$ scaling for μ and p, while $\epsilon^2 = (m_e/m_\mu) \times g_p g_\mu/e^2$. The green curve is the parameter space that can explain the proton-size anomaly. The experimental reach ($> 3\sigma$) by the Borexino-SOX setup is the blue regime. The recast of LSND constraints [176] is shown in purple, while the gray area is constrained by the stellar energy loss [179]. The solar production constraint [180] is the protruding pink area between $\epsilon^2 = 10^{-9}$ and 10^{-13}.

as the distance between the target and the center of the detector, $d_{\rm LSND} = 8.3$ m is the length of the detector itself, and $A_{\rm LSND} \simeq 25\,{\rm m}^2$ is the cross-section of the detector looking from the side [176, 178]. $L_{\rm dec,abs}$ are the decaying and absorption length determined by the physical processes Eq. (4.4). Notice that we no longer use the assumption that $L_{\rm dec,\,abs} \gg L_{\rm LSND}$ and $d_{\rm LSND}$ since in the high ϵ^2 regime these three lengths could be comparable. The number density of electrons in the LSND detector is $n_e = 2.9 \times 10^{29}$ m^{-3}, and the absorption again plays a subdominant role in the energy deposition process.

Based on Fig. 10 of [176] and Fig. 28 of [159] we estimate that there are less than 20 decay-in-flight events above 140 MeV during the exposure. We then determine the LSND constraint on the parameter space of the ϕ scalar as plotted in Fig. 4.1 in purple color. We reiterate a rather approximate nature of the estimates.

4.4.2 Solar emission and stellar energy loss

Thermal production of scalars may lead to abnormal energy losses (or abnormal thermal conductivity) that would alter the time evolution of well known stellar populations. In the regime of $m_\phi > T$, the thermally averaged energy loss is proportional to $g_e^2 \exp(-m_\phi/T_{\rm star})$. Given the extreme strength of stellar constraints [179], one can safely exclude $m_\phi < 250$ keV for the whole range of coupling constants considered in this thesis.

In addition, the non-thermal emission of scalars in nuclear reaction rates in the Sun can also be constrained. The light scalar ϕ can be produced in the Sun through the nuclear interaction p+D$\rightarrow {}^3$He$+\phi$. This process generates a 5.5 MeV ϕ flux that was constrained by the search conducted by the Borexino experiment. The flux can be estimated as

$$\Phi_{\phi,\rm solar} \simeq (g_p/e)^2 \Phi_{pp\nu} P_{\rm esc} P_{\rm surv}. \tag{4.18}$$

Here $\Phi_{pp\nu} = 6.0 \times 10^{10}$ cm$^{-2}s^{-1}$ is the proton-proton neutrino flux. $P_{\rm esc}$ is the probability of the light scalar escaping the Sun while $P_{\rm surv}$ is the probability of the scalar particle not decay before it reaches the Borexino detector.

$L_{\rm dec}$ is again determined by the decay processes in Eq. 4.4. For $m_\phi < 2m_e$ the ϕ particle can survive and reach the Borexino detector when $\epsilon < 10^{-9}$, and deposit its energy through processes in Eq. (4.4). For $m_\phi > 2m_e$ the $P_{\rm surv}$ is highly suppressed due to rapid di-electron decays and thus $m_\phi = 2m_e$ is where the constraint ends.

Notice that it is difficult to impose the supernovae (SN) constraints on this model, because of the uncertainties in the choices of some couplings. In general, we believe that the coupling of scalars to nucleons can be large enough so that

they remain trapped in the explosion zone, therefore avoiding the SN constraint.

4.5 Sensitivity to dark photons below 1 MeV

Dark photon is a massive "copy" of the regular SM photon, which couples to the electromagnetic current with a strength proportional to a small mixing angle ϵ, realized as a kinetic mixing operator. The low-energy Lagrangian for dark photons can be written as

$$\mathcal{L}_{\text{d.ph.}} = -\frac{1}{4}F'_{\mu\nu}F'^{\mu\nu} + \frac{1}{2}m^2_{A'}(A'_\mu)^2 + \epsilon A'^\mu J^{EM}_\mu. \tag{4.19}$$

Here J^{EM}_μ is an operator of the electromagnetic current.

This model is very well studied, and in many ways, it is more attractive than the model of scalars in (4.1) mainly because it has a natural UV completion. Zooming in on the parameter space relevant for the Borexino-SOX, we discover that above $2m_e$ the combination of all beam dump constraints put strong limits on the dark photon model. For $m_{A'} < 2m_e$ the most challenging constraint comes from cosmology, where the inclusion of three A' polarizations, fully thermalized with electron-photon fluid, will reduce the effective number of neutrino species to an unacceptable level $N_{eff} < 2$ [181]. Only a judicious choice of additional "passive" radiation could put this model back into agreement with cosmology.

Fully realizing all the complications coming from cosmology, we nevertheless estimate the sensitivity of the proposed setup to ϵ. An interesting feature of the dark photon model below the $2m_e$ threshold is that the main decay channel is 3γ, and it is mediated by the electron loop. The decay rate is very suppressed, and the effective-field-theory type calculation performed in the limit of very light

A' [182] was recently generalized to the $m_{A'} \sim 2m_e$ [183]. We take this decay rate, and in addition, calculate separately the cross section of the scattering process $e + A' \to e + \gamma$. Due to the strong suppression of the loop-induced decay, we find that the Compton-type scattering gives the main contribution to the signal rate in Borexino.

For the dark photon A', the emission rate (the rate of the nuclear state decay to A') is determined by

$$\frac{\Gamma_{A'}}{\Gamma_{\gamma,\ E1}} = \frac{v_{A'}(3 - v_{A'}^2)}{2}\epsilon^2, \tag{4.20}$$

where $v_{A'} = (1 - m_{A'}^2/\omega^2)^{1/2}$. In the limit of $m_{A'} \ll \omega$, the ratio of the two rates becomes simply ϵ^2. Substituting relevant numbers we get the counting rate for the 2.185 MeV energy as

$$\begin{aligned} \dot{N}_{A',\ 2.185\ \mathrm{MeV}} \left[\frac{\mathrm{counts}}{\mathrm{day}}\right] &= 1.5 \times 10^{18} \times \exp\left(-\frac{t[\mathrm{day}]}{285d}\right) \times \frac{\left(\frac{dN}{dt}\right)_0}{5\mathrm{PBq}} \\ &\quad \times \epsilon^2 \times v_{A'}(3 - v_{A'}^2) \times P_{\mathrm{deposit},\ 2.185\ \mathrm{MeV}} \end{aligned} \tag{4.21}$$

For the background event rate, we use the energy spectra shown in Fig. 2 in [174]. We use the 4th/green event spectrum with the fiducial volume (FV) cut. The background rate is around 200 counts/100t×100keV per 446.2 live-days at energy $E = 2.185$ MeV (For $E = 1.485$ MeV, the background rate is about 2300 counts/100t×100keV). We got the sensitivity curve in Fig. 2 by having an overal exposure of $t_{exp} = 365$ days and consider the coupling ϵ for each mass that gives $N_{sig} < 3\sqrt{N_{backgr}}$. The energy resolution at Borexino is $5\% \times \sqrt{1\mathrm{MeV}/E}$. We use this as the bin size when we estimate the background rates at $E = 2.185$ MeV and $E = 1.485$ MeV.

Even though the particle A' cannot decay to e^+e^- in the kinematic range we

consider, the decays to photons and the Compton-like absorption will lead to the beam dump constraints for this model. The LSND production is easy to estimate, given that π^0 will always have an $A'\gamma$ decay mode with $Br_{\pi^0\to A'\gamma} = 2\epsilon^2$.

A compilation of all the considerations above is shown in Fig. 4.2. We find that the sensitivity reach of the Borexino-SOX experiment, $\epsilon^2 \sim 10^{-10}$ in probing the light dark photons, is comparable but slightly above the bound from recasting the LSND data. Furthermore, this LSND bound covers up a small triangular parameter space for $10^{-5} \leq \epsilon \leq 10^{-4},\ m'_A \leq 2m_e$ that was not excluded by the cooling of Supernova 1987A [96,97], and the precision measurement of electron anomalous magnetic moment (see Fig. 7 of [96]), independently from the cosmological scenarios. Note that here we plot the "robust" constraint from [96] in our Fig. 4.2, which is the intersection of bounds from different supernova profile models. Also, both [96, 97] use the trapping criterion, rather than the energy transport criterion (see, *e.g.*, [184, 185]), to set the upper limits for the SN exclusion regions, with the trapping criterion being more conservative.

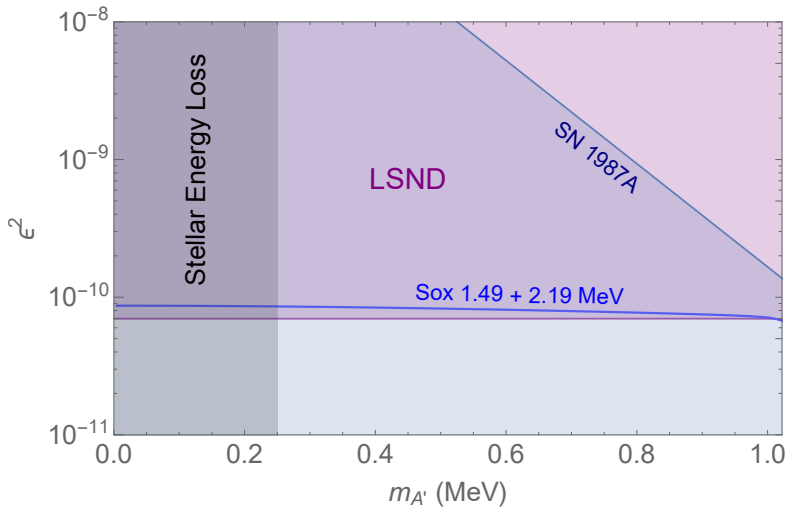

Figure 4.2: Future sensitivity reach for the Borexino-SOX setup and various existing constraints in coupling constant-mass parameter space for dark photons with a small mixing angle ϵ. The experimental reach ($> 3\sigma$) by the Borexino-SOX setup is the blue curve. The constraint recasting the LSND data [176] is slightly stronger than the Borexino-Sox reach, and excludes all the parameter space above the purple curve. Supernova cooling constrains the whole regime below the dark blue curve on the upper-right corner [96,97], while the gray area is again the stellar energy loss bound [179].

4.6 Conclusions

We have considered in detail how the search of the sterile neutrinos in the Borexino-SOX experiment can also be turned into a search for extremely weakly interacting bosons. The reach of the experiment to the parameters of exotic scalars is limited by the energy release in radioactive cascades. It has to be less than 2.185 MeV for the radioactive source to be used in SOX. However, in terms of the coupling constants, the reach of this experiment will be much farther down than even the most sensitive among the particle beam dump experiments. We find that with the proposed setup, coupling constants as low as $\epsilon^2 \sim 10^{-14}$ will be probed. The improved analysis in this work includes particle decays inside the detector as the main energy-deposition channel. It is the dominant process that significantly ex-

ceeds the scalar Compton absorption above the hundred-keV mass regime. Similar revisions will apply to searches proposed in Ref. [60] that suggest using proton accelerators to populate nuclear metastable states. In addition, we study the sensitivity reach of the Borexino-SOX experiment in probing a light dark photon below 1 MeV. The reach $\epsilon^2 \sim 10^{-10}$ is comparable, but slightly weaker than the bound already imposed by the existing LSND neutrino-electron scattering data. Combining this constraint with the supernova bound we completely rule out the possibility of having a light dark photon below 1 MeV in this coupling range.

In conclusion, one should not regard the SOX project as exclusively a search for sterile neutrinos (motivated mostly by experimental anomalies), but a generic search for dark sector particles. The scalar case considered in this thesis can be motivated by the proton charge radius anomaly, and the SOX project provides tremendous sensitivity to this type of models. We encourage the Borexino collaboration to perform its own study of the sensitivity to new bosons using more detailed information about background and efficiencies.

CHAPTER 5

DIPOLE PORTAL TO HEAVY NEUTRAL LEPTONS

The work presented in this Chapter is in collaboration with two other Ph.D. students, Gabriel Magill and Ryan Plestid, at McMaster University. Gabriel was in charge of deriving and including the production and detection of heavy neutral leptons (HNLs) in neutrino experiments and collider and produce the sensitivities and constraints of the HNLs. Ryan worked out the details of the meson decay production, the three-body Dalitz decays. Yu-Dai, the author of this thesis, worked on the early estimation of the SHiP sensitivity, derive the HNL production formula with Gabriel, helped collect experimental details, and derive the supernova constraints with Gabriel and Ryan.

The Standard Model of particles and fields (SM) shows remarkable resilience under the scrutiny of numerous particle physics experiments. In particular, the LHC experiments have put significant constraints on new hypothetical colored states, pushing their masses to a TeV scale and beyond. At the same time, owing to its smaller production cross sections, the electroweak extensions of the SM are far less constrained, and a plethora of new models may be hiding at energies of a few hundred GeV and beyond. If such sectors are considered to be heavy, their impact on the SM physics can be encoded in the higher-dimensional extensions of the SM. Moreover, the electroweak singlet components of such sectors can be light, and still coupled to the SM states. In the last few years, significant attention has been paid to the models containing new singlet fermionic states N (often referred to as heavy neutral leptons) that can couple to the SM leptons L and Higgs field H via the so-called neutrino portal coupling, NLH (see *e.g.* [186, 187]). Owing to the neutrality of N, its mass m_N is a free parameter with a wide range of

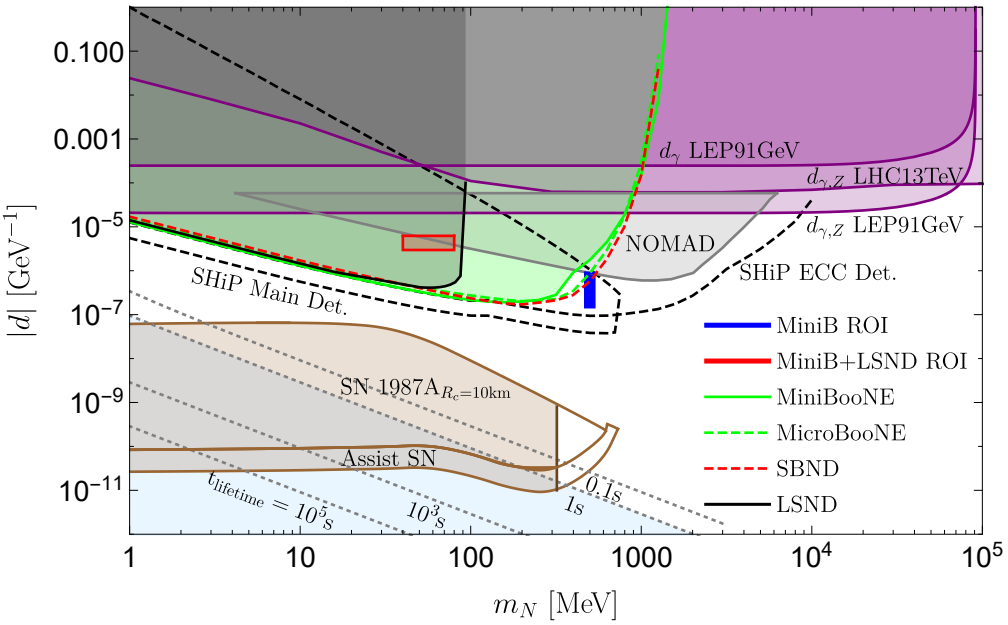

Figure 5.1: Overview of projected sensitivities (95% CL) and constraints obtained from SHiP, LHC, LEP, Supernova 1987A and experiments at the Short-Baseline Neutrino facility at Fermilab. We also show previously calculated favored regions of interest (ROI) in parameter space for MiniBooNE and LSND, and constraints from NOMAD. Limits are shown for the dimension 5 (γ mediator) and dimension 6 ($\gamma + Z$ mediators) extensions. Each curve is discussed and presented in detail in [5].

possibilities from the sub-eV scale and up, all the way to the Planck scale. This range is somewhat narrower if N is indeed taking part in generating masses for the light active neutrino species. A great deal of experimental activity is devoted to searches of N particles, that may show up in cosmological data, in neutrino oscillation experiments, in meson decays, beam dump experiments and at high energy colliders. (For a recent overview of neutrino portal see *e.g.* [114].)

Given large interests in searches of heavy neutral leptons, in this work we will analyze a less conventional case of N particles coupled to the SM via the so-called dipole portal encoded in the following effective Lagrangian,

$$\mathcal{L} \supset \bar{N}(i\partial\!\!\!/ - m_N)N + (d\bar{\nu}_L \sigma_{\mu\nu} F^{\mu\nu} N + h.c). \tag{5.1}$$

Here $F^{\mu\nu}$ is the electromagnetic field strength tensor, and ν_L is a SM neutrino field. This is an effective Lagrangian that needs to be UV completed at energy scales not much larger than $\Lambda \sim d^{-1}$. We are going to stay on the effective field theory grounds, noting that since our results show the sensitivity to d to be much better than TeV^{-1}, the UV completion scale can be raised above the electroweak scale. For now, Eq. (5.1) is also applicable only at energies below the weak scale, as it does not respect the full SM gauge invariance.

The main assumption made in Eq. (5.1) is the absence, or subdominance, of the mass mixing operator NLH. When the mass mixing operator is dominant, the production and decay of N particles is mostly governed by its interaction with the SM particles via weak bosons. The phenomenological consequences of these minimally coupled particles N is well understood. In contrast, if the leading order operator is suppressed, the dipole operator offers novel signatures and features in the production and decay of N, such as a much enhanced role of electromagnetic interactions in the production and decay of N. This case has so far being addressed only in a handful of works [48, 188–192], and here we would like to present a comprehensive analysis of the dipole N portal, and derive constraints on d that result from a variety of different experiments, both at high and medium energies.

Previously dipole interactions of neutrinos have been studied in several specific contexts (that we are aware of). If the SM neutrinos have a large flavor off-diagonal EM dipole moment, the interaction of solar and reactor neutrinos may get enhanced. This provides stringent limits on dipole moments of SM neutrinos [193]. Some theoretical and phenomenological aspects of the Dirac HNL dipole operator were discussed in Refs. [194, 195] (see also a more recent general discussion of dimension 5 effective operators in the neutrino sector [196]). A phenomenological

sensitivity study of this magnetic dipole operator has been considered for IceCube [197]. There, owing to the large incoming SM neutrino energies, the signature of interest was a coincident double energy deposit from the DIS production of N, and its subsequent decay. Another prominent place where the transitional $\nu - N$ dipole appears is the literature on searches of sterile neutrino dark matter via a dipole-induced decay $N \to \nu\gamma$ ([198] and references therein). A more closely related case to the topic of our study has arisen as a consequence of trying to accommodate MiniBoone and LSND anomalies, that we would like to discuss now in more detail.

While there is an overall theoretical/experimental consistency for the three-neutrino oscillation picture, there are several experimental results that do not fit in. Two notable exceptions are the anomalies observed at the intensity frontier experiments LSND and MiniBooNE [63, 64]. In these experiments, an excess of low energy electron (anti-)neutrinos have been observed, the source of which is currently unknown. Conceivably, there are two possibilities: new physics or some unaccounted SM processes. Thus, for example, single photons produced via poorly understood SM neutrino interactions with nuclei [199] might lead to some partial explanation of the anomalies. (At the signal level, a single photon cannot be distinguished from charged-current quasi-elastic events by MiniBooNE's Cherenkov detector.)

The most popular proposal is the existence of a light ($m \sim$ eV) sterile neutrino ([200] and references therein), which mediates the anomalous oscillation required to explain the observed excess signal. A possibility of eV sterile neutrinos being at the origin of the MiniBooNE and LSND oscillation results is strongly challenged by cosmological data. Indeed, the required parameters for mass splitting and mixing angle will lead to a complete thermalization of a new sterile species via oscillation

mechanism. This stands in sharp disagreement with cosmological data (in particular, cosmic microwave background (CMB), Big Bang Nucleosynthesis (BBN) and late-time cosmology) that constrain not only the total number of thermally populated relativistic degrees of freedom in the early Universe, but also limits the total neutrino mass $\sum m_\nu \leq 0.17$ eV at 95%CL [201]. Consequently, a single eV sterile neutrino is not consistent with cosmology in the absence of new physics. At the very least, the minimal model would need to be modified to suppress the oscillations in the early Universe, which is usually achieved at the expense of significantly enlarging the sterile neutrino sector *e.g.* by new types of interactions with dark matter and/or baryons [202, 203]. Thus, the sterile neutrino solution to the MiniBooNE and LSND anomalies naturally leads to the idea of a *dark sector*, with new matter and interaction states.

An alternative attempt to accommodate the anomalies without using eV-scale sterile neutrinos requires some dark sector states comparable in mass to the lightest mesons. Thus, it has been noted that the presence of a new sub-GeV neutral fermion N may mimic the signals observed at MiniBooNE and LSND [48, 188]. The necessary ingredient of this proposal is a new fermionic state N in the 10-to-few-100 MeV mass range and the dipole coupling in Eq. (5.1). This coupling mediates a relatively prompt decay of N to a normal neutrino and a photon, a signature that can be confused with the "normal" electron or positron final state in charged current events [48, 188]. Whether this model can simultaneously account for both anomalies without running into problems with other constraints remain an open issue (see the discussions in Refs. [48, 188–192]). At the same time the model has a clear advantage over the eV sterile neutrino model, as it creates no problems with cosmology, as N states will decay to the SM at early times before

the neutrino decoupling.

Continuing investment in neutrino physics will eventually lead to better understanding of the origin of these two anomalies. The Short-Baseline Neutrino program (SBN) [204] is going to be instrumental in testing the MiniBooNE anomaly. The design consists of three Liquid Argon time projection chamber (LAr-TPC) detectors that overcome the difficulties present at MiniBooNE by providing excellent photon/electron discrimination. Furthermore, the SBN program will use a near detector (SBND) to control systematic errors related to the neutrino beam content. Being close to the proton target, SBND will see a much larger neutrino flux than the mid-range detectors and will allow a more accurate measurement of the neutrinos before oscillation. In addition, a further increase in sensitivity may result from a proposed new experiment at CERN, Search for Hidden Particles (SHIP) [114], that will be able to significantly advance the probes to N states, and should also test their dipole interactions. For an analysis of a more conventional CC-dominated model of HNLs in application to Fermilab experiments we refer the reader to a recent paper [205].

Motivated by the relative simplicity of the neutrino dipole portal model and its potential applicability to neutrino anomalies, it is very useful to have a comprehensive survey of the model over a large region of parameter space. We therefore consider the energy, intensity and astrophysics frontiers, where this portal can be probed. A plot summarizing our results is shown in Fig. 6.1, and the rest of this chapter considers each probe individually. The existing constraints from previous dark matter experiments can be improved by the SBN and SHiP. From astrophysics, MeV HNLs could contribute to the supernova cooling, in particular that

of Supernova 1987A (SN 1987A). This happens when the coupling d is large enough so that the star can produce N in sufficient quantity, but small enough so that N can escape and cool down the star without being significantly impeded. For lifetimes longer than $0.1\text{s} - 1\text{s}$, N is relevant for, and can modify predictions of, BBN. The late decays of HNLs would modify the proton to neutron ratio, and with some reasonable assumptions about the initial cosmological temperatures being high, this puts an upper bound on the lifetime of N. We find that there is significant overlap of this region with SN constraints. Lastly, for above GeV masses, we turn to particle colliders and recast existing searches from the LHC and LEP.

CHAPTER 6

MILLICHARGED PARTICLES IN NEUTRINO EXPERIMENTS

The work presented in this Chapter is in collaboration with two other Ph.D. students, Gabriel Magill and Ryan Plestid, at McMaster University. Gabriel took charge of including the production channels and the detection signatures of mCP (millicharged particles) in neutrino experiments and produced the sensitivity and constraint figures. Ryan worked out the details of the meson decay production, the three-body Dalitz decays. Yu-Dai, the author of this thesis, derive the Drell-Yan production of the mCPs in detail, estimated the LSND sensitivity, helped collect experimental details, and discussed the link of our work to mCP dark matter and the implications on the 21-cm absorption-signal anomaly by the EDGES collaboration.

Introduction: Extensions of the Standard Model (SM) by light weakly charged particles, and their probes at the intensity frontier experiments have become an important direction of modern particle physics [206]. One of the simplest and most natural ways of coupling new particles to the SM is via a "kinetic mixing" or "hypercharge portal" [44, 207], which at low energies may lead to millicharged particles (mCPs), that would seemingly contradict the observed quantization of electric charge in nature [66]. In recent years, a wide class of related models were studied in connection with dark matter [45, 47, 67] (see also [61, 208–216]), and mCPs can be viewed as a specific limit of those theories.

It is well appreciated that both proton and electron beam dump experiments provide sensitive probes of vector portal models. In particular, production and scattering of light dark matter [209] has been studied as a function of mediator mass $m_{A'}$, dark sector coupling α_D, dark matter mass m_χ, and kinetic mixing

parameter ϵ_Y. Depending on the relation between these parameters, either the past electron beam dump facilities [212] or the proton fixed target experiments with a primary goal of neutrino physics [61,210] provide the best sensitivity. However, the simplest limit of $m_{A'} \to 0$, when the parameter space simplifies to the mass and effective charge of mCPs, $\{m_\chi, \epsilon\}$, was analyzed only in the context of electron beam dump experiments [217, 218]. Clearly, fixed target neutrino experiments, such as the existing data from MiniBooNE [65] and the Liquid Scintillator Near Detector (LSND) [178], and the soon to be released data from MicroBooNE, the ongoing SBN program [204], the Deep Underground Neutrino Experiment (DUNE) [219], and the proposed Search for Hidden Particles (SHiP) [220] serve as a fertile testing ground of MeV–GeV physics due to their high statistics [4,5,61,210]. These experiments all serve as promising avenues to probe mCPs.

The purpose of this *chapter* is twofold: First, we demonstrate that existing data from LSND provides leading bounds on mCPs (surpassing existing constraints from SLAC's mQ experiment [217]) in the low mass regime ($m_\chi \lesssim 35$ MeV). Likewise, newly released data from MiniBooNE [65] can set more stringent bounds on mCPs in the mass range of 100 MeV $\lesssim m_\chi \lesssim$ 180 MeV. Second, we predict that by optimizing search strategies at ongoing and upcoming experiments (such as MicroBooNE, SBND, DUNE, and SHiP), fixed source neutrino experiments can serve to provide leading bounds for mCPs over the full range of masses 5 MeV $\lesssim m_\chi \lesssim 5$ GeV. The detection signature of mCPs in these experiments is elastic scattering with electrons, and we find that detection prospects are highly sensitive to the threshold imposed on the electron's recoil energy. Therefore, significant gains in sensitivity to mCPs may be achieved by future experiments by optimizing

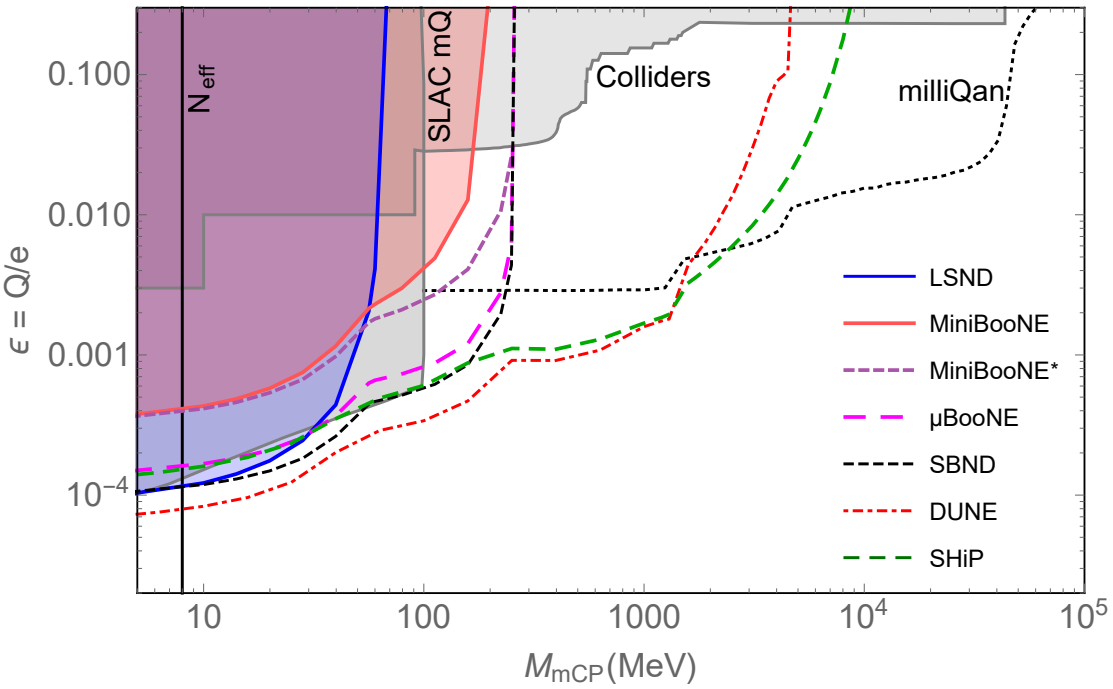

Figure 6.1: Exclusion curves for fermionic mCPs (results are broadly similar for scalars). Existing data is shown as solid lines, while projections are shown as dashed curves. The kinematic reach of a given experiment is set by the heaviest meson of interest it can produce. This is π^0 for LSND, η for the Booster experiments, and Υ for DUNE. At SHiP, Drell-Yan production extends the kinematic reach to roughly 10 GeV. The sensitivity of each experiment can be understood via Eq. (6.4) while the relevant parameters for each experiment are summarized in Table 6.1.

the detection of low energy electrons.

Our results have direct implications for models with late kinetic coupling of dark matter and baryons [221] that could lead to extra cooling of the baryon fluid and spin temperature at redshifts $z \sim 20$, which may result in a more pronounced 21 cm absorption signal. If a fraction of dark matter is composed of mCPs, this extra cooling mechanism can be naturally realized [222, 223], and fit the unexpected signal reported by Experiment to Detect the Global Epoch of Reionization Signature (EDGES) [224]. The interpretation of the EDGES result as shedding light on dark matter-baryon interactions necessitates a careful consideration of existing

laboratory constraints. Our analysis reveals that sensitivities from LSND, SBND, SHiP, and DUNE can explore previously unprobed regions of parameter space that are favored by the 1%-mCP fractional dark matter hypothesis [223, 225, 226] and by a proposal to use mCPs to reduce electron number (while maintaining charge neutrality) to achieve an earlier decoupling of the baryon gas from the CMB [227].

Production and detection: Fixed target neutrino experiments rely on the production of neutrinos from weak decays of charged pions. In generating a large flux of $\pi^{\pm}$ these experiments necessarily also produce a similar number [i.e. $\mathcal{O}(10^{20})$] of π^0 [215]. For large beam energies, other neutral mesons (e.g. η, Υ, J/ψ) are also produced. Any significant branching ratios to lepton pairs necessarily implies an associated decay to pairs of mCPs, resulting in a significant flux of mCPs even for extremely small charges. In the case of η and π^0, Dalitz decays $\pi^0/\eta \to \gamma\chi\bar{\chi}$ dominate, while for J/ψ and Υ direct decays, $J/\psi, \Upsilon \to \chi\bar{\chi}$ are the most important. The branching ratio for a meson, $\mathcal{M}$, to mCPs is given roughly by

$$\mathrm{BR}(\mathcal{M} \to \chi\bar{\chi}) \approx \epsilon^2 \times \mathrm{BR}\big(\mathcal{M} \to X e^+ e^-\big) \times f\Big(\frac{m_\chi}{M}\Big), \tag{6.1}$$

where M is the mass of the parent meson, X denotes any additional particles, and $f(m_\chi/M)$ is a phase space factor that decreases slowly as a function of m_χ/M. The number of mCPs passing through the detector is a function of both the branching ratio and geometric losses which can vary substantially between experiments (see Table 6.1).

We now turn to the detection of mCPs in the neutrino experiments, where the predominant signature is elastic scattering with electrons. The dominance of electron scattering as a detection signal is related to the low-Q^2 sensitivity of the scattering cross section. Explicitly, in the limit of small electron mass, we have

$$\frac{\mathrm{d}\sigma_{e\chi}}{\mathrm{d}Q^2} = 2\pi\alpha^2\epsilon^2 \times \frac{2(s - m_\chi^2)^2 - 2sQ^2 + Q^4}{(s - m_\chi^2)^2 Q^4}. \tag{6.2}$$

Upon integrating over momentum transfers, we see that the total cross section will be dominated by the small-Q^2 contribution to the integral. In this limit, we have $\mathrm{d}\sigma_{e\chi}/\mathrm{d}Q^2 \approx 4\pi\alpha^2\epsilon^2/Q^4$, and so we see that $\sigma_{e\chi} \approx 4\pi\alpha^2\epsilon^2/Q^2_{\mathrm{min}}$. We may relate Q_{min} in the lab frame to the recoil energy of the electron via $Q^2 = 2m_e(E_e - m_e)$ [1]. An experiment's recoil energy threshold, $E_e^{(\mathrm{min})}$, then sets the scale of the detection cross section as

$$\sigma_{e\chi} = 2.6 \times 10^{-25}\mathrm{cm}^2 \times \epsilon^2 \times \frac{1\ \mathrm{MeV}}{E_e^{(\mathrm{min})} - m_e}. \tag{6.3}$$

Consequently, sensitivity to mCPs can be greatly enhanced by accurately measuring low electron energy recoils (an important feature for search strategies at future experiments).

Results: We now discuss the details of the modeling and analysis used to create Fig. 6.1. The various curves are obtained by performing a sensitivity analysis [228]: given a number of predicted background events b and data n, the number of signal events s_{up} consistent with the observation and backgrounds at $(1-\alpha)$ credibility level is found by solving the equation $\alpha = \Gamma(1+n, b+s_{\mathrm{up}})/\Gamma(1+n, b)$ where $\Gamma(x, y)$ is the upper incomplete gamma function [229]. We choose a credibility interval of $1-\alpha = 95\%$ and calculate the corresponding bounds implied by s_{up} on our mCP model according to the formula

$$s_{\mathrm{up}} = \sum_{\mathrm{Energies}} N_\chi(E_i) \times \frac{N_e}{\mathrm{Area}} \times \sigma_{e\chi}(E_i;\ m_\chi) \times \mathcal{E}. \tag{6.4}$$

Based on Eqs. (6.1) and (6.3), we see that $s_{\mathrm{up}} \propto \epsilon^4$. Here, ϵ is the mCP electric charge (in units of e), $N_\chi(E_i)$ represents the number of mCPs with energy E_i arriving at the detector, $\sigma_{e\chi}(E_i)$ is the detection cross section consistent with the angular and recoil cuts in the experiment, N_e is the total number of electrons in-

[1] Note that for nucleon scattering, the cross section $\sigma \propto 1/Q^2$ is suppressed by $1/m_p$ rather than $1/m_e$.

	N [$\times 10^{20}$]		$A_{\rm geo}(m_\chi)[\times 10^{-3}]$		Cuts [MeV]		
Exp.	π^0	η	1 MeV	100 MeV	$E_e^{\rm min}$	$E_e^{\rm max}$	Bkg
LSND	130	—	20	—	18	52	300
mBooNE	17	0.56	1.2	0.68	130	530	2K
mBooNE*	1.3	0.04	1.2	0.68	18	—	0*
μBooNE	9.2	0.31	0.09	0.05	2	40	16
SBND	4.6	0.15	4.6	2.6	2	40	230
DUNE	830	16	3.3	5.1	2	40	19K
SHiP	4.7	0.11	130	220	100	300	140

Table 6.1: Summary of the lifetime meson rates (N), mCP detector acceptances ($A_{\rm geo}$), electron recoil energy cuts, and backgrounds at each of the experiments considered in this thesis. In all experiments a cut of $\cos\theta > 0$ is imposed in our analysis (*except for MiniBooNE's dark matter run where a cut of $\cos\theta > 0.99$ effectively reduces backgrounds to zero [230]). For the SHiP and DUNE experiments, we also include J/ψ and Υ mesons as well as Drell-Yan production which are discussed in the text. We use an efficiency of $\mathcal{E} = 0.2$ for Cherenkov detectors, $\mathcal{E} = 0.5$ for nuclear emulsion detectors, and $\mathcal{E} = 0.8$ for liquid argon time projection chambers. The data at LSND and MiniBooNE is taken from [176] and [65] respectively. Projections at MiniBooNE* [231], MicroBooNE [232], SBND [204], DUNE [219] and SHiP [114] are based on expected detector performance.

side the active volume of the detector, $\mathcal{E}$ is an overall electron detection efficiency. "Area" in (6.4) stands for the active volume divided by the average length $\langle l \rangle$ traversed by particles inside the detector. The total exposure is contained in $N_\chi(E_i)$. For most of the mCP parameter space under consideration, electromagnetic decays of mesons provide the dominant flux contribution, whereas Drell-Yan production (DYP) dominates for the large mCP masses that are only accessible at DUNE and SHiP.

To estimate how many mCPs of energy E_i arrive at the detector, we model the angular and energy distributions of the mesons using one of several empirical formulas to be discussed below. Given a meson produced at a certain angle and energy, we numerically sample its branching ratio to mCPs over all possible angles and energy in the lab frame, and determine the fraction of its branching ratio to

mCPs in which one of such particles has energy E_i and is pointed towards the detector. Repeating this procedure over all production energies and angles of the meson yields the meson contribution to $N_\chi(E_i)$. For DYP of mCPs from a quark and anti-quark pair, we integrate over the full production phase-space using MSTW parton distribution functions [233], and using Heaviside functions, we select the proportion of events containing an mCP pointed towards the detector, with energy E_i.

We now focus the discussion on the details of each experiment. In Table 6.1, we show for each experiment: the lifetime rates for π^0 and η mesons, the geometric acceptance $A_{\rm geo}(m_\chi)$ [2], the cuts that we have imposed, and the expected number of background events. Using Eq. (6.4) this is sufficient information to approximately reproduce our results.

At LSND, the π^0 spectrum is modeled using a Burman-Smith distribution [234,235] assuming 2 years of operation on a water target and 3 years of operation on a tungsten target. Our LSND analysis is based on [176], which featured 1.7×10^{23} protons on target (POT), a beam energy of 0.798 GeV, and a single electron background of approximately 300 events with energies ranging between 18 MeV and 52 MeV. We estimate the N_e/Area in Eq. (6.4) to be $2.5 \times 10^{26}\ e^-/\text{cm}^2$.

The meson spectrum from Fermilab's Booster Neutrino Beam (BNB) is relevant for MiniBooNE, MicroBooNE, and SBND. The BNB delivers 8.9 GeV POT and so can produce substantial numbers of both π^0 and η mesons. The former's angular and energy spectra are modeled by the Sanford-Wang distribution [215, 236], and η mesons by the Feynman Scaling hypothesis [236]. These distributions are com-

[2] Defined as the ratio between the number of mCPs that reach the detector and the total number produced.

mon across all three of the aforementioned experiments. We have compared our geometric acceptances with those generated using [215] and reasonable (to within an $\mathcal{O}(1)$ factor) agreement.

At MiniBooNE we perform two distinct analyses: First we consider the recently updated neutrino oscillation search [65]. We combine data from both neutrino and anti-neutrino runs and consider a sample of 2.41×10^{21} POT for which we take the single electron background to be 2.0×10^3 events and the measured rate to be 2.4×10^3. Next, motivated by a dedicated dark matter search with 1.86×10^{20} protons on target [112], we consider an anticipated parallel analysis [231] involving electron-recoil data. Backgrounds were suppressed by operating the beamline in an "off-target" mode, (i.e. not collimating charged pions), and these can be further suppressed (to zero) by imposing a cut of $\cos\theta > 0.99$ on the electron's recoil angle [230]. In both cases we estimate an electron number density of $3.2 \times 10^{26}\ e^-/\text{cm}^2$. The sensitivity curve quoted in Fig. 6.1 assumes that the upcoming analysis reports no signal consistent with mCPs.

At MicroBooNE, the meson rates assume 1.32×10^{21} POT and we estimate that the detector has an electron density of $3.9 \times 10^{26}\ e^-/\text{cm}^2$. The chosen recoil cuts are based on the lowest reaches achievable given the wire spacing in MicroBooNE's liquid argon detector [232]. The wire spacing is 3 mm and the ionization stopping power is approximately 2.5 MeV/cm, so electrons with total energy larger than at least 2 MeV produce tracks long enough to be reconstructed across two wires. Based on this and the requirement for ionization signals that don't shower, we limit ourselves to recoil cuts between 2 MeV and 40 MeV. The treatment of SBND is broadly similar to MicroBooNE, but we assume 6.6×10^{20} POT, which corresponds to half the run time of MicroBooNE.

At SHiP we assume 2×10^{20} POT and a near neutrino detector 50 m from the beam stop with an electron density of $2.7 \times 10^{26}\ e^-/\text{cm}^2$. Beam energies of 400 GeV allow us to include J/ψ and Υ, in addition to π^0 and η. We do not include mesons such as ρ, ω and ϕ, because they do not serve to significantly alter the sensitivity offered by J/ψ (although their inclusion would only increase sensitivity at SHiP for $m_\chi \lesssim 400$ MeV). At SHiP's energies, production of π^0 and η is described by the BMPT distributions [215, 237]. These distributions are slightly different depending on the mass of the meson with the η having a spectrum that is more forward pointed. We have compared our geometric acceptances to those obtained using [215] and found reasonable agreement, with our acceptances being smaller by a factor of four. For production of J/ψ, we assume that their energy production spectra are described by the distributions in [238]. These distributions rely on production being highly peaked in the forward direction and parameterized as $\mathrm{d}\sigma/\mathrm{d}x_F \propto (1 - |x_F|)^5$, where $x_F = 2p_\parallel/\sqrt{s}$ is the meson's longitudinal component in the COM frame of the collision. We account for geometric losses by using an empirical formulae for the p_T distribution provided in [239]. We assume that the production spectrum of Υ mesons are similarly given, and normalize their total cross section to the data in [240]. Using this, we have reproduced the Pb rates in Table 3 of [241] for J/Ψ, and for Υ we reproduced the Pt rates in Table 1 of [242]. For our results in Fig. 6.1 we estimate $N_{J/\psi} = 2.1 \times 10^{15}$ with an acceptance of $A_{\text{geo}}(100\text{ MeV}) = 8 \times 10^{-2}$, and $N_\Upsilon = 1.2 \times 10^{11}$ with $A_{\text{geo}}(100\text{ MeV}) = 7.2 \times 10^{-2}$. For large mCP masses, DYP becomes the main production mechanism. We calibrate our DYP calculations by reproducing the dimuon invariant mass spectrum in Fig. 11 of [243] from the FNAL-772 experiment [244].

At DUNE, our treatment of meson production is very similar to the treatment at SHiP. We model pseudoscalar meson production using the BMPT distribution,

as before, but use a beam energy of 80 GeV [219] and account for differences in the target material. We also include J/ψ and Υ mesons and treat them as described above. Our detector treatment and electron recoil cuts are motivated by the capability of MicroBooNE's liquid argon time projection chamber (LAr-TPC) detector, and in particular its ability to measure low energy electron recoils. We assume 3×10^{22} POT and a 30 tonne liquid argon detector which corresponds to $5.4 \times 10^{25}\ e^-/\text{cm}^2$. We estimate $N_{J/\psi} = 3 \times 10^{16}$ with an acceptance of $A_{\text{geo}}(100\text{ MeV}) = 2.4 \times 10^{-3}$ and $N_\Upsilon = 5.1 \times 10^9$ with $A_{\text{geo}}(100\text{ MeV}) = 3.7 \times 10^{-3}$. Lastly, it is important to point out that our results do not include multiple scattering effects through dirt. Low velocity mCPs with a moderate charge (i.e. $\epsilon \gtrsim 0.03$) might get impeded by their long transit through dirt. This is relevant for DYP at DUNE and could weaken our sensitivity for $m_\chi \gtrsim 2$ GeV. Larger ϵ may also lead to a double scattering of mCPs inside the detectors, which could be used as an additional tool of discriminating their signature against the neutrino background.

We now discuss our modeling of the single electron backgrounds appearing in Table 6.1. We consider two classes of backgrounds: those coming from each experiments flux of neutrinos [i.e. $\nu e \to \nu e$ and $\nu n \to e p$], and those coming from sources such as cosmics, mis-identified particles, or dirt related events.

We treat neutrino induced backgrounds in detail for each experiment by summing over the neutrino fluxes from each collaboration and accounting for the detection efficiencies $\mathcal{E}$. A large background reduction is obtained by imposing the electron recoil cuts $E_e^{(\text{max})}$ shown in Table 6.1. These do not significantly affect the signal (which is dominated by low electron recoils), but *do* significantly reduce charged and neutral current backgrounds [245, 246]. In the case of MiniBooNE's anticipated dark matter run based on electron recoils, the angular requirements

already provide a powerful background discriminant and the maximum energy of the electron is determined by the kinematics of the event.

We model the external sources of backgrounds by multiplying the neutrino induced backgrounds by an overall multiplicative factor. LAr-TPC detectors can use timing information as vetoes to reduce additional sources of backgrounds; this is not possible in a nuclear emulsion chamber. Therefore, we multiply our neutrino induced backgrounds by a factor of 10 for LAr-TPC detectors (MicroBooNE, SBND, and DUNE) and a factor of 25 for nuclear emulsion detectors (SHiP); this increase in the backgrounds decreases our sensitivity to ϵ by $20-30\%$. Although our procedure is clearly an estimate, we emphasize that our results in Fig. 6.1 can be easily revised for different background assumptions according to [229].

Outlook: We have shown that mCPs can be probed at fixed target neutrino experiments due to the large number of mesons produced with electromagnetic decay pathways. Using existing data, LSND and MiniBooNE are able to provide the leading sensitivity to mCPs for certain sub-GeV masses. Beyond serving as a test of fundamental physics, this newfound sensitivity has implications for models of physics beyond the Standard Model. In particular it further restricts the parameter space of cosmological models where a fraction of mCP dark matter results in extra cooling of baryons that modifies 21 cm physics at high redshifts.

Equally important are our projected sensitivities at MicroBooNE, SBND, DUNE, and SHiP. The success of these experiments as probes of mCPs will rely heavily on their respective collaborations' search strategies. In particular, by working to increase the sensitivity to low energy electron recoils the predicted signal rate can be enhanced with a scaling proportional to $1/(E_e - m_e)$. MicroBooNE has shown preliminary work that suggests sensitivity to electron recoils with kinetic

energies as low as 300 keV [232]. If this can be achieved, it is conceivable that the combined sensitivity of LSND, SBND, MicroBooNE, DUNE and SHiP will provide the leading sensitivity to mCPs in the full range of 5 MeV $\lesssim m_\chi \lesssim$ 5 GeV.

We close by noting that further progress may come from new experimental concepts and innovations. Significant progress may come from coupling large underground neutrino detectors with purposely installed new accelerators [61, 62]. Millicharged particles may also be searched by experiments in *disappearance* channels [109–111], where $e^+e^- \to \gamma + \chi + \bar{\chi}$ and $Z + e^- \to Z + e^- + \chi + \bar{\chi}$ production leads to anomalous missing momentum/energy from the χ-pair that pass through a detector without depositing energy. Because of the advantageous scaling with ϵ (second, rather than the fourth power), there are clear prospects on improving bounds on mCPs above the 100 MeV energy range.

APPENDIX A

USEFUL FORMULAE FOR THERMAL DARK MATTER

A.1 Boltzmann Equations

The Boltzmann equation for the DM phase space distribution, $f_\chi(\mathbf{p};t)$, in an expanding Universe is

$$\frac{\partial f_\chi}{\partial t} - H\frac{p^2}{E}\frac{\partial f_\chi}{\partial E} = C[f_\chi]\,, \tag{A.1}$$

where $E = \sqrt{\mathbf{p}^2 + m_\chi^2}$, $H(t)$ is the Hubble expansion rate, and $C[f_\chi]$ is the collision term. For ELDER dark matter, the relevant collision terms are the $3 \to 2$ self-annihilations and χ-ψ elastic scattering (ψ can be any light SM particle). The collision terms also includes annihilations to SM, but their effect in the ELDER scenario is negligible, and are omitted. Strong elastic self-scattering of ELDERs ensures that, throughout the kinetic decoupling and freeze-out process, the phase space distribution follows a thermal distribution:

$$f_\chi = \frac{1}{e^{(E-\mu_\chi)/T'} - 1}\,, \tag{A.2}$$

where $\mu_\chi(t)$ is the chemical potential, and $T'(t)$ is the temperature of the dark sector. Eq. (A.1) can be most easily solved by taking the first two moments, the DM number density n and energy density ρ:

$$n_\chi = g_\chi \int \frac{d^3p}{(2\pi)^3} f_\chi, \qquad \rho_\chi = g_\chi \int \frac{d^3p}{(2\pi)^3} E f_\chi, \tag{A.3}$$

where g_χ is the number of degrees of freedom in χ. These obey

$$\frac{\partial n_\chi}{\partial t} + 3Hn_\chi = -\langle\sigma_{3\to2}v^2\rangle\left(n_\chi^3 - n_\chi^2 n_\chi^{\rm eq}\right), \tag{A.4}$$

$$\frac{\partial \rho_\chi}{\partial t} + 3H\left(\rho_\chi + P_\chi\right) = -\langle\sigma_{el}v\delta E\rangle n_\chi n_\psi, \tag{A.5}$$

where $n_\chi^{\rm eq}$ is the density of χ in chemical equilibrium (*i.e.* at zero chemical potential). The thermally averaged $3 \to 2$ annihilation and energy transfer rates are

$$\begin{aligned} n_\chi^3 \langle \sigma_{3\to 2} v^2 \rangle &= \frac{1}{3!2!} \int d\Pi_{\chi_1} d\Pi_{\chi_2} d\Pi_{\chi_3} d\Pi_{\chi_4} d\Pi_{\chi_5} (2\pi)^4 \delta^4 \left(p_{\chi_1} + p_{\chi_2} + p_{\chi_3} - p_{\chi_4} - p_{\chi_5} \right) \\ &\quad \times f_{\chi_1} f_{\chi_2} f_{\chi_3} \overline{|\mathcal{M}_{\chi_1\chi_2\chi_3\to\chi_4\chi_5}|^2}, \end{aligned} \tag{A.6}$$

$$\begin{aligned} n_\chi n_\psi \langle \sigma_{el} v \delta E \rangle &= \int d\Pi_{\chi_1} d\Pi_{\psi_1} d\Pi_{\chi_2} d\Pi_{\psi_2} (2\pi)^4 \delta^4 \left(p_{\chi_1} + p_{\psi_1} - p_{\chi_2} - p_{\psi_2} \right) \\ &\quad \times (E_{\chi_2} - E_{\chi_1}) f_{\chi_1} f_{\psi_1} \overline{|\mathcal{M}_{\chi_1\psi_1\to\chi_2\psi_2}|^2}, \end{aligned} \tag{A.7}$$

where

$$d\Pi_i \equiv \frac{g_i d^3 p_i}{(2\pi)^3 2E_i} \tag{A.8}$$

is the Lorentz invariant phase-space integration volume. The squared matrix elements, $\overline{|\mathcal{M}|^2}$, are averaged over initial and final degrees of freedom, including spin, color, and charge.[1]

During the kinetic decoupling and freeze-out process, the χ particles, to a good

[1]For the case of complex χ considered in this thesis, we treat χ and χ^* as two states of the same particle, and averaging over these two states for each initial and final dark matter particle. For instance, for self-scattering

$$\begin{aligned} \overline{|\mathcal{M}_{\chi_1\chi_2\to\chi_3\chi_4}|^2} &\equiv \frac{1}{2^4}\Big(|\mathcal{M}(\chi_1\chi_2 \to \chi_3\chi_4)|^2 + |\mathcal{M}(\chi_1^*\chi_2^* \to \chi_3^*\chi_4^*)|^2 + |\mathcal{M}(\chi_1\chi_2^* \to \chi_3\chi_4^*)|^2 \\ &\quad + |\mathcal{M}(\chi_1\chi_2^* \to \chi_3^*\chi_4)|^2 + |\mathcal{M}(\chi_1^*\chi_2 \to \chi_3\chi_4^*)|^2 + |\mathcal{M}(\chi_1\chi_2^* \to \chi_3^*\chi_4)|^2 \Big). \end{aligned} \tag{A.9}$$

and for $\chi^{(*)} e^\pm \to \chi^{(*)} e^\pm$ in the dark photon portal,

$$\overline{|\mathcal{M}_{\chi_1\psi_1\to\chi_2\psi_2}|^2} = \frac{1}{2^2}\frac{1}{4^2}\Big(|\mathcal{M}(\chi e^-)|^2 + |\mathcal{M}(\chi e^+)|^2 + |\mathcal{M}(\chi^* e^-)|^2 + |\mathcal{M}(\chi^* e^-)|^2 \Big) = \frac{e^2 g_D^2 \epsilon_\gamma^2 m_\chi^2}{m_V^4} E_e^2 \left(1 + \cos\theta\right), \tag{A.10}$$

where E_e and $\cos\theta$ are the electron energy and scattering angle, respectively, in the center-of-mass frame of the collision. Setting $\cos\theta = 1$ (corresponding to $t = 0$) in this equation yields Eq. (2.26).

approximation, follow a Maxwell-Boltzmann distribution. Then,

$$f_\chi = \left(\frac{n_\chi}{n_\chi^{\rm eq}}\right) f_\chi^{\rm eq} \qquad \Longrightarrow \qquad \rho_\chi = \left(\frac{n_\chi}{n_\chi^{\rm eq}}\right) \rho_\chi^{\rm eq}, \qquad P_\chi = \left(\frac{n_\chi}{n_\chi^{\rm eq}}\right) P_\chi^{\rm eq}. \tag{A.11}$$

Here 'eq' denotes the values of the variables in chemical equilibrium, $\mu_\chi = 0$:

$$\begin{aligned} n_\chi^{\rm eq} &= \frac{g_\chi m_\chi^2 T'}{2\pi^2} K_2(m_\chi/T'), \\ \rho_\chi^{\rm eq} &= \frac{g_\chi m_\chi^2 T'}{2\pi^2} \left(m_\chi K_1(m/T') + 3T' K_2(m_\chi/T')\right), \\ P_\chi^{\rm eq} &= \frac{g_\chi m_\chi^2 T'^2}{2\pi^2} K_2(m_\chi/T'), \end{aligned} \tag{A.12}$$

and $n_\chi/n_\chi^{\rm eq} = e^{-\mu_\chi/T'}$. The Boltzmann equations (A.4), (A.5) then reduce to a system of coupled partial differential equations for T' and μ_χ (or equivalently T' and n_χ).

In the epoch of interest, the entropy of the universe is dominated by relativistic SM degrees of freedom: $s_0 = \frac{2\pi^2}{45} g_{*s} T^3$, where T is the SM plasma temperature, and $g_{*S} = 10.75$ at the relevant temperatures (0.5 MeV $\lesssim T \lesssim$ 100 MeV). The contribution of ELDERs to the entropy is suppressed both because they are non-relativistic, and because the number of degrees of freedom is small compared to SM. Neglecting this contribution, the time variable in the Boltzmann equations can be conveniently traded for the SM temperature:

$$\frac{\partial}{\partial t} = -\left(1 + 3\frac{T}{g_{*s}(T)}\frac{\partial g_{*s}(T)}{\partial T}\right)^{-1} HT\frac{\partial}{\partial T}. \tag{A.13}$$

A.2 Kinetic Decoupling and Approximate Analytic Solution

Since the relic density of ELDER dark matter is primarily determined at the time of its kinetic decoupling from the SM, we would like to obtain analytic insight into this process. Kinetic decoupling occurs before freeze-out of the $3 \to 2$ interactions,

so that $\mu_\chi = 0$ throughout the decoupling process. The ELDERs can then be completely characterized by their temperature T', whose evolution is dictated by Eq. (A.5). In this section, we describe an approximate analytic solution to this equation, which in turn yields an analytic estimate of the ELDER relic density.

In the limit that the non-relativistic χ particles are scattering off thermalized relativistic ψ particles, an approximate analytic form of the energy transfer rate integral, Eq. (A.7), can be found. In Ref. [247], this was achieved by expanding the integrand in small momentum transfer. Here we present the necessary equations, but refer the reader to detailed calculation in the Appendix of [247]. First the thermally averaged energy transfer rate is written in terms of the collision operator in the non-relativistic limit:

$$\begin{aligned} n_\chi n_\psi \langle \sigma_{el} v \delta E \rangle &\simeq \int d\Pi_{\chi_1} d\Pi_{\psi_1} d\Pi_{\chi_2} d\Pi_{\psi_2} (2\pi)^4 \delta^4 \left(p_{\chi_1} + p_{\psi_1} - p_{\chi_2} - p_{\psi_2}\right) \\ &\quad \times \left(\frac{p_{\chi_1}^2}{2m_\chi} - \frac{p_{\chi_2}^2}{2m_\chi} \right) f_{\chi_1} f_{\psi_1} \overline{|M_{\chi_1\psi_1 \to \chi_2\psi_2}|^2} \\ &= -\int d\Pi_{\chi_1} d\Pi_{\psi_1} d\Pi_{\chi_2} d\Pi_{\psi_2} (2\pi)^4 \delta^4 \left(p_{\chi_1} + p_{\psi_1} - p_{\chi_2} - p_{\psi_2}\right) \\ &\quad \times \frac{p_{\chi_1}^2}{2m_\chi} (f_{\chi_1} f_{\psi_1} - f_{\chi_2} f_{\psi_2}) \overline{|M_{\chi_1\psi_1 \to \chi_2\psi_2}|^2} \\ &= -\int d\Pi_{\chi_1} \frac{p_{\chi_1}^2}{m_\chi} C[f_{\chi_1}]. \end{aligned} \tag{A.14}$$

Using Eq. (B.22) in [247]

$$C[f_{\chi_1}] = \frac{g_\psi^2 g_\chi}{12(2\pi)^3} m_\chi^2 c_n N_{n+3}^\psi \left(\frac{T}{m_\chi} \right)^{n+4} \left[m_\chi T \nabla_{p_{\chi_1}}^2 + \vec{p}_{\chi_1} \cdot \vec{\nabla}_{p_{\chi_1}} + 3 \right] f_{\chi_1}(p_{\chi_1}) \,, \tag{A.15}$$

where c_n is the leading coefficient of the matrix element expanded in E_ψ / m_χ at zero momentum transfer

$$\overline{|\mathcal{M}|^2}_{\substack{t=0 \\ s=m_\chi^2 + 2m_\chi E_\psi}} \equiv c_n \left(\frac{E_\psi}{m_\chi} \right)^n + \ldots, \tag{A.16}$$

and

$$N_j^\psi = \frac{j+1}{T^{j+1}} \int dE_\psi E_\psi^j f_\psi(E_\psi) = \begin{cases} (1-2^{-j})\ (j+1)!\,\zeta(j+1) & \psi \in \text{fermion}, \\ (j+1)!\,\zeta(j+1) & \psi \in \text{boson}. \end{cases} \tag{A.17}$$

If expanding the matrix element around $t = 0$ is not a good expansion, for instance, if the amplitude vanishes as $t \to 0$, then one should replace A.16 with the t-averaged matrix element [248]. Taking f_χ to be the Maxwell-Boltzmann distribution at temperature T' and integrating over the collision operator yields

$$n_\chi n_\psi \langle \sigma_{el} v \delta E \rangle \simeq n_\chi \frac{c_n g_\psi^2 g_\chi m_\chi N_{3+n}^\psi}{32\pi^3} \left(\frac{T}{m_\chi}\right)^{4+n} (T' - T). \tag{A.18}$$

Note that when the two sectors have the same temperature, the energy transfer vanishes, which is expected for particles in thermal equilibrium. The energy transfer rate can be related to the more commonly used quantity $\langle \sigma_{el} v \rangle$, as follows:

$$\langle \sigma_{el} v \delta E \rangle \simeq 2(n+3) \frac{N_{3+n}^\psi}{N_{2+n}^\psi} \frac{T}{m_\chi} (T' - T) \langle \sigma_{el} v \rangle. \tag{A.19}$$

When the $3 \to 2$ process is active and the dark matter particles are non-relativistic, they follow equilibrium Maxwell-Boltzmann distributions, and the energy density Boltzmann equation (A.5) gives a differential equation for the temperature

$$\frac{\partial T'}{\partial T} = 3\frac{T'^2}{m_\chi T} + a \left(\frac{T}{m_\chi}\right)^{1+n} \frac{T'^2}{m_\chi^2} \frac{(T' - T)}{m_\chi}, \tag{A.20}$$

where

$$a \equiv \frac{c_n g_\psi^2 g_\chi m_\chi N_{3+n}^\psi}{32\pi^3 H_{T=m_\chi}}. \tag{A.21}$$

On the right-hand side, there are two competing terms. The first term contributes to the cannibalization of the dark matter, which tends to increase the dark temperature relative to the SM. The second term, which comes from the elastic scattering term, pushes $T' \to T$. The scattering term falls faster with temperature, and at

some point will no longer be able to compete. At that time, the dark matter will thermally decouple from the SM bath, and cannibalization will take over the evolution of the dark sector. This decoupling occurs roughly when the second term is of order one:[2]

$$T_d \simeq m_\chi a^{-1/(4+n)}. \tag{A.22}$$

After decoupling, the second term can be ignored, and dark temperature grows only logarithmically relative to the SM temperature,

$$T' \simeq \frac{T_d}{1 + 3\frac{T_d}{m_\chi}\log\frac{T_d}{T}}\,, \tag{A.23}$$

until the dark matter freezes out.

We can attempt to find the analytic asymptotic behavior of the Boltzmann equations. Recasting Eq. (A.20) in terms of x and x' yields

$$\frac{\partial x'}{\partial x} = \frac{3}{x} + \frac{a x^{-n-4}(x - x')}{x'}\,. \tag{A.24}$$

There appears to to be no closed form solution to the above differential equation, but the following differential equation does have a closed form solution:

$$\frac{\partial x'}{\partial x} = \frac{3}{x} + \frac{a x^{-n-4}(x - x')}{x}\,. \tag{A.25}$$

In the limit $x \ll x_d$, $x = x'$ so the two differential equations are approximately the same. Likewise, when $x \gg x_d$, the 2nd term is negligible in both equations, so the change is not relevant. The closed form solution to Eq. (A.25) is

$$x' = e^t \left(\left(\frac{a}{n+4}\right)^{\frac{1}{n+4}} \Gamma\left(\frac{n+3}{n+4}, t\right) - \frac{3\mathrm{Ei}(-t)}{n+4} \right) \tag{A.26}$$

[2]The kinetic decoupling temperature can also be estimated by observing that in equilibrium, the rate of energy transfer to the SM must keep up with the rate of kinetic energy release by $3 \to 2$ annihilations: $n_e\langle\sigma_{el} v \delta E\rangle \sim -m_\chi^2 H T^{-1}$. According to Eq. (A.19), $\langle\sigma_{el} v \delta E\rangle \sim \langle\sigma_{el} v\rangle T^2/m_\chi$. This approach, which was used in Ref. [1], gives a result consistent with Eq. (2.6).

where $t \equiv \frac{a x^{-n-4}}{n+4}$, Γ is the incomplete gamma function and $\mathrm{Ei}(-t) = -\int_t^\infty \frac{e^{-z}}{z} dz$. The asymptotic limits of this solution at small and large x are

$$x'(x \to 0) = x\,, \tag{A.27}$$

$$x'(x \to \infty) = 3\log(x) + \left(\frac{a}{n+4}\right)^{\frac{1}{n+4}} \Gamma\left(\frac{n+3}{n+4}\right) - 3\log\left[e^{\frac{\gamma_E}{n+4}} \left(\frac{a}{n+4}\right)^{\frac{1}{n+4}}\right] \tag{A.28}$$

The second limit is very similar to the cannibalization result

$$\frac{\partial x'}{\partial x} = \frac{3}{x}, \quad x'[x_d] = x_d \qquad \Longrightarrow \qquad x' = 3\log(x) + x_d - 3\log(x_d), \tag{A.29}$$

since $\Gamma(\frac{n+3}{n+4}) \approx e^{\frac{\gamma_E}{n+4}} \approx 1$. Therefore we make the identification for the decoupling temperature

$$x_d \simeq \left(\frac{a}{n+4}\right)^{\frac{1}{n+4}} \Gamma\left(\frac{n+3}{n+4}\right). \tag{A.30}$$

This agrees with the rough estimate of Eq. (A.22), and provides the precise value of the numerical coefficient. Assuming instantaneous freeze-out of the $3 \to 2$ annihilations at the dark sector temperature x'_f (corresponding to SM plasma temperature x_f), the dark matter yield is given by

$$Y(x_f) \equiv \frac{n'(x_f)}{s(x_f)} = \frac{g_\chi m_\chi^3 e^{x'_f}/(2\pi x'_f)^{3/2}}{\frac{2\pi^2}{45} g_{\star s} m_\chi^3/x_f^3} \simeq \frac{0.1 \frac{g_\chi}{g_{\star s,\,f}} a^{\frac{3}{8}} e^{-0.87 a^{1/4}}}{\left(1 + \frac{3.4}{\sqrt[4]{a}} \log x_f\right)^{3/2}}. \tag{A.31}$$

Here, the exponential dependence of relic density on the elastic scattering rate is manifest. We also note a logarithmic dependence on the temperature at freeze-out, which shows only a very minor dependence on the $3 \to 2$ rate, provided it is still active at decoupling.

A.3 Thermally-Averaged $3 \to 2$ Rate

Here we present the necessary formulas to calculate the thermally averaged $3 \to 2$ rate in thermal equilibrium, in the non-relativistic regime ($T \ll m_\chi$). Assuming

Maxwell-Boltzmann distribution, which is justified when the dark matter is highly non-relativistic, the integral can be written in terms of 2-body and 3-body phase space integrals:

$$\begin{aligned}\langle\sigma_{3\to 2}v^2\rangle &= \frac{1}{3!2!}\frac{1}{(n_\chi^{\rm eq})^3}\int d\Pi_{\chi_1}d\Pi_{\chi_2}d\Pi_{\chi_3}d\Pi_{\chi_4}d\Pi_{\chi_5}(2\pi)^4\delta^4\left(p_{\chi_1}+p_{\chi_2}+p_{\chi_3}-p_{\chi_4}-p_{\chi_5}\right)\\ &\quad\times f_{\chi_1}f_{\chi_2}f_{\chi_3}\overline{|\mathcal{M}|^2}\\ &= \frac{1}{(n_\chi^{\rm eq})^3}\frac{g_\chi^5}{3!2!}\int\frac{d^3p_{\chi_1}}{(2\pi)^3 2E_{\chi_1}}\frac{d^3p_{\chi_2}}{(2\pi)^3 2E_{\chi_2}}\frac{d^3p_{\chi_3}}{(2\pi)^3 2E_{\chi_3}}(2\pi)^4\delta^4\left(p_{\chi_1}+p_{\chi_2}+p_{\chi_3}-p_0\right)\\ &\quad\times\frac{d^3p_{\chi_4}}{(2\pi)^3 2E_{\chi_4}}\frac{d^3p_{\chi_5}}{(2\pi)^3 2E_{\chi_5}}(2\pi)^4\delta^4\left(p_0-p_{\chi_4}-p_{\chi_5}\right)\frac{d^4p_0}{(2\pi)^4}e^{E_0/T}\overline{|\mathcal{M}|^2}. \qquad \text{(A.32)}\end{aligned}$$

Since we are interested in the case when the dark matter is non-relativistic, the system is approximately at rest. Therefore, to leading order, the integrals can be performed in the center of mass frame. The forms of the 3-body and 2-body space integrals are well known in this case:

$$\frac{1}{g_\chi^3}\int d\Pi_1 d\Pi_2 d\Pi_3(2\pi)^4\delta^4(p_0-p_1-p_2-p_3)=\frac{1}{(2\pi)^3}\frac{1}{16s}\int dm_{12}^2 dm_{23}^2\,, \qquad \text{(A.33)}$$

where $s=p_0^2$. The bounds of integration are

$$\begin{aligned}m_{23,max}^2 &= \frac{(s-m_\chi^2)^2}{4m_{12}^2}-\frac{m_{12}^2}{4}\left(\lambda^{1/2}(m_{12},m_\chi,m_\chi)-\lambda^{1/2}(m_{12},m_\chi,\sqrt{s})\right)^2\,,\\ m_{23,min}^2 &= \frac{(s-m_\chi^2)^2}{4m_{12}^2}-\frac{m_{12}^2}{4}\left(\lambda^{1/2}(m_{12},m_\chi,m_\chi)+\lambda^{1/2}(m_{12},m_\chi,\sqrt{s})\right)^2\,,\\ m_{12,max}^2 &= (\sqrt{s}-m_\chi)^2\,,\\ m_{12,min}^2 &= 4m_\chi^2\,, \qquad \text{(A.34)}\end{aligned}$$

where $\lambda(x,y,z) = (1-(z+y)^2/x^2)\,(1-(z-y)^2/x^2)$. The 2-body phase-space integral is

$$\frac{1}{g_\chi^2}\int d\Pi_4 d\Pi_5(2\pi)^4\delta^4(p_0-p_4-p_5)=\frac{1}{8\pi}\lambda^{1/2}(\sqrt{s},m_\chi,m_\chi). \qquad \text{(A.35)}$$

Finally, the remaining p_0 integral can be written as

$$\frac{d^4p}{(2\pi)^4}=\frac{1}{(2\pi)^3}\int_{9m_\chi^2}^\infty ds\int_{\sqrt{s}}^\infty dE_0\sqrt{E_0^2-s}\,. \qquad \text{(A.36)}$$

Putting everything together, we obtain

$$\langle \sigma_{3\to 2} v^2 \rangle = \frac{g_\chi^5}{(n_\chi^{\rm eq})^3} \frac{1}{768} \frac{1}{(2\pi)^7} \int_{9m_\chi^2}^\infty \frac{ds}{s} \sqrt{1-\frac{4m_\chi^2}{s}} \int_{\sqrt{s}}^\infty dE_0 e^{E_0/T} \sqrt{E_0^2 - s} \int dm_{12}^2 dm_{23}^2 \overline{|\mathcal{M}|^2}. \tag{A.37}$$

If the matrix element has significant dependence on kinematics even in the non-relativistic regime, the remaining integrals have to be evaluated numerically. This is the case in the Choi-Lee model of Section 2.4.2, where a resonance at $\sqrt{s} \approx 3m_\chi$ can lead to rapid change of the matrix element with s near threshold. Our analysis of that model is therefore based on numerical evaluation of Eq. (A.37). In most cases, however, the matrix element in the non-relativistic regime can be approximated as a constant, independent of kinematics. In this case, all integrals in Eq. (A.37) can be evaluated analytically. This yields

$$\langle \sigma_{3\to 2} v^2 \rangle = \frac{\sqrt{5} g_\chi^2}{2304\pi m_\chi^3} \overline{|\mathcal{M}|^2}. \tag{A.38}$$

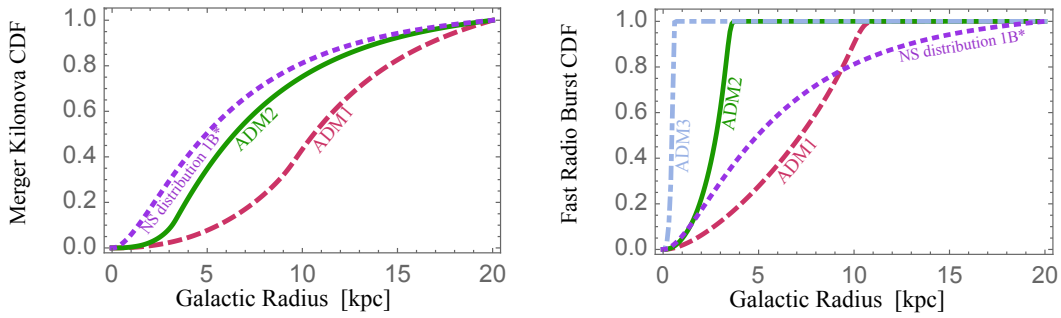

Figure B.1: Cumulative distribution functions corresponding to the Kolmogorov-Smirnov tests shown in Figures 3.3 and 3.4 are given, for merger kilonovae (left) and fast radio bursts (right). Both merger kilonovae and FRBs are assumed to follow the distribution of NSs in an MWEG (dotted purple line labeled 1B*). This distribution can be compared with distributions for representative NS-imploding dark matter models, ADM1, ADM2, and ADM3, defined by $t_c \rho_x / v_x = 3$, 15, and 100 Gyr GeV/cm^3 (200 km/s)$^{-1}$ respectively, see Eq. (2) of the main text.

APPENDIX B

DARK MATTER-INDUCED NEUTRON STAR IMPLOSIONS

B.1 Cumulative Distribution Functions

Figure B.1 shows the cumulative distribution functions used in the Kolmogorov-Smirnov tests, whose results are displayed in Figures 3.3 and 3.4. As indicated, the displayed CDFs here were generated using the neutron star distribution model 1B* in [249]. However, note that we have found that Kolmogorov-Smirnov tests utilizing other pulsar distribution models in [249] require a similar number of NS mergers to achieve sensitivity to asymmetric dark matter comparable to the results shown in Figures 3.3 and 3.4.

B.2 Dark matter-induced Neutron Star Implosion Time

The analysis of NS implosions in Section 1 assumed that the longest timescale in the NS implosion process is the time for a NS to accrete a BH-forming mass of dark matter. Here we justify this assumption by computing timescales for all dynamical processes leading up to dark matter-induced NS implosions. As an example, we consider fermionic dark matter in the PeV mass range with dark matter-nucleon cross-section $\sigma_{n\mathrm{x}} \sim 10^{-45}$ cm^2. For $\sigma_{n\mathrm{x}} \gtrsim 10^{-45}$ cm^2, all PeV mass dark matter passing through the NS will be captured [144], as assumed in Section 1. Extending this work to PeV mass bosonic dark matter requires minor modifications discussed around Eq. (3) of the main text, with similar results obtained. Similar results arises for low mass dark matter [30, 124, 126, 128, 145], where sensitivity to σ_{nx} scales inversely with $t_{\mathrm{c}}\rho_{\mathrm{x}}/v_{\mathrm{x}}$ – so that the $t_{\mathrm{c}}\rho_{\mathrm{x}}/v_{\mathrm{x}}$ reach of this study results in up to a 100-fold improvement in σ_{nx} sensitivity.

A small BH may form when a NS accumulates so much dark matter, that the dark matter cannot support its own weight with degeneracy pressure. This critical mass for fermionic dark matter is $M^{\mathrm{f}}_{\mathrm{crit}} \sim \frac{m^3_{\mathrm{pl}}}{m^2_{\mathrm{x}}}$, as reported in the main text. In principle (*e.g.* for lower mass dark matter) dark matter may accumulate to $M^{\mathrm{f}}_{\mathrm{crit}}$ size in a NS, yet not implode. This is because until dark matter in a NS "self-gravitates" or equivalently forms a bulk whose density exceeds the NS density, it will remain stable.[1] We find the self-gravitating mass M_{sg} [124] for PeV mass dark matter, and determine that $M_{\mathrm{crit}} \gg M_{\mathrm{sg}}$, which justifies our assumption in the main text, that a BH will form once M_{crit} dark matter accumulates. For the

[1] In the case of dark matter with substantial self-interactions, this computation is different [28, 126, 127].

limiting case of a younger NS with temperature $T_{\rm NS} \sim 10^5$ K,

$$M_{sg} \simeq 5 \times 10^{37}\,{\rm GeV} \left(\frac{T_{\rm NS}}{10^5\ {\rm K}}\right)^{3/2} \left(\frac{\rm PeV}{m_X}\right)^{3/2}, \tag{B.1}$$

and one can see that $M_{\rm crit}$ is at least 10^6 times larger than M_{sg} for PeV mass dark matter.

Next we review the dynamical timescales for a NS to become converted to a BH by accumulated dark matter. First the dark matter particles thermally equilibrate with the neutron star, through repeated scattering; we denote this thermalization time scale by $\tau_{\rm th}$. Once an unstable mass $M_{\rm crit}$ of dark matter has thermalized into a small volume, the dark matter will collapse, cool, and form a BH, over a time $\tau_{\rm co}$. Lastly, the small BH formed of dark matter accretes the surrounding neutron star in a time τ_{Bondi}. We will see that each process occurs much faster than the $t_c \gtrsim$ Myr time scale, and conclude that the neutron star implosion time is determined by t_c.

We first consider the thermalization. Dark matter particles captured and accumulated in the neutron star thermalize with the neutrons and cool to temperature $T \simeq 10^5$ K, same as the neutron star, before it start lose more kinetic energy and eventually collapse into a BH. The time scale τ_{th} is determined by the neutron-dark matter collisions [145], in particular

$$\tau_{\rm th} \simeq 8 \times 10^{-3}\,{\rm yr} \left(\frac{m_{\rm x}}{\rm PeV}\right) \left(\frac{10^{-45}\,{\rm cm}^2}{\sigma_{nx}}\right) \left(\frac{10^5\ {\rm K}}{T_{\rm NS}}\right)^2. \tag{B.2}$$

After thermalization, the dark matter particles form a spherical configuration of radius $r_0 \sim (9T/8\pi G\rho_c m_{\rm x})^{1/2}$, where the dark matter density at collapse is equal to the NS density $\rho_c \sim \rho_{\rm n}$. The dark matter particles can further lose more of their energy and collapse into a BH. There are several mechanisms that contribute to

this cooling, with associated time scales. Here we focus on cooling via dark matter-neutron scattering, while other cooling mechanisms can be found in *e.g.* [29]. The dark matter cooling and collapse time is approximately the time for dark matter to lose $\mathcal{O}(1)$ of its kinetic energy to surrounding neutrons,

$$\begin{aligned}\tau_{\rm co} &\simeq \frac{1}{n\sigma_{n\rm x}v_{\rm xc}}\left(\frac{p_F}{\Delta p}\right)\left(\frac{m_{\rm x}}{2m_n}\right)\\ &\simeq 4\times 10^5\ {\rm yrs}\left(\frac{m_{\rm x}}{\rm PeV}\right)\left(\frac{10^{-45}\ {\rm cm}^2}{\sigma_{\rm nx}}\right)\left(\frac{r_x}{r_0}\right),\end{aligned} \tag{B.3}$$

where n is the number density of the neutrons. The first term $1/n\sigma_{n\rm x}v_{\rm xc}$ is the time for a single collision. In addition, Pauli blocking has to be taken into account, as it reduces cross-section by a factor of $\Delta p/p_F$, hence the second term. Here $p_F \sim 0.5$ GeV is the neutron Fermi momentum in a NS and $\Delta p \sim m_n v_{\rm xc}$. The factor of $v_{\rm xc}$ here is the velocity of the dark matter sphere as it collapses through radius r_x, which can be written as $v_{\rm xc} \sim (Gm_{\rm x}/r_x)^{1/2}$. The final factor takes into account that in each collision only a fraction $\sim 2m_n/m_{\rm x}$ of the dark matter kinetic energy is transferred, so one requires $\sim \left(\frac{m_{\rm x}}{2m_n}\right)$ collisions for an order-one energy loss.

With the BH formed, assuming it accretes the remainder of the NS, the time for which depends on the BHBH mass $M_{\rm crit}$ (*e.g.* [32, 147]).

$$\tau_{\rm Bondi} \sim 0.1\ {\rm yrs}\left(\frac{m_X}{\rm PeV}\right)^2 \tag{B.4}$$

We find that $\tau_{\rm th}, \tau_{\rm co}, \tau_{\rm Bondi}$ are much shorter than $\sim t_c$, which therefore determines the time until a NS implodes.

BIBLIOGRAPHY

[1] Eric Kuflik, Maxim Perelstein, Nicolas Rey-Le Lorier, and Yu-Dai Tsai. Elastically Decoupling Dark Matter. *Phys. Rev. Lett.*, 116(22):221302, 2016.

[2] Eric Kuflik, Maxim Perelstein, Nicolas Rey-Le Lorier, and Yu-Dai Tsai. Phenomenology of ELDER Dark Matter. *JHEP*, 08:078, 2017.

[3] Joseph Bramante, Tim Linden, and Yu-Dai Tsai. Searching for dark matter with neutron star mergers and quiet kilonovae. *Phys. Rev.*, D97(5):055016, 2018.

[4] Maxim Pospelov and Yu-Dai Tsai. Probing Light Bosons in the Borexino-SOX Experiment. 2017.

[5] Gabriel Magill, Ryan Plestid, Maxim Pospelov, and Yu-Dai Tsai. Dipole portal to heavy neutral leptons. 2018.

[6] Gabriel Magill, Ryan Plestid, Maxim Pospelov, and Yu-Dai Tsai. Millicharged particles in neutrino experiments. 2018.

[7] Maxim Perelstein and Yu-Dai Tsai. 750 GeV diphoton excess and strongly first-order electroweak phase transition. *Phys. Rev.*, D94(1):015033, 2016.

[8] Jens Braun, Jiunn-Wei Chen, Jian Deng, Joaquin E. Drut, Bengt Friman, Chen-Te Ma, and Yu-Dai Tsai. Imaginary polarization as a way to surmount the sign problem in *Ab Initio* calculations of spin-imbalanced Fermi gases. *Phys. Rev. Lett.*, 110:130404, 2013.

[9] Yu-Dai Tsai, Hsiang-nan Li, and Qiang Zhao. η_c mixing effects on charmonium and B meson decays. *Phys. Rev.*, D85:034002, 2012.

[10] Yu-Dai Tsai, X. N. Wu, and Yi Yang. Phase Structure of Kerr-AdS Black Hole. *Phys. Rev.*, D85:044005, 2012.

[11] Edvige Corbelli and Paolo Salucci. The Extended Rotation Curve and the Dark Matter Halo of M33. *Mon. Not. Roy. Astron. Soc.*, 311:441–447, 2000.

[12] S. M. Faber and R. E. Jackson. Velocity dispersions and mass to light ratios for elliptical galaxies. *Astrophys. J.*, 204:668, 1976.

[13] A. N. Taylor, S. Dye, Thomas J. Broadhurst, N. Benitez, and E. van Kampen. Gravitational lens magnification and the mass of abell 1689. *Astrophys. J.*, 501:539, 1998.

[14] Alexandre Refregier. Weak gravitational lensing by large scale structure. *Ann. Rev. Astron. Astrophys.*, 41:645–668, 2003.

[15] Maxim Markevitch, A. H. Gonzalez, D. Clowe, A. Vikhlinin, L. David, W. Forman, C. Jones, S. Murray, and W. Tucker. Direct constraints on the dark matter self-interaction cross-section from the merging galaxy cluster 1E0657-56. *Astrophys. J.*, 606:819–824, 2004.

[16] Stefano Profumo. *An Introduction to Particle Dark Matter*. World Scientific, 2017.

[17] Gerard Jungman, Marc Kamionkowski, and Kim Griest. Supersymmetric dark matter. *Phys. Rept.*, 267:195–373, 1996.

[18] Eric D. Carlson, Marie E. Machacek, and Lawrence J. Hall. Self-interacting dark matter. *Astrophys. J.*, 398:43–52, 1992.

[19] David N. Spergel and Paul J. Steinhardt. Observational evidence for selfinteracting cold dark matter. *Phys. Rev. Lett.*, 84:3760–3763, 2000.

[20] Yonit Hochberg, Eric Kuflik, Hitoshi Murayama, Tomer Volansky, and Jay G. Wacker. Model for Thermal Relic Dark Matter of Strongly Interacting Massive Particles. *Phys. Rev. Lett.*, 115(2):021301, 2015.

[21] J. Rich, R. Rocchia, and M. Spiro. A search for strongly interacting dark matter. *Physics Letters B*, 194:173–176, July 1987.

[22] Andrew A. de Laix, Robert J. Scherrer, and Robert K. Schaefer. Constraints of self interacting dark matter. *Astrophys. J.*, 452:495, 1995.

[23] B. Moore. Evidence against dissipationless dark matter from observations of galaxy haloes. *Nature*, 370:629, 1994.

[24] Wikipedia. `https://en.wikipedia.org/wiki/Strongly_interacting_massive_particle`.

[25] Glenn D. Starkman, Andrew Gould, Rahim Esmailzadeh, and Savas Di-

mopoulos. Opening the Window on Strongly Interacting Dark Matter. *Phys. Rev.*, D41:3594, 1990.

[26] Yonit Hochberg, Matt Pyle, Yue Zhao, and Kathryn M. Zurek. Detecting Superlight Dark Matter with Fermi-Degenerate Materials. 2015.

[27] Joseph Bramante and Tim Linden. Detecting Dark Matter with Imploding Pulsars in the Galactic Center. *Phys. Rev. Lett.*, 113(19):191301, 2014.

[28] Joseph Bramante and Fatemeh Elahi. Higgs portals to pulsar collapse. *Phys. Rev.*, D91(11):115001, 2015.

[29] I. Goldman and S. Nussinov. Weakly Interacting Massive Particles and Neutron Stars. *Phys. Rev.*, D40:3221–3230, 1989.

[30] Arnaud de Lavallaz and Malcolm Fairbairn. Neutron Stars as Dark Matter Probes. *Phys. Rev.*, D81:123521, 2010.

[31] Chris Kouvaris and Peter Tinyakov. Constraining Asymmetric Dark Matter through observations of compact stars. *Phys. Rev.*, D83:083512, 2011.

[32] Joseph Bramante and Tim Linden. On the r-Process Enrichment of Dwarf Spheroidal Galaxies. *Astrophys. J.*, 826(1):57, 2016.

[33] Jim Fuller and Christian Ott. Dark Matter-induced Collapse of Neutron Stars: A Possible Link Between Fast Radio Bursts and the Missing Pulsar Problem. *Mon. Not. Roy. Astron. Soc.*, 450(1):L71–L75, 2015.

[34] Benjamin P. Abbott et al. Upper Limits on the Rates of Binary Neutron Star and Neutron Star - Black Hole Mergers From Advanced Ligo's First Observing Run. *Astrophys. J.*, 832(2):L21, 2016.

[35] Z. Doctor et al. A Search for Kilonovae in the Dark Energy Survey. *Astrophys. J.*, 837(1):57, 2017.

[36] M. Soares-Santos et al. A Dark Energy Camera Search for an Optical Counterpart to the First Advanced LIGO Gravitational Wave Event GW150914. *Astrophys. J.*, 823(2):L33, 2016.

[37] Shaon Ghosh and Gijs Nelemans. Localizing gravitational wave sources with optical telescopes and combining electromagnetic and gravitational wave data. *Astrophys. Space Sci. Proc.*, 40:51–58, 2015.

[38] E. Bellm and S. Kulkarni. The unblinking eye on the sky. *Nature Astronomy*, 1:0071, March 2017.

[39] Philippe Berger et al. Holographic Beam Mapping of the CHIME Pathfinder Array. *Proc. SPIE Int. Soc. Opt. Eng.*, 9906:99060D, 2016.

[40] L. B. Newburgh et al. HIRAX: A Probe of Dark Energy and Radio Transients. *Proc. SPIE Int. Soc. Opt. Eng.*, 9906:99065X, 2016.

[41] G. W. Bennett et al. Final Report of the Muon E821 Anomalous Magnetic Moment Measurement at BNL. *Phys. Rev.*, D73:072003, 2006.

[42] *Fundamental Physics at the Intensity Frontier*, 2012.

[43] Vanda Silveira and A. Zee. SCALAR PHANTOMS. *Phys. Lett.*, B161:136–140, 1985.

[44] Bob Holdom. Two U(1)'s and Epsilon Charge Shifts. *Phys. Lett.*, 166B:196–198, 1986.

[45] C. Boehm and Pierre Fayet. Scalar dark matter candidates. *Nucl. Phys.*, B683:219–263, 2004.

[46] Alexey Boyarsky, Oleg Ruchayskiy, and Mikhail Shaposhnikov. The Role of sterile neutrinos in cosmology and astrophysics. *Ann. Rev. Nucl. Part. Sci.*, 59:191–214, 2009.

[47] Maxim Pospelov, Adam Ritz, and Mikhail B. Voloshin. Secluded WIMP Dark Matter. *Phys. Lett.*, B662:53–61, 2008.

[48] Sergei N. Gninenko. A resolution of puzzles from the LSND, KARMEN, and MiniBooNE experiments. *Phys. Rev.*, D83:015015, 2011.

[49] Asimina Arvanitaki, Savas Dimopoulos, Sergei Dubovsky, Nemanja Kaloper, and John March-Russell. String Axiverse. *Phys. Rev.*, D81:123530, 2010.

[50] Nima Arkani-Hamed, Douglas P. Finkbeiner, Tracy R. Slatyer, and Neal Weiner. A Theory of Dark Matter. *Phys. Rev.*, D79:015014, 2009.

[51] Joerg Jaeckel and Andreas Ringwald. The Low-Energy Frontier of Particle Physics. *Ann. Rev. Nucl. Part. Sci.*, 60:405–437, 2010.

[52] Jim Alexander et al. Dark Sectors 2016 Workshop: Community Report. 2016.

[53] A. Gando et al. Search for Majorana Neutrinos near the Inverted Mass Hierarchy Region with KamLAND-Zen. *Phys. Rev. Lett.*, 117(8):082503, 2016. [Addendum: Phys. Rev. Lett.117,no.10,109903(2016)].

[54] S. Andringa et al. Current Status and Future Prospects of the SNO+ Experiment. *Adv. High Energy Phys.*, 2016:6194250, 2016.

[55] G. Bellini et al. SOX: Short distance neutrino Oscillations with BoreXino. *JHEP*, 08:038, 2013.

[56] Carlo Gustavino. Neutrinos and Nuclear Astrophysics at LUNA. *Nucl. Part. Phys. Proc.*, 273-275:1807–1813, 2016.

[57] M. Nakahata et al. Calibration of Super-Kamiokande using an electron linac. *Nucl. Instrum. Meth.*, A421:113–129, 1999.

[58] C. Aberle et al. Whitepaper on the DAEdALUS Program. In *Proceedings, Community Summer Study 2013: Snowmass on the Mississippi (CSS2013): Minneapolis, MN, USA, July 29-August 6, 2013*, 2013.

[59] M. Abs et al. IsoDAR@KamLAND: A Conceptual Design Report for the Technical Facility. 2015.

[60] Eder Izaguirre, Gordan Krnjaic, and Maxim Pospelov. Probing New Physics with Underground Accelerators and Radioactive Sources. *Phys. Lett.*, B740:61–65, 2015.

[61] Yonatan Kahn, Gordan Krnjaic, Jesse Thaler, and Matthew Toups. DAEdALUS and dark matter detection. *Phys. Rev.*, D91(5):055006, 2015.

[62] Eder Izaguirre, Gordan Krnjaic, and Maxim Pospelov. MeV-Scale Dark Matter Deep Underground. *Phys. Rev.*, D92(9):095014, 2015.

[63] C. Athanassopoulos et al. Evidence for anti-muon-neutrino —> anti-electron-neutrino oscillations from the LSND experiment at LAMPF. *Phys. Rev. Lett.*, 77:3082–3085, 1996.

[64] A. A. Aguilar-Arevalo et al. A Search for electron neutrino appearance at the $\Delta m^2 \sim 1\mathrm{eV}^2$ scale. *Phys. Rev. Lett.*, 98:231801, 2007.

[65] A. A. Aguilar-Arevalo et al. Observation of a Significant Excess of Electron-Like Events in the MiniBooNE Short-Baseline Neutrino Experiment. 2018.

[66] M. I. Dobroliubov and A. Yu. Ignatiev. MILLICHARGED PARTICLES. *Phys. Rev. Lett.*, 65:679–682, 1990.

[67] David E. Brahm and Lawrence J. Hall. U(1)-prime DARK MATTER. *Phys. Rev.*, D41:1067, 1990.

[68] Nicolas Bernal, Camilo García-Cely, and Rogerio Rosenfeld. WIMP and Simp Dark Matter from the Spontaneous Breaking of a Global Group. *JCAP*, 1504(04):012, 2015.

[69] Hyun Min Lee and Min-Seok Seo. Communication with Simp Dark Mesons via Z' -Portal. *Phys. Lett.*, B748:316–322, 2015.

[70] Nicolas Bernal, Xiaoyong Chu, Camilo García-Cely, Thomas Hambye, and Bryan Zaldivar. Production Regimes for Self-Interacting Dark Matter. 2015.

[71] Nicolas Bernal and Xiaoyong Chu. Z_2 Simp Dark Matter. *JCAP*, 1601:006, 2016.

[72] Yonit Hochberg, Eric Kuflik, and Hitoshi Murayama. Simp Spectroscopy. *JHEP*, 05:090, 2016.

[73] Soo-Min Choi and Hyun Min Lee. Resonant Simp Dark Matter. 2016.

[74] Duccio Pappadopulo, Joshua T. Ruderman, and Gabriele Trevisan. Cannibal Dark Matter. 2016.

[75] Marco Farina, Duccio Pappadopulo, Joshua T. Ruderman, and Gabriele Trevisan. Phases of Cannibal Dark Matter. 2016.

[76] Lindsay Forestell, David E. Morrissey, and Kris Sigurdson. Non-Abelian Dark Forces and the Relic Densities of Dark Glueballs. 2016.

[77] Amarjit Soni and Yue Zhang. Hidden $SU(N)$ Glueball Dark Matter. *Phys. Rev.*, D93(11):115025, 2016.

[78] Soo-Min Choi, Yoo-Jin Kang, and Hyun Min Lee. On Thermal Production of Self-Interacting Dark Matter. *JHEP*, 12:099, 2016.

[79] James Cline, Hongwan Liu, Tracy Slatyer, and Wei Xue. Enabling Forbidden Dark Matter. 2017.

[80] Soo-Min Choi, Hyun Min Lee, and Min-Seok Seo. Cosmic Abundances of Simp Dark Matter. *JHEP*, 04:154, 2017.

[81] Nicolás Bernal, Xiaoyong Chu, and Josef Pradler. Simply Split Simps. 2017.

[82] Ujjal Kumar Dey, Tarak Nath Maity, and Tirtha Sankar Ray. Light Dark Matter through Assisted Annihilation. *JCAP*, 1703(03):045, 2017.

[83] Yonit Hochberg, Eric Kuflik, Tomer Volansky, and Jay G. Wacker. Mechanism for Thermal Relic Dark Matter of Strongly Interacting Massive Particles. *Phys. Rev. Lett.*, 113:171301, 2014.

[84] Robert Foot, H. Lew, and R. R. Volkas. A Model with Fundamental Improper Space-Time Symmetries. *Phys. Lett.*, B272:67–70, 1991.

[85] Robert Foot, H. Lew, and R. R. Volkas. Possible Consequences of Parity Conservation. *Mod. Phys. Lett.*, A7:2567–2574, 1992.

[86] Z. G. Berezhiani, A. D. Dolgov, and R. N. Mohapatra. Asymmetric Inflationary Reheating and the Nature of Mirror Universe. *Phys. Lett.*, B375:26–36, 1996.

[87] Z. Chacko, Hock-Seng Goh, and Roni Harnik. The Twin Higgs: Natural Electroweak Breaking from Mirror Symmetry. *Phys. Rev. Lett.*, 96:231802, 2006.

[88] Gustavo Burdman, Z. Chacko, Hock-Seng Goh, and Roni Harnik. Folded Supersymmetry and the Lep Paradox. *JHEP*, 02:009, 2007.

[89] Kim Griest and Marc Kamionkowski. Unitarity Limits on the Mass and Radius of Dark Matter Particles. *Phys. Rev. Lett.*, 64:615, 1990.

[90] Céline Boehm, Matthew J. Dolan, and Christopher McCabe. A Lower Bound on the Mass of Cold Thermal Dark Matter from Planck. *JCAP*, 1308:041, 2013.

[91] Jonathan L. Feng and Jason Kumar. The Wimpless Miracle: Dark-Matter Particles without Weak-Scale Masses Or Weak Interactions. *Phys. Rev. Lett.*, 101:231301, 2008.

[92] Eder Izaguirre, Gordan Krnjaic, Philip Schuster, and Natalia Toro. Analyzing the Discovery Potential for Light Dark Matter. *Phys. Rev. Lett.*, 115(25):251301, 2015.

[93] Douglas P. Finkbeiner, Silvia Galli, Tongyan Lin, and Tracy R. Slatyer. Searching for Dark Matter in the Cmb: a Compact Parameterization of Energy Injection from New Physics. *Phys. Rev.*, D85:043522, 2012.

[94] Mathew S. Madhavacheril, Neelima Sehgal, and Tracy R. Slatyer. Current Dark Matter Annihilation Constraints from Cmb and Low-Redshift Data. *Phys. Rev.*, D89:103508, 2014.

[95] Tracy R. Slatyer. Indirect Dark Matter Signatures in the Cosmic Dark Ages I. Generalizing the Bound on S-Wave Dark Matter Annihilation from Planck. 2015.

[96] Jae Hyeok Chang, Rouven Essig, and Samuel D. McDermott. Revisiting Supernova 1987A Constraints on Dark Photons. *JHEP*, 01:107, 2017.

[97] Edward Hardy and Robert Lasenby. Stellar cooling bounds on new light particles: plasma mixing effects. *JHEP*, 02:033, 2017.

[98] Rouven Essig, Aaron Manalaysay, Jeremy Mardon, Peter Sorensen, and Tomer Volansky. First Direct Detection Limits on Sub-Gev Dark Matter from Xenon10. *Phys. Rev. Lett.*, 109:021301, 2012.

[99] Rouven Essig, Tomer Volansky, and Tien-Tien Yu. New Constraints and Prospects for Sub-Gev Dark Matter Scattering Off Electrons in Xenon. 2017.

[100] Rouven Essig, Jeremy Mardon, and Tomer Volansky. Direct Detection of Sub-Gev Dark Matter. *Phys. Rev.*, D85:076007, 2012.

[101] Peter W. Graham, David E. Kaplan, Surjeet Rajendran, and Matthew T. Walters. Semiconductor Probes of Light Dark Matter. *Phys. Dark Univ.*, 1:32–49, 2012.

[102] Rouven Essig, Marivi Fernandez-Serra, Jeremy Mardon, Adrian Soto, Tomer Volansky, and Tien-Tien Yu. Direct Detection of Sub-Gev Dark Matter with Semiconductor Targets. 2015.

[103] Javier Tiffenberg, Miguel Sofo-Haro, Alex Drlica-Wagner, Rouven Essig, Yann Guardincerri, Steve Holland, Tomer Volansky, and Tien-Tien Yu.

Single-Electron and Single-Photon Sensitivity with a Silicon Skipper Ccd. 2017.

[104] Yonit Hochberg, Yue Zhao, and Kathryn M. Zurek. Superconducting Detectors for Superlight Dark Matter. *Phys. Rev. Lett.*, 116(1):011301, 2016.

[105] Katelin Schutz and Kathryn M. Zurek. On the Detectability of Light Dark Matter with Superfluid Helium. *Phys. Rev. Lett.*, 117:121302, 2016.

[106] Simon Knapen, Tongyan Lin, and Kathryn M. Zurek. Light Dark Matter in Superfluid Helium: Detection with Multi-Excitation Production. *Phys. Rev.*, D95(5):056019, 2017.

[107] Stephen Derenzo, Rouven Essig, Andrea Massari, Adrían Soto, and Tien-Tien Yu. Direct Detection of Sub-Gev Dark Matter with Scintillating Targets. 2016.

[108] Yonit Hochberg, Yonatan Kahn, Mariangela Lisanti, Christopher G. Tully, and Kathryn M. Zurek. Directional Detection of Dark Matter with 2D Targets. 2016.

[109] J. P. Lees et al. Search for Invisible Decays of a Dark Photon Produced in e^+e^- Collisions at BaBar. *Phys. Rev. Lett.*, 119(13):131804, 2017.

[110] D. Banerjee et al. Search for invisible decays of sub-GeV dark photons in missing-energy events at the CERN SPS. *Phys. Rev. Lett.*, 118(1):011802, 2017.

[111] Eder Izaguirre, Gordan Krnjaic, Philip Schuster, and Natalia Toro. Testing GeV-Scale Dark Matter with Fixed-Target Missing Momentum Experiments. *Phys. Rev.*, D91(9):094026, 2015.

[112] A. A. Aguilar-Arevalo et al. Dark Matter Search in a Proton Beam Dump with MiniBooNE. *Phys. Rev. Lett.*, 118(22):221803, 2017.

[113] M. Battaglieri et al. Dark matter search in a Beam-Dump eXperiment (BDX) at Jefferson Lab. 2014.

[114] Sergey Alekhin et al. A facility to Search for Hidden Particles at the CERN SPS: the SHiP physics case. *Rept. Prog. Phys.*, 79(12):124201, 2016.

[115] Soo-Min Choi and Hyun Min Lee. Simp Dark Matter with Gauged Z_3 Symmetry. *JHEP*, 09:063, 2015.

[116] Douglas Clowe, Anthony Gonzalez, and Maxim Markevitch. Weak Lensing Mass Reconstruction of the Interacting Cluster 1E0657-558: Direct Evidence for the Existence of Dark Matter. *Astrophys. J.*, 604:596–603, 2004.

[117] Scott W. Randall, Maxim Markevitch, Douglas Clowe, Anthony H. Gonzalez, and Marusa Bradac. Constraints on the Self-Interaction Cross-Section of Dark Matter from Numerical Simulations of the Merging Galaxy Cluster 1E 0657-56. *Astrophys. J.*, 679:1173–1180, 2008.

[118] Miguel Rocha, Annika H. G. Peter, James S. Bullock, Manoj Kaplinghat, Shea Garrison-Kimmel, Jose Onorbe, and Leonidas A. Moustakas. Cosmological Simulations with Self-Interacting Dark Matter I: Constant Density Cores and Substructure. *Mon. Not. Roy. Astron. Soc.*, 430:81–104, 2013.

[119] Jesus Zavala, Mark Vogelsberger, and Matthew G. Walker. Constraining Self-Interacting Dark Matter with the Milky Way's Dwarf Spheroidals. *Monthly Notices of the Royal Astronomical Society: Letters*, 431:L20–L24, 2013.

[120] Annika H. G. Peter, Miguel Rocha, James S. Bullock, and Manoj Kaplinghat. Cosmological Simulations with Self-Interacting Dark Matter Ii: Halo Shapes Vs. Observations. *Mon. Not. Roy. Astron. Soc.*, 430:105, 2013.

[121] P. A. R. Ade et al. Planck 2015 results. XIII. Cosmological parameters. *Astron. Astrophys.*, 594:A13, 2016.

[122] Masha Baryakhtar, Joseph Bramante, Shirley Weishi Li, Tim Linden, and Nirmal Raj. Dark Kinetic Heating of Neutron Stars and An Infrared Window On WIMPs, SIMPs, and Pure Higgsinos. 2017.

[123] Samuel D. McDermott, Hai-Bo Yu, and Kathryn M. Zurek. Constraints on Scalar Asymmetric Dark Matter from Black Hole Formation in Neutron Stars. *Phys. Rev.*, D85:023519, 2012.

[124] Joseph Bramante, Keita Fukushima, and Jason Kumar. Constraints on bosonic dark matter from observation of old neutron stars. *Phys. Rev.*, D87(5):055012, 2013.

[125] Nicole F. Bell, Andrew Melatos, and Kalliopi Petraki. Realistic neutron star

constraints on bosonic asymmetric dark matter. *Phys. Rev.*, D87(12):123507, 2013.

[126] Chris Kouvaris. Limits on Self-Interacting Dark Matter. *Phys. Rev. Lett.*, 108:191301, 2012.

[127] Joseph Bramante, Keita Fukushima, Jason Kumar, and Elan Stopnitzky. Bounds on self-interacting fermion dark matter from observations of old neutron stars. *Phys. Rev.*, D89(1):015010, 2014.

[128] Joseph Bramante. Dark matter ignition of type Ia supernovae. *Phys. Rev. Lett.*, 115(14):141301, 2015.

[129] M. Colpi, S. L. Shapiro, and I. Wasserman. Boson Stars: Gravitational Equilibria of Selfinteracting Scalar Fields. *Phys. Rev. Lett.*, 57:2485–2488, 1986.

[130] J. Abadie et al. Predictions for the Rates of Compact Binary Coalescences Observable by Ground-based Gravitational-wave Detectors. *Class. Quant. Grav.*, 27:173001, 2010.

[131] Andrew M. Hopkins and John F. Beacom. On the normalisation of the cosmic star formation history. *Astrophys. J.*, 651:142–154, 2006.

[132] Julio F. Navarro, Carlos S. Frenk, and Simon D. M. White. A Universal density profile from hierarchical clustering. *Astrophys. J.*, 490:493–508, 1997.

[133] Yoshiaki Sofue. Rotation Curve and Mass Distribution in the Galactic Center — From Black Hole to Entire Galaxy —. *Publ. Astron. Soc. Jap.*, 65:118, 2013.

[134] S. W. Hawking. Black hole explosions. *Nature*, 248:30–31, 1974.

[135] Bernard J. Carr and S. W. Hawking. Black holes in the early Universe. *Mon. Not. Roy. Astron. Soc.*, 168:399–415, 1974.

[136] Fabio Capela, Maxim Pshirkov, and Peter Tinyakov. Constraints on primordial black holes as dark matter candidates from capture by neutron stars. *Phys. Rev.*, D87(12):123524, 2013.

[137] Fabio Capela, Maxim Pshirkov, and Peter Tinyakov. Constraints on Pri-

mordial Black Holes as Dark Matter Candidates from Star Formation. *Phys. Rev.*, D87(2):023507, 2013.

[138] George M. Fuller, Alexander Kusenko, and Volodymyr Takhistov. Primordial Black Holes and r-Process Nucleosynthesis. 2017.

[139] Daniel Kasen, N. R. Badnell, and Jennifer Barnes. Opacities and Spectra of the r-process Ejecta from Neutron Star Mergers. *Astrophys. J.*, 774:25, 2013.

[140] E. Aprile et al. First Dark Matter Search Results from the XENON1T Experiment. *Phys. Rev. Lett.*, 119(18):181301, 2017.

[141] F. Ruppin, J. Billard, E. Figueroa-Feliciano, and L. Strigari. Complementarity of dark matter detectors in light of the neutrino background. *Phys. Rev.*, D90(8):083510, 2014.

[142] B. P. Abbott et al. Multi-messenger Observations of a Binary Neutron Star Merger. *Astrophys. J.*, 848(2):L12, 2017.

[143] P. K. Blanchard et al. The Electromagnetic Counterpart of the Binary Neutron Star Merger LIGO/VIRGO GW170817. VII. Properties of the Host Galaxy and Constraints on the Merger Timescale. *Astrophys. J.*, 848(2):L22, 2017.

[144] Joseph Bramante, Antonio Delgado, and Adam Martin. Multiscatter stellar capture of dark matter. *Phys. Rev.*, D96(6):063002, 2017.

[145] Bridget Bertoni, Ann E. Nelson, and Sanjay Reddy. Dark Matter Thermalization in Neutron Stars. *Phys. Rev.*, D88:123505, 2013.

[146] Tolga Guver, Arif Emre Erkoca, Mary Hall Reno, and Ina Sarcevic. On the capture of dark matter by neutron stars. *JCAP*, 1405:013, 2014.

[147] Chris Kouvaris and Peter Tinyakov. Growth of Black Holes in the interior of Rotating Neutron Stars. *Phys. Rev.*, D90(4):043512, 2014.

[148] Yasunari Kurita and Hiroyuki Nakano. Gravitational waves from dark matter collapse in a star. *Phys. Rev.*, D93(2):023508, 2016.

[149] A. Rane, D. R. Lorimer, S. D. Bates, N. McMann, M. A. McLaughlin, and K. Rajwade. A search for rotating radio transients and fast radio bursts

in the Parkes high-latitude pulsar survey. *Mon. Not. Roy. Astron. Soc.*, 455(2):2207–2215, 2016.

[150] Scott Vander Wiel, Sarah Burke-Spolaor, Earl Lawrence, Casey J. Law, and Geoffrey C. Bower. Rare Event Statistics Applied to Fast Radio Bursts. 2016.

[151] D. R. Lorimer, M. Bailes, M. A. McLaughlin, D. J. Narkevic, and F. Crawford. A bright millisecond radio burst of extragalactic origin. *Science*, 318:777, 2007.

[152] D. Thornton et al. A Population of Fast Radio Bursts at Cosmological Distances. *Science*, 341(6141):53–56, 2013.

[153] Carlos Palenzuela. Modeling magnetized neutron stars using resistive MHD. *Mon. Not. Roy. Astron. Soc.*, 431:1853–1865, 2013.

[154] Kyriaki Dionysopoulou, Daniela Alic, Carlos Palenzuela, Luciano Rezzolla, and Bruno Giacomazzo. General-Relativistic Resistive Magnetohydrodynamics in three dimensions: formulation and tests. *Phys. Rev.*, D88:044020, 2013.

[155] Heino Falcke and Luciano Rezzolla. Fast radio bursts: the last sign of supramassive neutron stars. *Astron. Astrophys.*, 562:A137, 2014.

[156] Luca Baiotti, Ian Hawke, and Luciano Rezzolla. On the Gravitational radiation from the collapse of neutron stars to rotating black holes. *Class. Quant. Grav.*, 24:S187–S206, 2007.

[157] B. P. Abbott et al. Prospects for Observing and Localizing Gravitational-Wave Transients with Advanced LIGO and Advanced Virgo. 2013. [Living Rev. Rel.19,1(2016)].

[158] Gian F. Giudice, Matthew McCullough, and Alfredo Urbano. Hunting for Dark Particles with Gravitational Waves. *JCAP*, 1610(10):001, 2016.

[159] A. Aguilar-Arevalo et al. Evidence for neutrino oscillations from the observation of anti-neutrino(electron) appearance in a anti-neutrino(muon) beam. *Phys. Rev.*, D64:112007, 2001.

[160] A. A. Aguilar-Arevalo et al. Improved Search for $\bar{\nu}_\mu \to \bar{\nu}_e$ Oscillations in the MiniBooNE Experiment. *Phys. Rev. Lett.*, 110:161801, 2013.

[161] J. M. Conrad and M. H. Shaevitz. Sterile Neutrinos: An Introduction to Experiments. 2016.

[162] Randolf Pohl et al. The size of the proton. *Nature*, 466:213–216, 2010.

[163] Randolf Pohl, Ronald Gilman, Gerald A. Miller, and Krzysztof Pachucki. Muonic hydrogen and the proton radius puzzle. *Ann. Rev. Nucl. Part. Sci.*, 63:175–204, 2013.

[164] David Tucker-Smith and Itay Yavin. Muonic hydrogen and MeV forces. *Phys. Rev.*, D83:101702, 2011.

[165] Chien-Yi Chen, Hooman Davoudiasl, William J. Marciano, and Cen Zhang. Implications of a light dark Higgs solution to the g-2 discrepancy. *Phys. Rev.*, D93(3):035006, 2016.

[166] Brian Batell, Nicholas Lange, David McKeen, Maxim Pospelov, and Adam Ritz. The Leptonic Higgs Portal. 2016.

[167] Vernon Barger, Cheng-Wei Chiang, Wai-Yee Keung, and Danny Marfatia. Proton size anomaly. *Phys. Rev. Lett.*, 106:153001, 2011.

[168] Brian Batell, David McKeen, and Maxim Pospelov. New Parity-Violating Muonic Forces and the Proton Charge Radius. *Phys. Rev. Lett.*, 107:011803, 2011.

[169] Savely G. Karshenboim, David McKeen, and Maxim Pospelov. Constraints on muon-specific dark forces. *Phys. Rev.*, D90(7):073004, 2014. [Addendum: Phys. Rev.D90,no.7,079905(2014)].

[170] Yu-Sheng Liu, David McKeen, and Gerald A. Miller. Electrophobic Scalar Boson and Muonic Puzzles. *Phys. Rev. Lett.*, 117(10):101801, 2016.

[171] Randolf Pohl et al. Laser spectroscopy of muonic deuterium. *Science*, 353(6300):669–673, 2016.

[172] Riccardo Barbieri and Torleif Erik Oskar Ericson. Evidence Against the Existence of a Low Mass Scalar Boson from Neutron-Nucleus Scattering. *Phys. Lett.*, 57B:270–272, 1975.

[173] Abdelhak Djouadi. The Anatomy of electro-weak symmetry breaking. I: The Higgs boson in the standard model. *Phys. Rept.*, 457:1–216, 2008.

[174] G. Bellini et al. New limits on heavy sterile neutrino mixing in B8 decay obtained with the Borexino detector. *Phys. Rev.*, D88(7):072010, 2013.

[175] P. Vogel and John F. Beacom. Angular distribution of neutron inverse beta decay, anti-neutrino(e) + p —> e+ + n. *Phys. Rev.*, D60:053003, 1999.

[176] L. B. Auerbach et al. Measurement of electron - neutrino - electron elastic scattering. *Phys. Rev.*, D63:112001, 2001.

[177] Jose Enrique Amaro, A. M. Lallena, and J. Nieves. Radiative pion capture in nuclei: A Continuum shell model approach. *Nucl. Phys.*, A623:529–547, 1997.

[178] C. Athanassopoulos et al. The Liquid scintillator neutrino detector and LAMPF neutrino source. *Nucl. Instrum. Meth.*, A388:149–172, 1997.

[179] Georg Raffelt and Achim Weiss. Red giant bound on the axion - electron coupling revisited. *Phys. Rev.*, D51:1495–1498, 1995.

[180] O. Yu. Smirnov et al. Measurement of neutrino flux from the primary proton–proton fusion process in the Sun with Borexino detector. *Phys. Part. Nucl.*, 47(6):995–1002, 2016.

[181] Kenneth M. Nollett and Gary Steigman. BBN And The CMB Constrain Light, Electromagnetically Coupled WIMPs. *Phys. Rev.*, D89(8):083508, 2014.

[182] Maxim Pospelov, Adam Ritz, and Mikhail B. Voloshin. Bosonic super-WIMPs as keV-scale dark matter. *Phys. Rev.*, D78:115012, 2008.

[183] Samuel D. McDermott, Hiren H. Patel, and Harikrishnan Ramani. Dark Photon Decay Beyond The Euler-Heisenberg Limit. 2017.

[184] Adam Burrows, M. Ted Ressell, and Michael S. Turner. Axions and SN1987A: Axion trapping. *Phys. Rev.*, D42:3297–3309, 1990.

[185] Wolfgang Keil, H. Thomas Janka, and Georg Raffelt. Reduced neutrino opacities and the SN1987A signal. *Phys. Rev.*, D51:6635–6646, 1995.

[186] Takehiko Asaka and Mikhail Shaposhnikov. The nuMSM, dark matter and baryon asymmetry of the universe. *Phys. Lett.*, B620:17–26, 2005.

[187] Dmitry Gorbunov and Mikhail Shaposhnikov. How to find neutral leptons of the νMSM? *JHEP*, 10:015, 2007. [Erratum: JHEP11,101(2013)].

[188] S. N. Gninenko. The MiniBooNE anomaly and heavy neutrino decay. *Phys. Rev. Lett.*, 103:241802, 2009.

[189] David McKeen and Maxim Pospelov. Muon Capture Constraints on Sterile Neutrino Properties. *Phys. Rev.*, D82:113018, 2010.

[190] Manuel Masip, Pere Masjuan, and Davide Meloni. Heavy neutrino decays at MiniBooNE. *JHEP*, 01:106, 2013.

[191] Manuel Masip and Pere Masjuan. Heavy-neutrino decays at neutrino telescopes. *Phys. Rev.*, D83:091301, 2011.

[192] S. N. Gninenko. New limits on radiative sterile neutrino decays from a search for single photons in neutrino interactions. *Phys. Lett.*, B710:86–90, 2012.

[193] Carlo Giunti and Alexander Studenikin. Neutrino electromagnetic interactions: a window to new physics. *Rev. Mod. Phys.*, 87:531, 2015.

[194] Alberto Aparici, Kyungwook Kim, Arcadi Santamaria, and Jose Wudka. Right-handed neutrino magnetic moments. *Phys. Rev.*, D80:013010, 2009.

[195] Alberto Aparici. *Exotic properties of neutrinos using effective Lagrangians and specific models.* PhD thesis, Valencia U., 2013.

[196] A. Caputo, P. Hernandez, J. Lopez-Pavon, and J. Salvado. The seesaw portal in testable models of neutrino masses. *JHEP*, 06:112, 2017.

[197] Pilar Coloma, Pedro A. N. Machado, Ivan Martinez-Soler, and Ian M. Shoemaker. Double-Cascade Events from New Physics in Icecube. *Phys. Rev. Lett.*, 119(20):201804, 2017.

[198] Kevork N. Abazajian. Sterile neutrinos in cosmology. *Phys. Rept.*, 711-712:1–28, 2017.

[199] Richard J. Hill. On the single photon background to ν_e appearance at MiniBooNE. *Phys. Rev.*, D84:017501, 2011.

[200] K. N. Abazajian et al. Light Sterile Neutrinos: A White Paper. 2012.

[201] F. Couchot, S. Henrot-Versillé, O. Perdereau, S. Plaszczynski, B. Rouillé D'Orfeuil, M. Spinelli, and M. Tristram. Cosmological constraints on the neutrino mass including systematic uncertainties. *Astron. Astrophys.*, 2017. [Astron. Astrophys.606,A104(2017)].

[202] Basudeb Dasgupta and Joachim Kopp. Cosmologically Safe eV-Scale Sterile Neutrinos and Improved Dark Matter Structure. *Phys. Rev. Lett.*, 112(3):031803, 2014.

[203] Steen Hannestad, Rasmus Sloth Hansen, and Thomas Tram. How Self-Interactions can Reconcile Sterile Neutrinos with Cosmology. *Phys. Rev. Lett.*, 112(3):031802, 2014.

[204] M. Antonello et al. A Proposal for a Three Detector Short-Baseline Neutrino Oscillation Program in the Fermilab Booster Neutrino Beam. 2015.

[205] Peter Ballett, Silvia Pascoli, and Mark Ross-Lonergan. MeV-scale sterile neutrino decays at the Fermilab Short-Baseline Neutrino program. *JHEP*, 04:102, 2017.

[206] Marco Battaglieri et al. US Cosmic Visions: New Ideas in Dark Matter 2017: Community Report. 2017.

[207] Eder Izaguirre and Itay Yavin. New window to millicharged particles at the LHC. *Phys. Rev.*, D92(3):035014, 2015.

[208] James D. Bjorken, Rouven Essig, Philip Schuster, and Natalia Toro. New Fixed-Target Experiments to Search for Dark Gauge Forces. *Phys. Rev.*, D80:075018, 2009.

[209] Brian Batell, Maxim Pospelov, and Adam Ritz. Exploring Portals to a Hidden Sector Through Fixed Targets. *Phys. Rev.*, D80:095024, 2009.

[210] Patrick deNiverville, Maxim Pospelov, and Adam Ritz. Observing a light dark matter beam with neutrino experiments. *Phys. Rev.*, D84:075020, 2011.

[211] Eder Izaguirre, Gordan Krnjaic, Philip Schuster, and Natalia Toro. New Electron Beam-Dump Experiments to Search for MeV to few-GeV Dark Matter. *Phys. Rev.*, D88:114015, 2013.

[212] Brian Batell, Rouven Essig, and Ze'ev Surujon. Strong Constraints on

Sub-GeV Dark Sectors from SLAC Beam Dump E137. *Phys. Rev. Lett.*, 113(17):171802, 2014.

[213] Bogdan A. Dobrescu and Claudia Frugiuele. GeV-Scale Dark Matter: Production at the Main Injector. *JHEP*, 02:019, 2015.

[214] Pilar Coloma, Bogdan A. Dobrescu, Claudia Frugiuele, and Roni Harnik. Dark matter beams at LBNF. *JHEP*, 04:047, 2016.

[215] Patrick deNiverville, Chien-Yi Chen, Maxim Pospelov, and Adam Ritz. Light dark matter in neutrino beams: production modelling and scattering signatures at MiniBooNE, T2K and SHiP. *Phys. Rev.*, D95(3):035006, 2017.

[216] Shao-Feng Ge and Ian M. Shoemaker. Constraining Photon Portal Dark Matter with Texono and Coherent Data. 2017.

[217] A. A. Prinz et al. Search for millicharged particles at SLAC. *Phys. Rev. Lett.*, 81:1175–1178, 1998.

[218] Sacha Davidson, Steen Hannestad, and Georg Raffelt. Updated bounds on millicharged particles. *JHEP*, 05:003, 2000.

[219] R. Acciarri and *et. al.* Long-Baseline Neutrino Facility (LBNF) and Deep Underground Neutrino Experiment (DUNE) Conceptual Design Report Volume 2: The Physics Program for DUNE at LBNF. 2, 2015.

[220] M. Anelli et al. A facility to Search for Hidden Particles (SHiP) at the CERN SPS. 2015.

[221] Hiroyuki Tashiro, Kenji Kadota, and Joseph Silk. Effects of dark matter-baryon scattering on redshifted 21 cm signals. *Phys. Rev.*, D90(8):083522, 2014.

[222] Rennan Barkana. Possible interaction between baryons and dark-matter particles revealed by the first stars. *Nature*, 555(7694):71–74, 2018.

[223] Julian B. Muñoz and Abraham Loeb. Insights on Dark Matter from Hydrogen during Cosmic Dawn. 2018.

[224] Judd D. Bowman, Alan E. E. Rogers, Raul A. Monsalve, Thomas J. Mozdzen, and Nivedita Mahesh. An absorption profile centred at 78 megahertz in the sky-averaged spectrum. *Nature*, 555(7694):67–70, 2018.

[225] Asher Berlin, Dan Hooper, Gordan Krnjaic, and Samuel D. McDermott. Severely Constraining Dark Matter Interpretations of the 21-cm Anomaly. 2018.

[226] Rennan Barkana, Nadav Joseph Outmezguine, Diego Redigolo, and Tomer Volansky. Signs of Dark Matter at 21-cm? 2018.

[227] Adam Falkowski and Kalliopi Petraki. 21cm absorption signal from charge sequestration. 2018.

[228] C. Amsler et al. *Physics Letters*, B667:1, 2008 and 2009 partial update for the 2010 edition.

[229] Given Eq. (6.4) and $\alpha = \Gamma(1+n, b+s_{\rm up})/\Gamma(1+n, b)$, any of our limits on ϵ can be rescaled for different choices of backgrounds. This is important for our projected sensitivities since detailed modelling of backgrounds will likely differ from what is assumed here.

[230] R. Dharmapalan et al. Low Mass WIMP Searches with a Neutrino Experiment: A Proposal for Further MiniBooNE Running. 2012.

[231] We anticipate the release of electron recoil data from MiniBooNE's dark matter run. Our modelling of backgrouds is motivated by their nucleon scattering data [112].

[232] R. Acciarri et al. Michel Electron Reconstruction Using Cosmic-Ray Data from the MicroBooNE LArTPC. *JINST*, 12(09):P09014, 2017.

[233] A. D. Martin, W. J. Stirling, R. S. Thorne, and G. Watt. Parton distributions for the LHC. *Eur. Phys. J.*, C63:189–285, 2009.

[234] R.L. Burman and E.S. Smith. Parameterization of pion production and reaction cross sections at lampf energies. 5 1989.

[235] R.L. Burman, M.E. Potter, and E.S. Smith. Monte carlo simulation of neutrino production by medium-energy protons in a beam stop. *Nuclear Instruments and Methods in Physics Research Section A: Accelerators, Spectrometers, Detectors and Associated Equipment*, 291(3):621 – 633, 1990.

[236] A. A. Aguilar-Arevalo et al. Neutrino flux prediction at miniboone. *Phys. Rev. D*, 79:072002, Apr 2009.

[237] M. Bonesini, A. Marchionni, F. Pietropaolo, and T. Tabarelli de Fatis. On Particle production for high-energy neutrino beams. *Eur. Phys. J.*, C20:13–27, 2001.

[238] Charles Gale, Sangyong Jeon, and Joseph I. Kapusta. J / psi production and absorption in high-energy proton nucleus collisions. *Phys. Lett.*, B459:455–460, 1999.

[239] A. Gribushin et al. Production of J/ψ mesons in p Be collisions at 530-GeV/c and 800-GeV/c. *Phys. Rev.*, D62:012001, 2000.

[240] I. Abt et al. Measurement of the υ production cross-section in 920-GeV fixed-target proton-nucleus collisions. *Phys. Lett.*, B638:13–21, 2006.

[241] B. Alessandro et al. J/psi and psi-prime production and their normal nuclear absorption in proton-nucleus collisions at 400-GeV. *Eur. Phys. J.*, C48:329, 2006.

[242] S. W. Herb et al. Observation of a Dimuon Resonance at 9.5-GeV in 400-GeV Proton-Nucleus Collisions. *Phys. Rev. Lett.*, 39:252–255, 1977.

[243] W. J. Stirling and M. R. Whalley. A Compilation of Drell-Yan cross-sections. *J. Phys.*, G19:D1–D102, 1993.

[244] D. M. Alde et al. Nuclear dependence of dimuon production at 800-GeV. FNAL-772 experiment. *Phys. Rev. Lett.*, 64:2479–2482, 1990.

[245] Alessandro Strumia and Francesco Vissani. Precise quasielastic neutrino/nucleon cross-section. *Phys. Lett.*, B564:42–54, 2003.

[246] Gaby Radel and Rolf Beyer. Neutrino electron scattering. *Modern Physics Letters A*, 08(12):1067–1088, 1993.

[247] Torsten Bringmann and Stefan Hofmann. Thermal Decoupling of Wimps from First Principles. *JCAP*, 0704:016, 2007. [Erratum: JCAP1603,no.03,E02(2016)].

[248] Tobias Binder, Laura Covi, Ayuki Kamada, Hitoshi Murayama, Tomo Takahashi, and Naoki Yoshida. Matter Power Spectrum in Hidden Neutrino Interacting Dark Matter Models: A Closer Look at the Collision Term. *JCAP*, 1611:043, 2016.

[249] N. Sartore, E. Ripamonti, A. Treves, and R. Turolla. Galactic neutron stars. I. Space and velocity distributions in the disk and in the halo. 510:A23, February 2010.